Direction Finding and Localization with Bluetooth 5.2

by

Xuchang Zhang

Student Name	Student Number
Xuchang Zhang	5458587

Daily Supervisor:	Dr. Arash Noroozi
Project Supervisor:	Dr. Raj Thilak Rajan
Project Duration:	November, 2022 - September, 2023
Faculty:	Faculty of Electrical Engineering, Delft

Abstract

The potential of indoor localization using the Bluetooth Low Energy approach has increased significantly with the incorporation of the Constant Tone Extension (CTE) function in BLE 5.1. These small and energy-efficient beacons transmit signals that Bluetooth-enabled devices may detect, allowing for proximity and positioning calculations. This technology supports uninterrupted navigation, customized location-dependent services, and novel applications such as indoor wayfinding, asset tracking, and proximity-based interactions. By integrating the new feature with an appropriate antenna array, it becomes possible to estimate both the Angle of Arrival (AoA) and Angle of Departure (AoD). This research exclusively focuses on the analysis of the AoA mode.

Nevertheless, estimating AoA poses significant challenges, particularly in indoor scenarios. In such a complex environment, the effect of multipath, which greatly corrupts the results, cannot be ignored. Furthermore, the low energy equipment used in BLE often results in high frequency offset, which cannot be ignored, especially when antenna array sampling does not occur at the same time. Throughout the span of this project, an in-depth analysis has been conducted on several elements in order to gain a comprehensive understanding of the positioning algorithm.

In this thesis, we first look into I/Q data processing. Then we looked into how the frequency offset is formed and how it affects estimation. To determine the frequency offset, we modeled the data structure and used the maximum likelihood approach. Following that, many AoA estimate approaches and multipath solving strategies are discussed. Since a 4×4 URA has been chosen for application, we discuss how they operate and the drawbacks of having a small number of antennas. A virtual antenna (VA) solution is offered to address the hardware limitation problem, although it fails in a multipath environment. Finally, we model the problem of AOA estimation, followed by a localization algorithm based on the estimated angles. The least squares (LS) and total least squares (TLS) approaches, as well as the Matlab algorithm, are introduced.

A Matlab simulation was performed to assess the algorithm's performance. The multipath scenario is constructed using the raytracing technique, wherein we imitate the situation within an empty room and only concentrate on the first-order reflection routes. We looked into a variety of aspects that could effect performance, such as the number of antennas, the number of data packets combined, the signal-to-noise ratio (SNR), the estimated number of sources, the parameters of multipath mitigation approaches, and so on. The simulation reveals that, with the correct settings, the Toeplitz Reconstruction (TR) method is the best. In the setting of a 4×4 uniform rectangular array (URA), it has been shown that over 90% of the results show a distance inaccuracy that is smaller than 0.14 meters. With an increased size of the 8×8 Uniform Rectangular Array (URA), a significant proportion of the outcomes, approximately 60%, exhibit a distance accuracy of less than 0.1 meters.

After the simulation, we conduct a real-world experiment in order to assess the practicality and effectiveness of the solutions. The decision to conduct the experiment in an open air area was made in order to minimize the potential interference caused by uncontrolled multipath. The TR approach demonstrates a distance inaccuracy of approximately 0.4 m, which is an improvement of approximately 0.1-0.2 m compared to conventional methods. The biggest challenge is in the estimation of elevation angles, which requires additional investigation. The results of azimuth angle estimate are comparable to prior 1-D AoA estimation studies. Even with a significant error rate in predicting elevation angle, the distance error is lower than in earlier positioning research.

Finally, we present possible directions for related future work. This could be optimizing algorithm parameters, considering other factors that might affect the antenna, modifying the given CTE configurations, and so on.

Acknowledgements

I would like to express appreciation to the individuals and organizations who provided assistance and guidance throughout the process of this thesis study.

I would want to express my gratitude to Kien Company for providing me with the opportunity to engage in this project and investigate on this innovative and promising technology.

Additionally, I would want to express my gratitude to my daily supervisor, Dr. Arash Noroozi. Arash consistently demonstrated support throughout the entirety of the project, and his professional demeanor effectively steered me through numerous challenging circumstances. I would also like to express my gratitude to another supervisor, Dr. Raj Thilak Rajan. The guidance provided by his structural approach greatly influenced the direction and formulation of the details within this study.

Lastly, I would want to express my gratitude for my friends and colleagues. The experience of working in Kien and studying at TU Delft is truly memorable and imbued with a sense of delight, owing to their invaluable contributions.

$XuchangZhang$
Delft, September 2023

Contents

1 Introduction

Locating an item is crucial in industrial usage, especially in modern age. An accurate localization result benefits the further processing of the item or the data. A typical positioning solution often contains the following factors [1]:

- Protocols for carrying the process;
- An infrastructure;
- Observations of one or more physic parameters, e.g. angles, distances, and time duration;
- A positioning method to calculate the location with the above observations;
- A reference system as the basis of computed locations.

For outdoor positioning, the Global Positioning Service (GPS) has already been sufficiently studied and improved in the areas of traffic navigation, surveying, and mapping since the start of its civil use in May 2000 [1]. On the other hand, for indoor positioning, a common universal solution has not been decided yet, as outdoor techniques cannot be directly applied to the indoor scenario. Conventional GPS receivers work poorly inside buildings, and cellular positioning methods suffer from huge errors. The application of an accurate indoor positioning solution is promising in all kinds of fields: asset tracking, patient monitoring, route optimization, workflow optimization, etc. As industries continue to embrace the potential of indoor positioning, the technology's transformative impact on efficiency, safety, and customer engagement becomes increasingly evident, opening doors to new levels of productivity and operational excellence.

Various localization and direction-finding methods have been studied using either absolute or relative measurements of different physical parameters, e.g., distance, time, angles, etc [2]. The Received Signal Strength Indicator (RSSI) measures the relative distance between the receiver and the transmitter. Time of Arrival (ToA) gives the absolute time instants of the transmission; Time Difference of Arrival (TDoA) uses the time difference instead of absolute values; The angle of Arrival (AoA) measures the angle of incoming signals with respect to the receiver, which contains multiple antennas.

Before Bluetooth 5.1, finding the direction of the signals with Bluetooth was often overlooked since only RSSI information could be exploited. Still, there was plenty of impressive research on this topic. [3] combined the fingerprinting technique with BLE, while others, like [4] chose the RSSI method. Both are not ideal. Fingerprinting requires environmental characterization, which involves a huge amount of training and exhausts the computation since the environment may change over time and thus change the characterization as well. RSSI index, on the other hand, is poor in a complex indoor environment where Bluetooth is often used considering its distance-limited communication.

As for direction-finding with Bluetooth, we focus on the AoA method because of a new feature named Constant Tone Extention (CTE). It was introduced by the Bluetooth Special Interest Group (SIG) after BLE 5.1 [5]. CTE provides a chance for the receiver antenna array to sample I/Q data containing phase information, which can be simply combined with the AoA method. This feature makes the application of Bluetooth in localization more promising than ever. Ye provides a detailed BLE-based AoA estimation algorithm with has Multiple Signal Classification (MUSIC) and PDDA on both ULA and Square Rectangular Antenna Arrays without discussing multipath effects [6]. Yao and the following

study from Cloudt both elaborate the BLE 1-D AoA estimation in the presence of other error estimations such as multipath effects and frequency deviation with ULA [7][8]. Shu introduced two-point positioning with two square antenna arrays but only activated a line of linear antennas on each board, which only enabled the positioning on a 2-D plane [9]. He implemented the Kalman filter in BLE-AoA estimation with ULA [10].

Currently, a practical BLE-AoA estimation algorithm is still underdeveloped. ULA is widely discussed but can only estimate angles or positions on a 2-D plane. URA is suitable for 3-D real-life positioning. But it is more complex in both modeling the data structure and mitigating multipath effects.

The scope of this thesis is to investigate accurate BLE-AoA estimations with a square antenna array and then position the transmitter with multiple locators, as shown in Fig.1.1. Error compensation techniques like multipath mitigation and frequency deviation estimation are discussed.

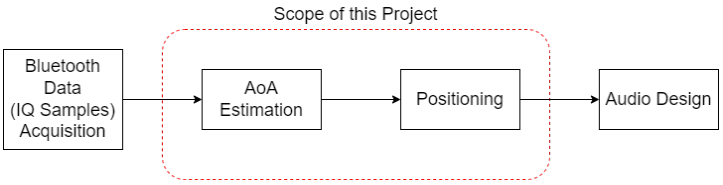

Figure 1.1: Scope of the Thesis.

1.1. Motivation

Direction Finding has long been a hot topic in fields like IoT, Automatic Mobile, and others [2]. As Bluetooth 5.1 introduces the AoA/AoD estimation feature and Bluetooth 5.2 introduces a data-compressing technique that enables higher audio quality transmission, this thesis mainly focuses on localization realization with the BLE feature.

This project is in cooperation with the company Kien. Kien is a company dedicated to innovative sound experiences based in Rotterdam. Through this project, we want to investigate the potential use of the new BLE feature to locate a user in a practical indoor environment so that our products could provide a customized audio experience based on position information. Such a method could also be promising for other industrial applications.

First, a few other direction-finding methods will be explained. And we will justify the choice of AoA in BLE devices.

1.1.1. Received Signal Strength Indicator (RSSI)

The Received Signal Strength Indicator, as the name implies, is a relative value that indicates the strength of the received signal. It could thus be used to calculate the distance between the transmitter and the receiver.

RSSI is simple and inexpensive because it only requires a path-loss model to estimate distance. In a Line-of-Sight (LOS) situation, for example, where the signal power only considers environmental features, a classic path-loss model is:

$$\text{RSSI} = -10n \log_{10} d + A \tag{1.1}$$

where n is the path loss coefficient ranging from 2 to 4 with different situations, A is the reference RSSI value of somewhere known, and d is the distance to be estimated [11]. To localize the exact position of interest, at least three receivers are required for trilateration.

However, the disadvantage of RSSI is also obvious. In Non-LOS (NLOS) situations or when complex multipath propagation is involved, there are extra signal attenuations introduced. In more complicated scenarios with obstacles and severe reflections indoors, the accuracy of the results could be poor.

1.1.2. Channel State Information (CSI)

The channel impulse response encompasses the amplitude and phase response of the channel across various frequencies and between distinct transmitter-receiver antenna pairs [12]. It can be written in

polar coordinate form:

$$H(f) = |H(f)|e^{j\angle H(f)} \tag{1.2}$$

with $|H(f)|$ represents the magnitude/amplitude response and $\angle H(f)$ the phase response of the frequency f

1.1.3. Fingerprinting

Fingerprinting is another classic and widely used DF method that takes environmental factors into account. This method is divided into two stages: an offline measurement collects RSSI or CSI data, and an online (or real-time) step obtains measurements and compares them to the offline ones to estimate. This is typically accomplished by mapping the user's location onto the offline point using online measurements. Other advanced methods, such as Artificial Neural Networks (ANN) and Support Vector Machines (SVM), have been proposed in addition to the basic method of maximum likelihood [13][14].

The main issue with mapping is that, due to the nature of mapping, the estimated position is discrete rather than continuous [2]. An offline grid with a higher density is required to improve the accuracy of the results. Offline measurements are collected in the form of RSSI values, as previously stated. Because the model is too vague, the signal-strength-based indicator may be unable to achieve the required level of accuracy. These Machine Learning methods, on the other hand, are more theoretical and too complex for applications that require fast, real-time results. Fingerprinting, on the other hand, is sensitive to minor changes in the target's position in space.

1.1.4. Time of Flight/Time of Arrival/Time Difference of Arrival

Both the Time of Flight (ToF) and Time of Arrival (ToA) approaches take into account the time signal propagation takes and then combine the observations with the previously known positions of the reference nodes [15].

Since the absolute time instants are involved, strict synchronizations between transmitters and receivers are demanded.

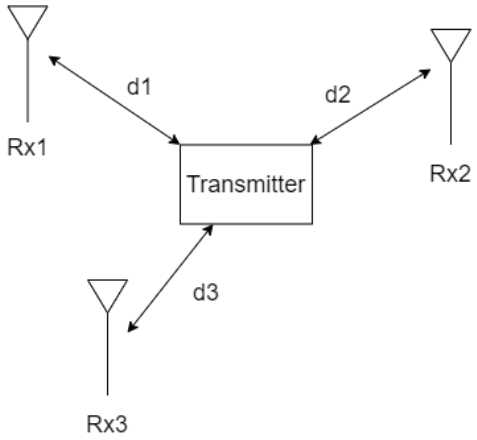

Figure 1.2: Illustration of Time of Arrival Method.

However, because ToF and ToA measure time instants for distance estimation, their accuracy necessitates precise synchronization between the transmitters and receivers. A high sample rate is also required for receivers to not miss arriving signals.

Time Difference of Arrival (TDoA) requires strict synchronization among the transmitters without involving the receiver. Multiple transmitters (at least three) are required to generate a set of hyperbolic equations. The geometry of TDoA is shown in Fig.1.3, where the red spot is the estimated spot of the target, i.e., the intersection of all three hyperbolas.

With all possible practical errors, the unique intersection spot cannot be guaranteed when there are more than three transmitters. So a set of equations between the unknown spot (x, y, z) and each known position of the i-th transmitter (x_i, y_i, z_i) and j-th transmitter (x_j, y_j, z_j):

$$L_{i,j} = \sqrt{(x_i - x)^2 + (y_i - y)^2 + (z_i - z)^2} - \sqrt{(x_j - x)^2 + (y_j - y)^2 + (z_j - z)^2} \tag{1.3}$$

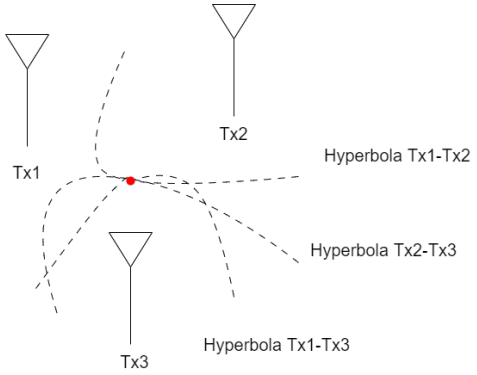

Figure 1.3: Illustration of Time Difference of Arrival Method.

These sets of equations can be solved with Linear Regression method [16]or linearized with Taylor-series expansion [2].

1.1.5. Angle of Arrival

Angle of Arrival (AoA) methods require antenna arrays set at different radiuses on the wave circles[17]. The angle is calculated with phase differences between antennas, as shown in Fig.1.4. Mainstream algorithms are subspace-based methods like MUSIC and ESPRIT. For Bluetooth 5.1, an AoA-estimation-related feature is added. Details for this technique will be explained in later sections. While AoA can offer precise estimation in scenarios when the distance between the transmitter and receiver is short, it necessitates more intricate hardware and meticulous calibration compared to RSSI techniques. Furthermore, the accuracy of AoA diminishes as the distance between the transmitter and receiver increases [2]. That is to say, a small error in the angle of arrival calculation results in a significant discrepancy in the estimation of the actual position [18].

The main error of AoA estimation comes from the multipath propagation. Apart from the LOS signals, especially for indoor scenarios, there are reflections from walls and obstacles between transmitters and receivers. These multipath signals are attenuated and delayed versions of the direct path. Such relationships between them may reduce the rank of the covariance matrix, so subspace methods would fail.

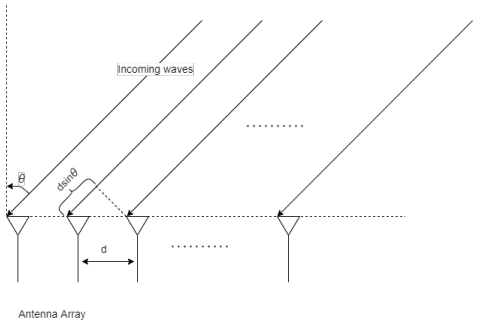

Figure 1.4: Illustration of Angle of Arrival Method.

1.2. Thesis Object

This thesis is to further investigate the direction-finding feature in Bluetooth and discuss its applicability to indoor positioning. Our objects are:

- Explore the direction-finding feature of Bluetooth;
- Investigate the 2-D AoA algorithm;
- Improve the AoA algorithm considering the multipath scenario;
- Develop a positioning algorithm after the angle estimation;

- Evaluate the performance of the algorithm with a MATLAB simulation;
- Conduct experiments to evaluate the performance of the algorithm using real-time transmitted data.

1.3. Report Structure

The structure of this report is listed as follows:

- Chapter 2 introduces the basis of the BLE technique and the direction-finding feature. Then the data model used throughout the project is formulated.
- Chapter 3 introduces how the frequency offset is generated and how to estimate it;
- Chapter 4 discusses different types of AoA estimation methods and their improvement under a multipath scenario;
- Chapter 5 shows how to estimate the position with multiple locators available;
- Chapter 6 presents and compares simulation results from different methods on different aspects;
- Chapter 7 shows the experiment setup of the project and the result.

With the introduction above, the flow chart for this project is shown in Fig.1.5.

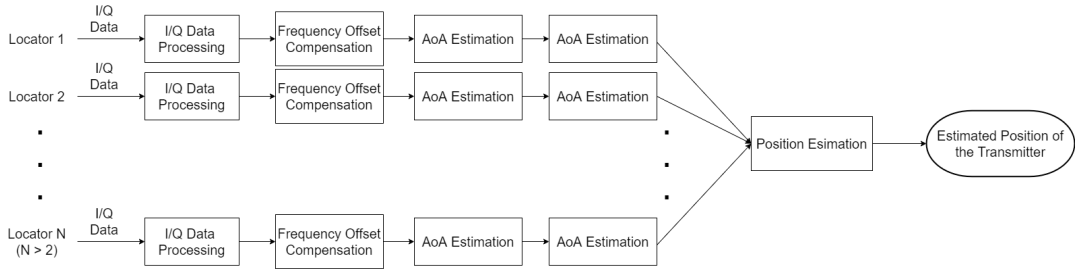

Figure 1.5: Flow Chart of the Project.

1.4. Nomenclature

1.4.1. Abbreviations

Abbreviation	Definition
DF	Direction Finding
BLE	Bluetooth Low Energy
CTE	Constant Tone Extension
FH	Frequency Hopping
ULA	Uniform Linear Array
URA	Uniform Rectangular Array
LOS	Line of Sight
NLOS	Non Line of Sight
ANN	Artificial Neural Network
SVM	Support Vector Machine
RSSI	Received Signal Strength Indicator
CSI	Channel State Information
ToA	Time of Arrival
TDoA	Time Difference of Arrival
AoA	Angle of Arrival
CFO	Carrier Frequency Offset
LS	Least Square
TLS	Total Least Square
MUSIC	MUltiple SIgnal Classification

Abbreviation	Definition
ESPRIT	Estimation of Signal Parameters via Rational Invariance Techniques
TR	Toeplitz Reconstruction
SS	Spatial Smoothing
FBSS	Forward-backward Spatial Smoothing
VA	Virtual Array
RMSE	Root Mean Square Error
MSE	Mean Square Error
LC3	Low Complexity Communication Cod
DK	development kit
SoC	System-on-Chip
PDU	Protocol Data Unit
CRC	Cyclic Redundancy Check
CDF	cumulative distribution function

1.4.2. Symbols

Symbol	Definition
M	number of antennas on the first direction
N	number of antennas on the second direction
M_T	total number of antennas
$\mathbf{S}$	the signal matrix received at the reference antenna
$\mathbf{A}$	the antenna steering matrix, or the array manifold matrix
$\mathbf{O}$	the frequency offset matrix
$\mathbf{\Gamma}$	the multipath profile matrix containing the phase shift and attenuation information
M_s	the number of antenna in one subarray on the primary direction
N_s	the nmuber of antenna in one subarray on the secondary direction
K	total number of sources (including multipath)
d	the spacing between two adjacent antennae
f_o	the frequency offset
f_c	the channel center frequency
λ	the wavelength of the Bluetooth signal sent by the transmitter
θ	the elevation angle
ϕ	the azimuth angle

1.5. Conclusion

Here in Chapter1, we introduce the fundamental concept of a positioning solution. Then, we explain the principle of multiple indoor locationing techniques including RSSI, ToA, AoA, and so on. Given their advantages and disadvantages, it is clear why we are more motivated to select AoA as the direction-finding technique within our project.

2

Basic Technique and Model

The basic BLE technique and mathematical model for this project are introduced in this chapter. First, we will go over the structure of CTE packets and how they can be used to estimate AoA. Then, because the sampled data are in the format of I/Q values, we will show how to process such a format for the following processing. Finally, a basic mathematical data model is built that takes into account the antenna response, multipath effects, and frequency offset.

2.1. Bluetooth Low Energy

BLE is a wireless communication technology based on Bluetooth but consumes less power than Bluetooth Basic [5]. It covers frequencies ranging from 2.402 GHz to 2.480 GHz. The frequency band is divided into 40 channels including 37 data channels and 3 advertising channels, with each center frequency separate 2 MHz from the others. The distribution of all the channels is illustrated in Fig.2.1 [19].

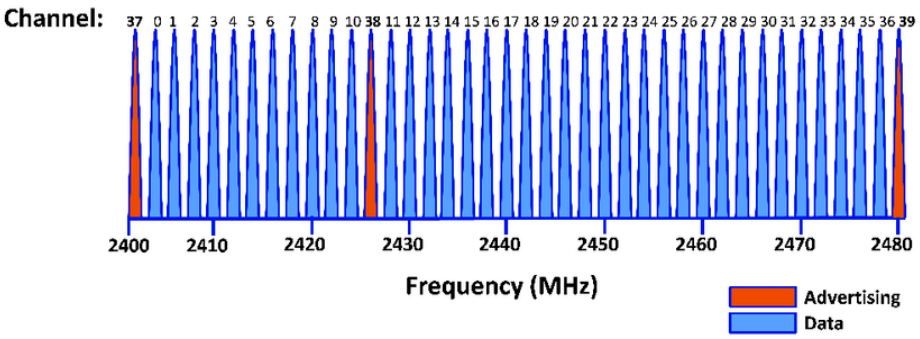

Figure 2.1: The BLE Channel Distribution.

Before CTE was introduced, BLE-based localization techniques can be broadly categorized into either fingerprinting [20] or RSSI-based ranging [21][22][23]. The downside of fingerprinting, as previously explain in Chapter1, is that it requires a significant amount of training effort to characterize an environment and often such a characterization is temporary as the environment changes over time [24]. In contrast, RSSI-based range encounters challenges in achieving high accuracy due to the lack of effective techniques to mitigate the impact of multipath effects in BLE communication.

Thus, when it comes to the positioning accuracy, these BLE-based methods shows rather large error in positioning result. One example is the Bluepass system [25]. Bluepass is a Bluetooth-based indoor MBL system that uses RSSI readings from user devices to calculate the distance between them and stationary Bluetooth receivers. It comprises a central server, local server, Bluetooth detecting device, and user device app. To use it, users must install the app and login on their smartphone. A mean square error (MSE) of 2.33m is achieved. Other examples including Ayyalasomayajula et al. offered a CSI-based localization systems using BLE technology where a 86cm accuracy is attained [26]; Islam et

al. proposed a unique multipath profiling approach for tracking any BLE tag in an indoor context which has a range error of around 2.4 m [24].

2.1.1. Bluetooth 5.2

The direction-finding feature was introduced with Bluetooth 5.1, and Bluetooth 5.2 builds upon this by incorporating the new LC3 codec. This codec ensures the potential for higher audio quality through more efficient information compression [27]. Given that this project focuses on an algorithm tailored for audio applications, Bluetooth 5.2 has been chosen as the preferred version. The primary features of the three most recent BLE versions are summarized in Table 2.1.

Table 2.1: The Three Most Recent Versions of BLE

Versions	Main Features
5.0	Double faster data transfer than previous version; Transmitted range expanded;
5.1	Introducing direction finding with CTE structure; Improvements in caching and paring processes;
5.2	Introducing the new LC3 codec; Introducing an Enhanced Attribute protocol; Using Isochronous Channel;

To conclude, Bluetooth 5.1 introduced the direction-finding feature, while Bluetooth 5.2 introduced an Low Complexity Communication Codec (LC3 codec) that enables the engineer to utilize it in audio applications without losing quality. Considering the requirements of the company,

2.1.2. Direction Finding with CTE

The structure of data packages sent by BLE transmitters is illustrated in Fig.2.2. The direction-finding information is contained in the last part of the package, i.e. the Constant Tone Extension(CTE). Each advertisement will always start with one of the three primary channels. Then, since the package is too long to send in one channel, the appended CTE will be sent randomly in one of the secondary channels. The random frequency jumping is called Frequency Hopping (FH) which is introduced to prevent interference with Wi-Fi signals. This way of advertisement is called Periodic Advertisements, which is another feature of Bluetooth 5's Extended Advertisement [27].

Such an advertisement enables communication between transmitters and receivers in an unconnected mode. The connection-less mode is more feasible for the product's practical application because one tag can broadcast the package to several receivers and be located using the triangulation method.

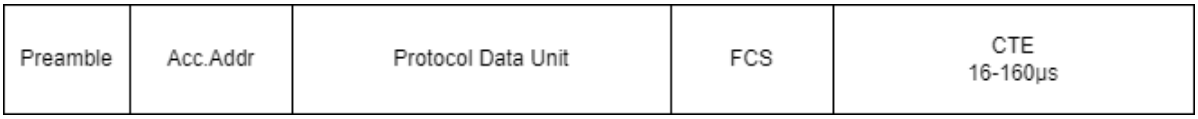

Figure 2.2: The BLE Package Structure.

The detailed composition of CTE is shown in Fig.2.3. The guard period separates the information in the previous sections of the packet from what is contained in CTE. This section contains no meaningful samples. The first IQ sample available is in the reference period which lasts for 8 μs with 8 samples contained in total. The remainder of the CTE is comprised of sample slots and switch slots. For each switch, a different antenna is sampled. The length of these slots can be either 1 μs or 2 μs. But once the value is set, all switch and sample slots should be of the same length.

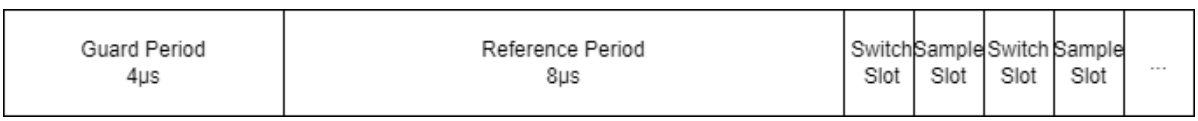

Figure 2.3: Constant Tone Extension Structure.

2.1.3. IQ Sampling

The samples in Fig.2.3 are stored in the format of IQ samples. IQ samples represent a signal with in-phase (I) and quadrature (Q) components, and the phase is easy to estimate with these two components known. The phase may obviously be computed using the arctan function. However, since the arctan

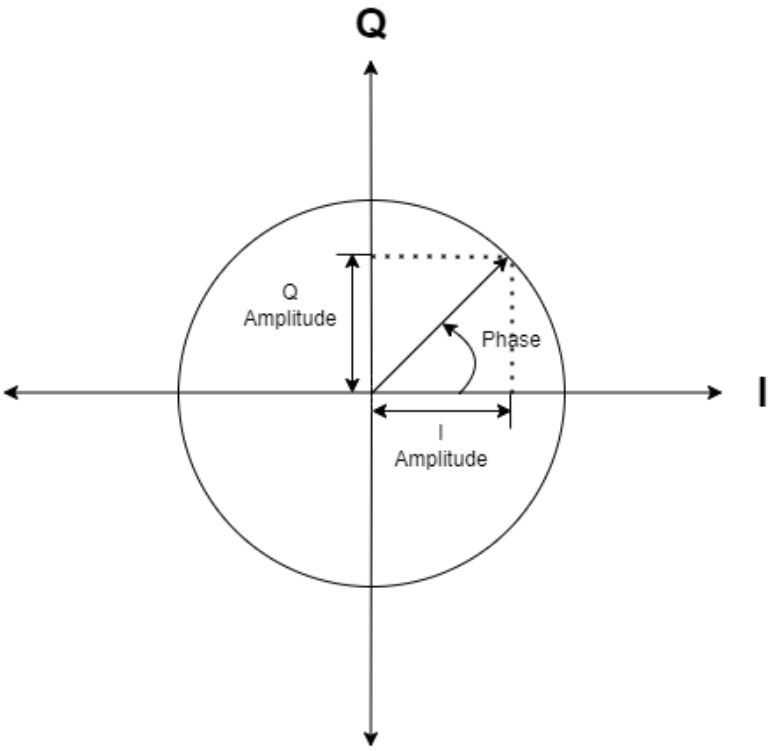

Figure 2.4: Illustration of IQ Sampling.

function in Matlab can only map the result into the range of $[-\pi/2, \pi/2]$, we have to further process these data as in (2.1) to adjust the range of mapping to $[0, 2\pi]$

$$\Phi = \begin{cases} arctan(\frac{Q}{I}) & if I > 0 Q \geq 0 \\ arctan(\frac{Q}{I}) + 2\pi & if I > 0 Q < 0 \\ arctan(\frac{Q}{I}) + \pi & if I < 0 Q \neq 0 \\ \frac{\pi}{2} & if I == 0 Q > 0 \\ \frac{3\pi}{2} & if I == 0 Q < 0 \end{cases} \tag{2.1}$$

2.1.4. Antenna Switch Patterns

During the sample-switch time, the sampling ordering, known as the Antenna Switch Pattern, can be determined. In the case of a ULA with M antennas, two primary patterns are introduced here: Round-Robin ([1,2,...M,1,2...]) and Return-to-First ([1,2,1,3,...1,M,...]). Other patterns include Mirror ([1,2,...,M,M-1,...2,1]). The distinction between Round Robin and Return to First is depicted in Fig.2.5.

2.2. Basic Data Model

The M $\times$ N antenna arrays used in this project are Nordic boards with 12 antennas, i.e. M $= 4$, N $= 4$, but with four inner locations unfilled. The numbers M and N represent the number of antennas in the primary and secondary directions, respectively. The primary direction in data model construction here is x, and the secondary direction is y.

Fig.2.6 shows the antenna placements and their accompanying numbers. d is the distance between two neighboring antennas that is equal on both axes. The positive direction of x-axis is defined as Ant2-Ant1-Ant12-Ant11, while the positive direction of y-axis is defined as Ant2-Ant3-Ant4-Ant5. The

Sample Period Ant1	Switch Period	Sample Period Ant2	Switch Period	Sample Period Ant1	Switch Period	...	Sample Period Ant1	Switch Period	Sample Period AntM	Switch Period	...

(a) Return-to-First Pattern

Sample Period Ant1	Switch Period	Sample Period Ant2	Switch Period	Sample Period Ant3	Switch Period	...	Sample Period AntM	Switch Period	Sample Period Ant1	Switch Period	...

(b) Round-Robin Pattern

Figure 2.5: Illustration of Two Antenna Switch Patterns

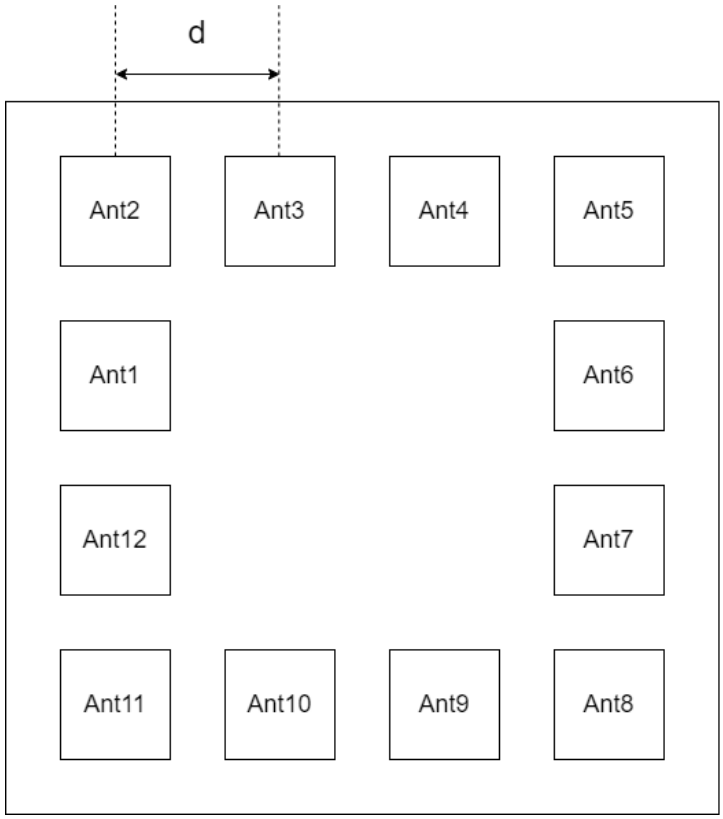

Figure 2.6: Illustration of Antenna Array with 12 Antennas.

positions of the antenna can then be expressed with d. The (m,n)-th antenna with 2-D coordinate (d_m, d_n) with $d_m, d_n \subseteq \{0, 1, 2, 3\}$ is at the position:

$$\begin{cases} d_m = (m-1)d \\ d_n = (n-1)d \end{cases} \tag{2.2}$$

It is important to observe that due to the configuration of the antenna array on the board, which is a partial 4×4 URA array rather than a complete array, the values of $(\mathsf{d_m}, \mathsf{d_n})$ are restricted and cannot encompass all possible combinations from (0,0) to (3,3). For instance, the coordinate (1,1) is non-existent. The relationship between the orders of antennas depicted in Figure 2.6, their corresponding positions, and their respective two-dimensional coordinates may be found in Table 2.2.

Antenna 2 is positioned at the top of the list due to its placement as the first antenna during the switch-sample period, serving as the reference antenna.

The current configuration of the antenna array allows for estimation of angles in a three-dimensional environment, specifically the azimuth angle ϕ and the elevation angle θ. The two angles are defined in Fig.2.7. The position of the point source is denoted by the red spot labeled as S. In this context, the coordinate system is defined with respect to the reference antenna's location within the entire array. The symbol S represents the position of the transmitter that is to be estimated.

First, consider there is only one point signal source without any multipath. The signal received at Ant2 at time instant t is represented as $s_0(t)$. In order for the time delay across antennas to be conveyed

Table 2.2: The Correspondence of Antenna Order, 2-D Coordinates, and Position.

Antenna Order	2-D Coordinate	Position	Antenna Order	2-D Coordinate	Position
2	(0,0)	(0,0)	8	(3,3)	(3d,3d)
3	(0,1)	(0,d)	9	(3,2)	(3d,2d)
4	(0,2)	(0,2d)	10	(3,1)	(3d,d)
5	(0,3)	(0,3d)	11	(3,0)	(3d,0)
6	(1,3)	(d,3d)	12	(2,0)	(2d,0)
7	(2,3)	(2d,3d)	1	(1,0)	(d,0)

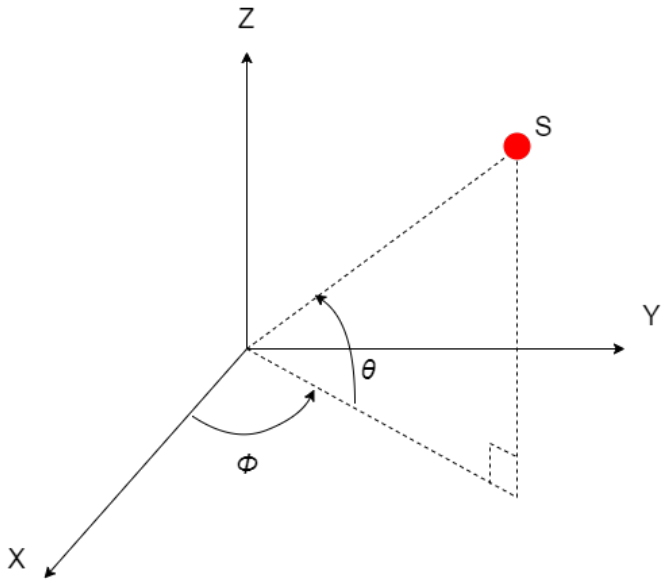

Figure 2.7: Definition of the Azimuth Angle (ϕ) and the Elevation Angle (θ).

as a phase shift, it is necessary for the point source denoted as s_0 to adhere to the narrowband and farfield assumption. In order to make this assumption, it is required that the amplitude $a(t)$ and phase $b(t)$ of the signal $s_0(t) = a(t)e^{j(2\pi f_c t + b(t)}$ change at a slower rate compared to the propagation time delay τ. , i.e.

$$a(t-\tau) \approx a(t) \quad b(t-\tau) \approx b(t) \tag{2.3}$$

Under such a condition, the delayed signal can be modeled as a phase-shifted version as

$$s(t-\tau) = a(t-\tau)e^{j2\pi f_c(t-\tau)+b(t-\tau)} \approx a(t)e^{j2\pi f_c(t-\tau)+b(t)} = e^{-j2\pi f_c \tau} s_0(t) \tag{2.4}$$

The relationship between the time delay τ and the distance between two receivers, in relation to the speed of wave propagation indicated as c, can be expressed. In the instance of the ULA (Uniform Linear Array), wherein the distance between adjacent elements is denoted as d and the angle at which the signal impinges is represented as θ, the resulting delay can be observed.

$$\tau = \frac{d\cos\theta}{c} \tag{2.5}$$

Take Ant2 in Fig.2.6 as the reference antenna, the signal received at another antenna m with coordinates (d_x, d_y) is a phase-shifted version of $s_0(t)$, which is

$$s_m(t) = e^{-j\frac{2\pi(d_x \cos\phi + d_y \sin\phi)\cos\theta}{\lambda}} s_0(t) \tag{2.6}$$

Assume the noise $\mathbf{n}(t)$ is temporal and spatial Gaussian white noise which is uncorrelated to the signals. The noise vector contains all factors related to noise in the practical data but could not simply

be modeled with (2.6) [28]. Then the M×1 data vector received at instant t, $\mathbf{x}(t)$, equals

$$\begin{aligned}\mathbf{x}(t) &= \begin{bmatrix} 1 \\ e^{-j\frac{2\pi d \cos\phi\cos\theta}{\lambda}} \\ e^{-j\frac{2\pi 2d \cos\phi\cos\theta}{\lambda}} \\ \vdots \\ e^{-j\frac{2\pi(M-1)d \cos\phi\cos\theta}{\lambda}} \\ e^{-j\frac{2\pi d \sin\phi\cos\theta}{\lambda}} \\ e^{-j\frac{2\pi d(\cos\phi\cos\theta+\sin\phi\cos\theta)}{\lambda}} \\ \vdots \\ e^{-j\frac{2\pi d((M-1)\cos\phi\cos\theta+(N-1)\sin\phi\cos\theta)}{\lambda}} \end{bmatrix} s_0(t) + \mathbf{n}(t) \\ &= \mathbf{a}(\theta,\phi)s_0(t) + \mathbf{n}(t) \end{aligned} \tag{2.7}$$

where $\mathbf{a}(\theta,\phi) \in \mathbb{C}^{MN\times 1}$ is the steering vector for the LOS signal.

Dive into the structure of $\mathbf{a}(\theta,\phi)$ by looking at its two directions, we find that

$$\begin{aligned}\mathbf{a}(\theta,\phi) &= \boldsymbol{\gamma} \otimes \boldsymbol{\beta} \\ &= \begin{bmatrix}1 & \gamma & \cdots & \gamma^{(N-1)}\end{bmatrix}^T \otimes \begin{bmatrix}1 & \beta & \cdots & \beta^{(M-1)}\end{bmatrix}^T \end{aligned} \tag{2.8}$$

where $\boldsymbol{\beta}$ and $\boldsymbol{\gamma}$ are the steering unit of primal and secondary direction respectively, and $\otimes$ denotes the Kronecker product.The explicit definition of $\boldsymbol{\gamma}$ and $\boldsymbol{\beta}$ themselves depends on the direction they referring to, as shown in Tab.2.3. As in the data model of this project, the primal direction is x-axis and secondary direction is y-axis. So in (2.8), $\beta = e^{-j\frac{2\pi d \cos\phi\cos\theta}{\lambda}}$ and $\gamma = e^{-j\frac{2\pi d \sin\phi\cos\theta}{\lambda}}$. In the context of the simulated scenarios described in the Matlab BLE functions, it is observed that the primary direction is aligned with the z-axis, while the secondary direction is aligned with the y-axis. Consequently, the formulation of the steering vectors associated with these situations should be adjusted accordingly.

Table 2.3: Steering Unit for Each Direction

Direction	Steering Unit
X	$e^{-j\frac{2\pi d \cos\phi\cos\theta}{\lambda}}$
Y	$e^{-j\frac{2\pi d \sin\phi\cos\theta}{\lambda}}$
Z	$e^{-j\frac{2\pi d \sin\theta}{\lambda}}$

When there is only one direct path signal, as shown in (2.7),

$$\mathbf{x}(t) = \mathbf{a}(\theta,\phi)s_0(t) + \mathbf{n}(t)$$

the signal captured by each antenna is an altered version of the signal received at the reference antenna, only with a phase shift. The phase difference provides all the pertinent information related to the two angles. In an ideal scenario, the angle information can be accurately retrieved once the phase difference is observed, utilizing direction-finding techniques such as MUSIC.

2.2.1. Multipath Propagation

Nevertheless, when it comes to indoor localization, it is important to take into account the influence of multipath phenomena, such as reflections, scattering, and diffraction. The circumstances under which these three forms of propagation occur are provided in Tab.2.4, where the symbol λ represents the wavelength of the signal.

This project exclusively focuses on the reflection type of multipath. The analysis is limited to the scenario where both the transmitter and receivers are positioned at the center of the room or along the walls, in order to exclude more complex signal propagation scenarios such as the corners of the walls. Both the simulation and the experiment assume a scenario where the room is empty and there are no minor objects obstructing the propagation.

Fig.2.8 illustrates how the reflection multipath signals are generated. It is evident that when there is

Table 2.4: Types of Multipath Propagation

Type of Multipath Propagation	Condition	Example
Reflection	Size of object is much larger than λ	Solid surface of walls
Diffraction	Size of object is larger than λ	Edges or Corners of walls
Scattering	Size of object is smaller than λ	Small objects in the room

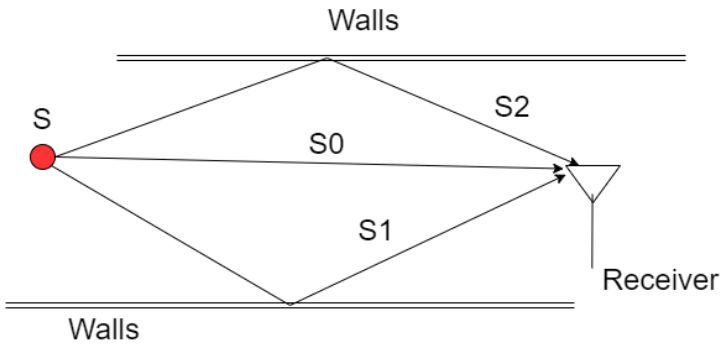

Figure 2.8: Illustration of Multipath Effects.

only one source, the signals received at the antenna experience a reduction in amplitude and a delay in phase, relative to the signal transmitted directly.

It is assumed that the number of multipath signals is K-1, and there are a total of K signals arriving at each antenna. When multipath signals hit the antenna, they undergo attenuation and delay, resulting in the generation of a multipath signals vector

$$\mathbf{s}(t) = \begin{bmatrix} 1 \\ \alpha_1 e^{-\tau_1} \\ \vdots \\ \alpha_{K-1} e^{-\tau_{K-1}} \end{bmatrix} s_0(t) \tag{2.9}$$

the symbol α_k represents the amplitude attenuation factor for the k-th multipath, whereas τ_k represents the time delay associated with the k-th multipath. The outcome $\mathbf{s}(t)$ is a vector of dimensions K$\times$1.

The data received at time instant t is then extended to

$$\mathbf{x}(t) = \mathbf{A}\mathbf{s}(t) + \vec{n}(t) \tag{2.10}$$

$$= \mathbf{A} \begin{bmatrix} 1 \\ \alpha_1 e^{-\tau_1} \\ \vdots \\ \alpha_{K-1} e^{-\tau_{K-1}} \end{bmatrix} s_0(t) + \mathbf{n}(t) \tag{2.11}$$

A is the complex-valued antenna manifold matrix that describes the antenna response per antenna and per multipath, which is

$$\mathbf{A} = \begin{bmatrix} \mathbf{a}_1(\boldsymbol{\theta}, \boldsymbol{\phi}) \\ \mathbf{a}_2(\boldsymbol{\theta}, \boldsymbol{\phi}) \\ \vdots \\ \mathbf{a}_{M_T}(\boldsymbol{\theta}, \boldsymbol{\phi}) \end{bmatrix} \tag{2.12}$$

$$= \begin{bmatrix} a_1(\theta_1, \phi_1) & a_1(\theta_2, \phi_2) & \dots & a_1(\theta_k, \phi_k) \\ a_2(\theta_1, \phi_1) & a_2(\theta_2, \phi_2) & \dots & a_2(\theta_k, \phi_k) \\ & \vdots & & \\ a_{M_T}(\theta_1, \phi_1) & a_{M_T}(\theta_2, \phi_2) & \dots & a_{M_T}(\theta_k, \phi_k) \end{bmatrix} \tag{2.13}$$

$$\tag{2.14}$$

where $\mathbf{a}_m(\boldsymbol{\theta}, \boldsymbol{\phi})$ indicates the steering row vector for them-th antenna, $\boldsymbol{\theta}$ and $\boldsymbol{\phi}$ are the vectors of elevation angles and azimuth angles for all multipath, and M_T is the number of antennas in total. For a full URA $M_T = MN$. Since the far-field assumption is made, each multipath signal arrives at different antennas with the same incident angle. The explicit structure of each element of the steering row vector is alike to (2.7). The steering element for (m,n)-th antenna with the coordinate (d_{xm}, d_{ym}) and k-th multipath is

$$a_m(\theta_k, \phi_k) = e^{-j\frac{2\pi(d_{xm}\cos\phi_k + d_{ym}\sin\phi_k)\cos\theta_k}{\lambda}} \tag{2.15}$$

In the case of collecting N samples, the point source signal ceases to be represented as a single numerical value and instead becomes a row vector $\mathbf{s}_0$

$$\mathbf{s}_0 = \begin{bmatrix} s_0(t_1) & s_0(t_2) & \dots & s_0(t_N) \end{bmatrix} \tag{2.16}$$

$$= \begin{bmatrix} s_0(t_1) & s_0(t_1 + \triangle T) & \dots & s_0(t_N + (N-1)\triangle T \end{bmatrix} \tag{2.17}$$

Let t_n represent the n-th sample instant. Given that the sample interval is determined by the length of the sample slot, we may express t_n as $t_n = t_1 + \triangle T$, where $\triangle T$ denotes the sample interval. The requirement for the antenna switch slots and sample slots in CTE to have equal lengths implies that the difference in length, denoted as $\triangle T$, is always twice the length of the slot. When the duration of the sample slot is 2μs, the corresponding change in time, denoted as $\triangle T$, is 4μs. Similarly, when the duration of the sample slot is reduced to 1μs, the corresponding change in time, denoted as $\triangle T$, is 2μs.

With multipath, the signal sent is now a $K \times N$ matrix that is

$$\mathbf{s} = \begin{bmatrix} 1 \\ \alpha_1 e^{-\tau_1} \\ \vdots \\ \alpha_{K-1} e^{-\tau_{K-1}} \end{bmatrix} \mathbf{s}_0 \tag{2.18}$$

$$= \boldsymbol{\Gamma} \begin{bmatrix} s_0(t_1) & s_0(t_2) & \cdots & s_0(t_N) \end{bmatrix} \tag{2.19}$$

where $\boldsymbol{\Gamma}$ stands for the vector containing the multipath attenuation and phase shifting information.

To conclude, the data model of M antennas and N samples each is

$$\mathbf{X} = \mathbf{A}\mathbf{s} + \mathbf{N} \tag{2.20}$$

$$= \mathbf{A}\boldsymbol{\Gamma}\mathbf{s_0} + \mathbf{N} \tag{2.21}$$

where $\mathbf{N}$ is the Gaussian white noise matrix with size $M \times N$.

2.2.2. Antenna Switch Effects

In section2.2, the data model with simultaneous sampling and multipath is discussed.

However, the IQ sampling in the CTE period is not a simultaneous process. The sampling instants of the non-reference antennas are related to the antenna switch pattern introduced in the previous section. In this project, we take the Round-Robin switch pattern.

As shown in Fig.2.3, in the switch-sample period, only one antenna is sampled at one sample instant. So the data can be interpreted as

$$\mathbf{X} = \begin{bmatrix} X_1(t_1) & X_1(t_{1+M_T}) & \cdots & X_1(t_N) \\ X_2(t_2) & \ddots & & \vdots \\ \vdots & & \ddots & \\ X_{M_T}(t_{M_T}) & \cdots & & X_{N+(M_T-1)} \end{bmatrix} \tag{2.22}$$

$$= \begin{bmatrix} X_1(t_1) & X_1(t_{1+M_T\triangle T}) & \cdots & X_1(t_N) \\ X_2(t_{1+\triangle T}) & \ddots & & \vdots \\ \vdots & & \ddots & \\ X_{M_T}(t_{1+(M_T-1)\triangle T}) & \cdots & & X_{N+(M_T-1)\triangle T} \end{bmatrix} \tag{2.23}$$

$$= \mathbf{OA}\boldsymbol{\Gamma} \begin{bmatrix} \mathbf{s}(t_1) & \mathbf{s}(t_2) & \cdots & \mathbf{s}(t_N) \end{bmatrix} \tag{2.24}$$

where t_n indicates the n-th sampling instant and $X_m(t_n)$ is the signal received at antenna m in instant t_n. If it the Round-Robin pattern is chosen, then in each column (or, each cycle), the m-th antenna is sampled at instant $t_m = t_1 + (m-1) \triangle T$. **O** is the offset matrix due to sampling at different time instants, which is constructed as:

$$\mathbf{O} = \begin{bmatrix} 1 & 0 & \cdots & 0 \\ 0 & e^{-j2\pi f \triangle T} & \cdots & \vdots \\ \vdots & \vdots & \ddots & \vdots \\ 0 & \cdots & & e^{-j2\pi(M_T-1)f\triangle T} \end{bmatrix} \tag{2.25}$$

$\triangle T$ is the time interval between two seccesive sample slots.

The present approach for estimating the DoA prioritizes data from the same time instant in each column. It is imperative to recreate the data matrix by utilizing the inverse of the offset matrix.

Due to the forthcoming discussion on frequency deviation in subsequent chapters, it is important to note that the observed channel frequency, denoted as f_{real}, does not align with the carrier frequency, denoted as f_c. The calculation of the offset matrix in equation (2.25) is not feasible for the data construction and hence requires an initial estimation. In subsequent chapters, we will present the methodology for estimating and constructing the offset matrix.

2.2.3. Conclusion

In this section, we present the fundamental data model for BLE 2-D AoA estimation. The model incorporates the **O** matrix, which accounts for the antenna switch effect that is particularly significant in the context of BLE problems. Additionally, the model includes the antenna steering matrix **A** that includes all angle information, and the $\mathbf{\Gamma}$ vector, which is introduced due to multipath propagation and cannot be disregarded in indoor scenarios. Subsequent chapters will dive further into the examination of solutions aimed at mitigating the impact of CFO and multipath, with the ultimate goal of enhancing the precision of angle estimation and following localization processes.

3

Frequency Deviation and Offset Estimation

In the previous chapters, the offset matrix in (2.25) is constructed as:

$$\mathbf{O} = \begin{bmatrix} 1 & 0 & \cdots & 0 \\ 0 & e^{-j2\pi f \triangle T} & \cdots & \vdots \\ \vdots & \vdots & \ddots & \vdots \\ 0 & \cdots & & e^{-j2\pi(M_T-1)f\triangle T} \end{bmatrix}$$

was discussed for the purpose of reconstructing a data matrix with synchronous samples in the corresponding column. Consequently, an accurate estimation of the true frequency becomes essential. This chapter dives into the generation of frequency deviation and the methods for estimating this offset.

3.1. Frequency Offset Compositon

According to the Bluetooth core specification [27], the 2GFSK modulation used in BLE has a frequency deviation f_{dev}. The minimum frequency deviation shall never be less than 185 kHz data rate is 1 mega symbol per second (Msym/s) symbol rate and never be less than 370 kHz with a data rate of 2 Msym/s. The modulation can be denoted as [29]:

$$s_{2GFSK}(t) = \begin{cases} A\cos\left[2\pi f_c t + 2\pi I_m \int_{-\infty}^{t} m(\tau)d\tau + \beta_1\right], & 1 \text{ is sent} \\ A\cos\left[2\pi f_c t - 2\pi I_m \int_{-\infty}^{t} m(\tau)d\tau + \beta_2\right], & 0 \text{ is sent} \end{cases} \tag{3.1}$$

where $s_{2GFSK}(t)$ is the modulated signal, while the channel frequency is represented by f_c, which is dependent upon the specific channel employed for the current CTE package. Additionally, the starting phase of the signal is denoted as β_1 and β_2. The variable $m(\tau)$ represents the message signal subsequent to undergoing the Gaussian filter. Given that CTE symbols are consistently represented by the value of 1, it may be inferred that the deviation will invariably yield a positive result.

In this project, the frequency deviation is assumed to be constant across one packet. The relation between this deviation, modulation index I_m, and the data rate is defined as [30]:

$$f_{\text{dev}} = \frac{f_{\text{data}}}{2} I_m \tag{3.2}$$

The variable f_{data} represents the data rate, which can take on values of either 1 Mb/s or 2 Mb/s. Meanwhile, I_m denotes the modulation index. The determination of such an index is dependent upon the hardware, typically falling within the range of 0.45 to 0.55. It can be deemed stable alone when the value of I_m lies between 0.495 and 0.505. Given a data rate of $f_{\text{data}} = 2$ Mb/s and a modulation index of I_m =0.5, the resulting frequency deviation is precisely 500 kHz. According to the Bluetooth Special

Interest Group (Bluetooth SIG), the minimum frequency deviation should be equal to or greater than 185kHz when transmitting at a rate of 1 Mb/s, and equal to or greater than 370kHz when transmitting at a rate of 2Mb/s [27]. The variability of f_{dev} is attributed to the premodulation process, which is influenced by various features of the Gaussian filter and the symbol rates determined by individual users.

The fluctuation of I_m primarily arises from the precision of the local oscillators used in BLE receivers, often measured in parts per million (ppm). BLE is a cost-effective form of communication that utilizes oscillators characterized by high ppm. Despite the modest scale of absolute value of ppm, it is important to acknowledge that signal distortion cannot be disregarded while utilizing at wireless communication with high frequencies, such as the 2.4 GHz operation frequency for Bluetooth. For instance, a crystal working within a 2.4 GHz BLE system with a frequency stability of $\pm$30 ppm has the potential to produce a maximum frequency deviation of.

$$\pm\frac{30}{10^6} \times 2.4 \times 10^9 = \pm 72\text{kHz} \tag{3.3}$$

In the event that the oscillators of the receiver and transmitter exhibit opposing signs, such as a positive deviation of +20 ppm for the receiver and a negative deviation of -20 ppm for the transmitter, the resulting total deviation may be significantly amplified. The oscillator may also be influenced by physical ambient factors, like temperature, humidity, and pressure. The precise estimation of frequency deviation is necessary due to its inherent variability among different chips. Additional errors, such as frequency drift, have the potential to be added into the model. However, given their comparatively smaller magnitudes in relation to f_{dev}, the model does not explicitly account for additional frequency mistakes.

In conclusion, the frequency offset between the transmitter and the receiver include faults that result from crystal oscillation and the characteristics of 2GFSK modulation. Together we use f_{o} to denote the whole difference of the real frequency from the given channel frequency. Then the received signals is:

$$s(t) = A\cos\left[2\pi f_c t + 2\pi f_o t + \beta_1\right] \tag{3.4}$$

Regardless of which channel is exactly in use, since the channel central frequency is large enough and the sample periods are either $2 \times 10^{-6}\ f_c t$or $4 \times 10^{-6}\ f_c t$ is always an integer and at the end shows no difference in the phase. Only the small value would play a crucial role in the offset matrix to shift the phase of the sampled IQ data.

This research project aims to estimate and compensate for the combined frequency offset of all the terms added to the channel frequency f_c, relative to f_c. The reason for estimating and compensating for this combined offset is that they accumulate over time together. All errors are regarded as constant inside a single CTE packet. The tolerance of various frequency mistakes as described by the Bluetooth Core Specification [5] is presented in Table 3.1.

Table 3.1: Frequency Error Tolerance

Frequency Error Name	Tolerance
Frequency Deviation	LE 1M PHY: $f_{dev} \geq$ 185kHz; LE 2M PHY: $f_{dev} \geq$ 370kHz;
Frequency Drift	$-50kHz \leq f_d \leq +50kHz$ within one package

3.2. Frequency Offset Estimation

The estimation of the frequency offset can be determined through the investigation of IQ samples within the reference period. As shown in Fig.2.3, the samples obtained within the initial 8 µs originate from the same antenna. Given that the CTE symbols are unmodulated and unwhitened 1, it can be observed that the frequency deviation remains constant and positive. In the absence of frequency variation, assuming reference sample intervals of 1 µs, the expected phase difference can be calculated as follows:

$$\begin{aligned} \triangle\Phi &= 2\pi \times f_c \times T \\ &= 2\pi \times 2402MHz \times 1 \times 10^{-6}s \end{aligned} \tag{3.5}$$

The frequency of channel 37, 2402 MHz, is selected. However, it is important to note that the choice of channels does not impact the outcome, as all channel frequencies are measured in the same units of MHz. Regardless of the chosen channel in equation (3.5), the outcome will consistently be an integer multiple of 2π. Therefore, considering the restoration of all phases from the arctan function, the presence of multiple 2π values does not yield any distinction, and it can be concluded that the phases of these eight samples are identical.

However, as depicted in Fig.2.3, the eight samples obtained during the reference period exhibit a rapid oscillation within the range of $-\pi$ to $+\pi$. The presence of frequency deviation, around 500kHz, is indicated by the oscillation in phases originating from the same antenna. The phase difference between the two reference samples has now been altered as:

$$\begin{aligned} \triangle\Phi &= 2\pi \times (f_c + f_o) \times T \\ &= 2\pi \times (2402 \times 10^3 + 500 + \varepsilon)kHz \times 1 \times 10^{-6}s \\ &= 2\pi N + \pi + 2\pi\varepsilon \times 10^{-6} \end{aligned} \tag{3.6}$$

where ε is the error from the ideal frequency deviation 500kHz. Comparing (3.5) and (3.6), it is evident that the offset f_o plays a significant role in accumulating effects on the phases of the reference antenna. Specifically, the cumulative effect is about equal to π when the data rate f_{data} is set to 2 Mb/s.

We assume that the frequency offset aside the standard deviation, i.e. ε, is constant within each CTE data packet.

3.2.1. Phase Flip

Because no antenna switching occurs during the reference period, the phase should rise monotonically with time according to (3.6). However, due to the limitation of the arctan function in MATLAB, such growing may be interrupted, and the phase may flip back around 0 once it exceeds 2π.

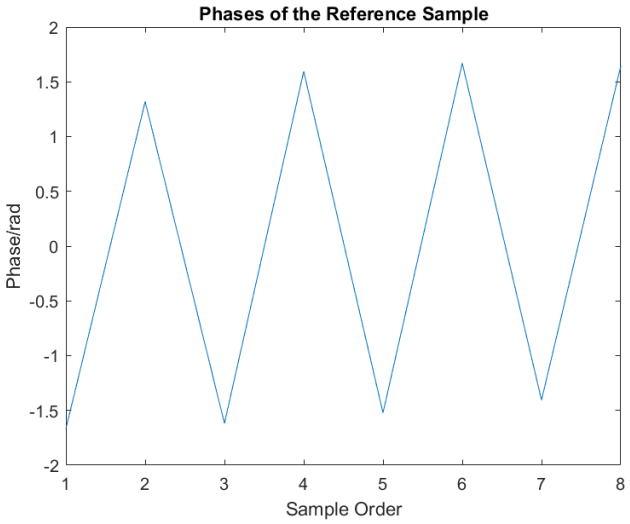

Figure 3.1: Illustration of Phases from the Reference Samples.

As shown in Fig.3.1, there is a jigsaw kind of fluctuation in the figure.

Moreover, if the deviation is perfectly 500kHz with the reference sampling rate of 1×10^6 Hz, then every 2 samples should be of the same phase even with the phase flip. However, this expectation is not met. This slight non-periodic error is accumulated by the errors alongside the standard deviation itself.

In order to visualize the accumulation of phases with time and thus estimate the frequency offset, process the data as follows:

It is clear that the phases are increasing monotonically and almost linearly rather than being unchanged as in (3.5). As previously stated, the slope of the line in Fig.3.2 is primarily caused by uncertainty around the standard deviation. The next step is to calculate the slope, which is the frequency deviation that matters.

Algorithm 1 Phase Flip Processing

Input: The vector ϕ contains all the phases directly calculated from reference IQ samples.

$i = 1$
$N = 8$
count $= 0$
$\phi_{copy} = \phi$
while $i \leq N - 1$ **do**
  if $\phi_{copy}(i+1) \leq \phi_{copy}(i)$ **then**
    count $=$ count $+ 1$
  end if
  $\phi(i+1) = \phi_{copy}(i+1) + 2\pi \times$ count
end while

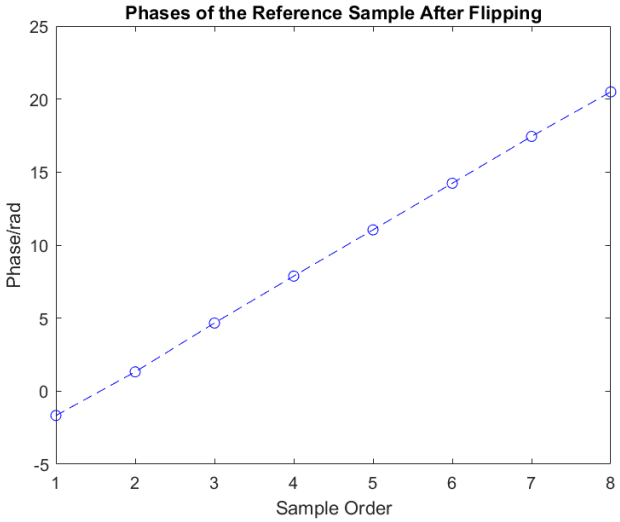

Figure 3.2: Illustration of Phases After Flipping Process.

In prior studies conducted by Yao and Cloudt, a multitude of CFO estimators were presented [7][8]. However, further research suggests that the CFO is subject to corruption by white Gaussian noise, which may not be a reasonable assumption in this context. In this part, we will introduce some basic estimate approaches.

3.2.2. TI Method

Unlike the two methods that will be introduced later, which only utilized a limited number of reference samples, the TI method is the default method by Texas Instrument and is applied in the Round Robin pattern to compensate the phase error caused by frequency offset on all samples and switch slots locally.

In the case of ULA, the phase difference between two adjacent antennas is directly related to AoA. The compensated phase difference between antenna i and antenna j ($i < j$) is computed as:

$$\hat{\triangle\phi_{ij}} = \triangle\phi_{ij} + \frac{|j-i| \triangle \phi_{i(i-M)}}{M} \tag{3.7}$$

where $\hat{\triangle\phi_{ij}}$ is the estimated phase difference, while $\triangle\phi_{ij}$ is the actual measurement, and M the total number of antennas. The compensated error $\frac{|j-i|\triangle\phi_{i(i-M)}}{M}$ is the phase difference of the same antenna over two adjacent loops of sampling $\triangle\phi_{i(i-M)}$ normalized by the total M samples to get the error between two slots. Since the error is assumed to be constant, for i-th and j-th antennas, the error unit is multiplied by $|j-i|$. The frequency offset can be derived from such a phase error:

$$\hat{f_o} = \frac{1}{2\pi(2T_{slot})}\varepsilon \tag{3.8}$$

This is quite similar to the Maximum Likelihood estimator introduced earlier this section.

In [8], the TI method was applied in the ULA case. However, for URA, for antennas placed in different directions, the phase difference values are not expected to be the same. Assume $i_1 = 4$, $j_1 = 6$, and $i_2 = 7$, $j_2 = 9$ as antenna numbers shown in Fig.2.6. Although both groups have a $2T_{slot}$ period in between, the expected phase difference is not the same as they are placed in different lines of a linear array'. For the (i_1,j_1) group, the phase difference:

$$\triangle\phi_{i_1,j_1} = (e^{j2\pi f_{real}4\triangle T}e^{-j2\pi\frac{d}{\lambda}(3\cos\phi\cos\theta+\sin\phi\cos\theta)} - e^{j2\pi f_{real}2\triangle T}e^{-j2\pi\frac{d}{\lambda}(2\cos\phi\cos\theta)})s(t) \tag{3.9}$$

and for (i_2,j_2) group, the phase difference:

$$\triangle\phi_{i_2,j_2} = (e^{j2\pi f_{real}6\triangle T}e^{-j2\pi\frac{d}{\lambda}(3\cos\phi\cos\theta+2\sin\phi\cos\theta)} - e^{j2\pi f_{real}8\triangle T}e^{-j2\pi\frac{d}{\lambda}(2\cos\phi\cos\theta+3\sin\phi\cos\theta)})s(t) \tag{3.10}$$

Thus, it is not practical using the sample and switch data to directly compensate the phase. In the following subsections, only two estimators only using the reference samples will be introduced.

3.2.3. Maximum Likelihood Estimation

The maximum likelihood estimator for CFO is first brought up by Moore for Orthogonal Frequency Division Multiplexing (OFDM) [31] and is applied to BLE scenario by Yao [7]. After compensation, since the slope of phase for the same antenna is assumed to be constant, the samples can be divided into two halves and then applied for estimation. Yao used the Return-to-First antenna switching pattern in ULA to increase the number of samples from the reference antenna [7].

However, in the case of the URA, the total number of antennas is often more. The Return-to-First pattern would compromise the number of overall snapshots for the CFO estimation to ensure each antenna has adequate snapshots. As a result, in this project, we use the standard Round-Robin switch pattern and only use samples from the reference period, i.e. the first eight samples. Because the time interval in the sample and switch slots is substantially bigger with such a switch pattern than the reference period with switch slots in between and sampling on other antennas. Even if they come from the same antenna, they suffer from more severe errors since the sample time may not be at the exact time instants.

The general MLE frequency estimator divides the reference samples into two halves with the same length,

$$f_o = \frac{1}{2\pi\triangle T}\tan^{-1}\frac{\sum_{i=1}^{L} Im(\mathbf{t}^*[i]\,\mathbf{t}[i+L])}{\sum_{i=1}^{L} Re(\mathbf{t}^*[i]\,\mathbf{t}[i+L])} \tag{3.11}$$

where $\mathbf{t}[i]$ denotes the i-th sample in the whole sequence $\mathbf{t}$, L is the length of one-half of the data, * denotes the conjugate operation, and $\triangle T$ is the time difference of the samples L length apart. Basically, this is an average over the phase difference between two halves, as the slope is assumed to be linear and constant.

The error in (3.11) is on the operator of arctan. In general, the phase difference between samples separated by the same time should be near to zero. However, because of the error contributed to the standard deviation, it cannot be assured that the ratio $\frac{\sum_{i=1}^{L} Im(\mathbf{t}^*[i]\mathbf{t}[i+L])}{\sum_{i=1}^{L} Re(\mathbf{t}^*[i]\mathbf{t}[i+L])}$ following the arctan operator will not flip across 2π, even if the ratio values themselves are near.

Thus, the conventional MLE estimator was improved by calculating the circular mean [8]:

$$f_o = \frac{1}{2\pi\triangle T}\arg\left(\sum_{i=0}^{L-1}\mathbf{t}^*[i]\mathbf{t}[i+L]\right) \tag{3.12}$$

where arg represents the phase computation operator.

Although more samples from the reference antenna were included in later sample slots for ULA in [7], the maximum CFO that can be computed without the fail of phase flip is considerably less bounded due to the larger time gap between samples in sample slots from the same antenna. Furthermore, in the case of URA, which naturally involves more antennae, the number of samples from the same antenna is more constrained, resulting in less improvement in estimate performance. As a result, in our study, we exclusively use samples from the reference period.

3.2.4. Least Square Method

The Least Squares approach seeks to minimize the sum of squared errors between the observed and estimated values [32] as

$$\min \|\mathbf{y} - \mathbf{Tb}\|^2 \tag{3.13}$$

where **y** is the observed phase values, **T** here is the matrix containing the sampling time, and b is the parameter of the line to be estimated. If **T** satisfies the full rank condition then the estimator is given by

$$\mathbf{b} = \mathbf{T}^{\dagger}\mathbf{y} \tag{3.14}$$

$$= (\mathbf{T}^T\mathbf{T})^{-1}\mathbf{T}^T\mathbf{y} \tag{3.15}$$

In particular, in the case of linear curve fitting, when the curve is represented as $y = kt + b$ with parameters $[k, b]$ with the observed data set $[(t_1, y_1), (t_2, y_2), \cdots, (t_{N_o}, y_{N_o})]$, the least squares issue is written as:

$$\begin{bmatrix} 1 & t_1 \\ 1 & t_2 \\ \cdots & \cdots \\ 1 & t_{N_o} \end{bmatrix} \begin{bmatrix} b \\ k \end{bmatrix} = \begin{bmatrix} y_1 \\ y_2 \\ \cdots \\ y_{N_o} \end{bmatrix} \tag{3.16}$$

where $N_o = 8$ is the total number of reference samples we use, and k is the slope of the estimated curve. What's worth noting is that $k \neq f_o$ since the slope only shows the phase difference over a single reference slot. The frequency offset can be calculated from k as follows:

$$f_o = \frac{k}{2\pi T_{ref}} \tag{3.17}$$

where $T_{ref} = 1 \times 10^{-6}$ is the reference sample period. Another way of solving the slope of the curve explicitly is:

$$k = \frac{\sum_{i=1}^{M}(t[i] - \bar{a})(t[i] - \bar{y})}{\sum_{i=1}^{M}(t[i] - \bar{t})^2} \tag{3.18}$$

where $\bar{t}$ and $\bar{y}$ are the mean values of the time sequence **t** and phase sequence **y**. Then apply (3.17) on the estimated k.

3.3. Frequency Offset Estimation Impact on Angle Estimation

After the calculation of the frequency offset f_o, the compensation is performed by generating the offset matrix as shown in (2.25) and then multiplying the data matrix with its inverse:

$$\hat{\mathbf{X}} = \hat{\mathbf{O}}^{-1}\mathbf{X} \tag{3.19}$$

where $\hat{\mathbf{X}}$ is the estimation of the compensated data matrix computed from the data matrix **X** that is collected with antenna switching.

Assume the error in frequency offset estimation is ϵ, then the compensated data becomes:

$$\begin{aligned} \hat{\mathbf{X}} &= \hat{\mathbf{O}}^{-1}\mathbf{X} \\ &= \hat{\mathbf{O}}^{-1}\mathbf{OAS} \\ &= \text{diag}(1, e^{-j2\pi(f_c+f_o+\epsilon)\triangle T}, e^{-j2\pi(f_c+f_o+\epsilon)2\triangle T}, \cdots, e^{-j2\pi(f_c+f_o+\epsilon)M\triangle T}) \cdot \\ &\quad \text{diag}(1, e^{-j2\pi(f_c+f_o)\triangle T}, e^{-j2\pi(f_c+f_o)2\triangle T}, \cdots, e^{-j2\pi(f_c+f_o)M\triangle T})\mathbf{AS} \end{aligned} \tag{3.20}$$

$$= \text{diag}(1, e^{-j2\pi\epsilon\triangle T}, e^{-j2\pi\epsilon 2\triangle T}, \cdots, e^{-j2\pi\epsilon M\triangle T})\mathbf{AS}$$

$$= \mathbf{O}_{\epsilon}\mathbf{AS} \tag{3.21}$$

where $\hat{\mathbf{O}}$ is the estimated diagonal frequency offset matrix, $\mathbf{O}_{\epsilon}$ is the offset error matrix, and $\triangle T$ is the time interval between two adjacent sample slots. Because of the switch slots in between every other sample slot, $\triangle T = 2T_{slot}$. So the impact of the frequency offset error is that it changes the subspace of the steering matrix **A**.

3.4. Cramér-Rao Lower Bound of Frequency Offset Estimation

The Cramér-Rao Lower Bound (CRLB) establishes a lower limit on the variance of an unbiased estimator. According to Kay, estimators that exhibit proximity to the CRLB tend to possess a higher degree of unbiasedness, making them more desirable for practical usage [33].

Given that our model differs from past studies, a comprehensive derivation may be provided in Appendix A. The variance lower bound for an unbiased estimator with a sample rate of $f_s = 1MHz$ is:

$$\text{Var}(\hat{f}_o) \geq \frac{3f_s^2}{8\pi^2 \text{SNR}((MN)^3 - 2(MN) - 2)} \tag{3.22}$$

where $\hat{f}_o$ stands for the estimation of the frequency offset, MN is the total number of antennas in the data model, and SNR $= \frac{1}{\sigma^2}$ is as defined in the Appendix, while in other plots the SNR values are in the unit of dB SNR $= -10 \log_{10} \sigma^2$

However, since we only use samples from the reference period for estimating CFO, (3.22) is changed for only one antenna involved. From AppendixA, the CRLB for estimating CFO by only reference samples is:

$$\text{Var}(\hat{f}_o) \geq \frac{3f_s^2}{2\pi^2 \text{SNR}(N_R^3 - N_R)} \tag{3.23}$$

where $N_R = 8$ is the number of samples in the reference period. It is obvious that such a CRLB value would be lower with more samples involved, i.e., with a larger N_R. And the BLE data structure constrains the lowest error using an unbiased estimator.

In Fig.3.3, two estimators are applied with signals corrupted in different SNR levels of white Gaussian noise. The errors are computed in the form of root-mean-square-error (RMSE):

$$\text{RMSE} = \sqrt{\frac{\sum_{i=1}^{N}(f_o - \hat{f}_o)^2}{N}} \tag{3.24}$$

where f_o is the true value which differs from each packet, $\hat{f}_o$ is the estimated value, and N = 100000 is the number of Monte-Carlo iterations for each SNR value. In general, the LS estimator tends to exhibit superior performance compared to the MLE technique. The final algorithm utilizes the LS estimator.

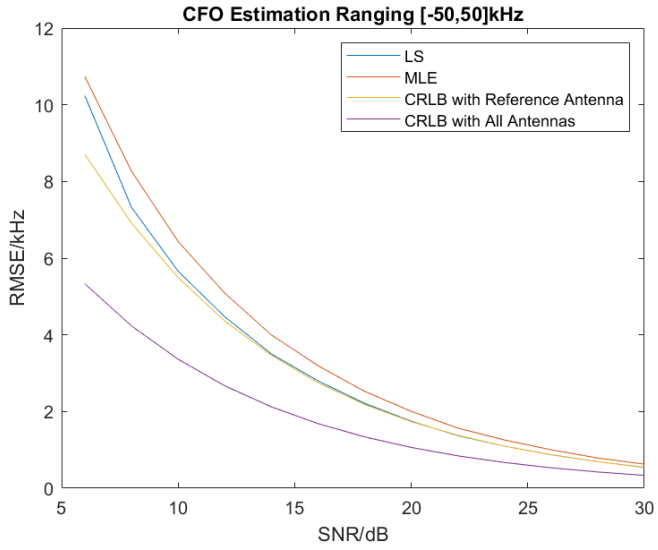

(a) With CFO Range of ± 50kHz

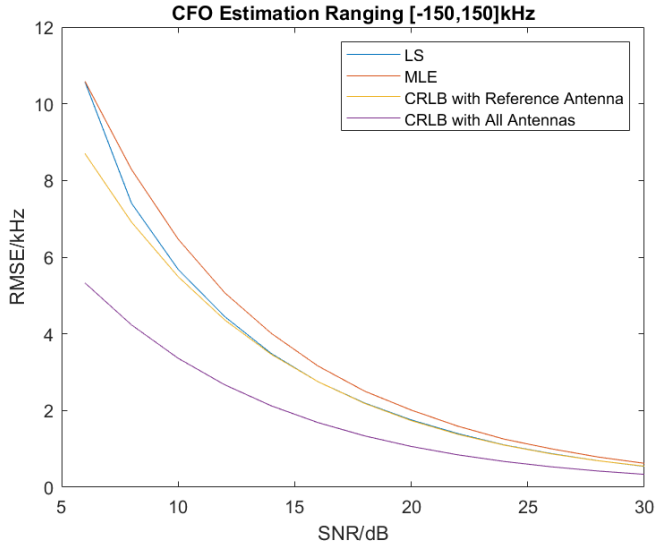

(b) With CFO Range of ± 150kHz

Figure 3.3: RMSE Comparison of Two Estimators and CRLB

3.5. Conclusion

In this chapter, we explain the concept of CFO and its generation mechanisms. Two estimators: the Least Square estimator and the Maximum Likelihood estimator, are introduced. By exclusively utilizing the samples within the reference period, we are able to estimate the frequency deviation. Next, both the estimators are compared with the CRLB of CFO estimation under varying SNR values. The results indicate that with higher SNR the RMSE would be lower, aligning with the expectation. Finally, the LS estimator is selected for the AoA estimation algorithm due to its superior performance in general compared to MLE.

Following the estimation of f_o, we construct the CFO matrix as described in (2.25) and calculated the compensated data matrix $\hat{\mathbf{X}}$. The compensated data matrix, denoted as $\hat{\mathbf{X}}$ and previously presented in (3.19), represents the data sampled from the array at the same time instants. This matrix will be utilized in subsequent direction-finding algorithms for further processing. The impact of CFO estimating errors on the angle estimation will be discussed in later chapters.

4

Direction Finding Algorithms

4.1. MUSIC

The Multiple Signal Classification (MUSIC) algorithm is widely recognized as one of the most commonly employed techniques for direction-finding [2]. MUSIC is a subspace-based method that aims to identify the optimal angle (or combination of angles in a two-dimensional setting) that maximizes the separation between the antenna steering vector and the noise subspace.

The first step is to calculate the covariance matrix.

$$\mathbf{R_X} = \mathrm{E}\left\{\mathbf{X}\mathbf{X}^H\right\} \tag{4.1}$$

where $\mathbf{X}$ is the observed data matrix. In a practical case, the expectation is calculated by averaging all snapshots of the data. Recall the assumption we made, namely that the signal and the noise are uncorrelated to each other, and that the noise is temporally and spatially white. Thus, the sampled covariance matrix $\hat{\mathbf{R}}_\mathbf{X}$ can be calculated as:

$$\begin{aligned}
\hat{\mathbf{R}}_\mathbf{X} &\doteq \frac{1}{N}\mathbf{X}\mathbf{X}^H \\
&= \frac{1}{N}\left(\mathbf{A}\mathbf{S} + \mathbf{N}\right)\left(\mathbf{A}\mathbf{S} + \mathbf{N}\right)^H \\
&= \frac{1}{N}\left(\mathbf{A}\mathbf{S}\mathbf{S}^H\mathbf{A}^H\right) + \frac{1}{N}\mathbf{N}\mathbf{N}^H \\
&= \mathbf{A}\hat{\mathbf{R}}_\mathbf{S}\mathbf{A}^H + \sigma^2\mathbf{I}
\end{aligned} \tag{4.2}$$

where σ^2 represents the variance of noise, $\mathbf{I}$ is an identity matrix with a size $M_T \times M_T$ with M_T antennas, $\mathbf{R_S}$ is the sampled covariance matrix of the signal, the superscript H denotes the operation of computing the Hermitian form of the matrix, and here N stands for the number of snapshots. Cross-terms of expectation of signal and noise are cancelled because of the assumption that the signal and the noise are independent.

Then we start the subspace analysis of the sample covariance matrix. The eigendecomposition of $\hat{\mathbf{R}}_\mathbf{X}$ is

$$\hat{\mathbf{R}}_\mathbf{X} = \mathbf{U}\Lambda\mathbf{U}^H \tag{4.3}$$

where matrix $\mathbf{U}$ is the $M_T \times M_T$ eigenvector matrix with normalized eigenvectors as its columns, and Λ is $M_T \times M_T$ diagonal matrix with corresponding eigenvalues in non-increasing order. The eigenvectors can be divided into distinct signal and noise subspaces, since they are considered uncorrelated to each

other. Then (4.3) can be expressed as follows

$$\begin{aligned}\hat{\mathbf{R}}_{\mathbf{X}} &= \mathbf{U}\mathbf{\Lambda}\mathbf{U}^H \\ &= \begin{bmatrix}\mathbf{U_S} & \mathbf{U_N}\end{bmatrix}\begin{bmatrix}\mathbf{\Lambda}_S + \sigma^2\mathbf{I}_K & 0 \\ 0 & \sigma^2\mathbf{I}_{M-K}\end{bmatrix}\begin{bmatrix}\mathbf{U_S}^H \\ \mathbf{U_N}^H\end{bmatrix} \\ &= \mathbf{U_S}\mathbf{\Lambda}\mathbf{U_S}^H + \sigma^2\left(\mathbf{U_S}\mathbf{U_S}^H + \mathbf{U_N}\mathbf{U_N}^H\right) \\ &= \mathbf{U_S}\left(\mathbf{\Lambda}_S + \sigma^2\mathbf{I}_K\right)\mathbf{U_S}^H + \sigma^2\mathbf{U_N}\mathbf{I}_{M-K}\mathbf{U_N}^H \end{aligned} \tag{4.4}$$

where $\mathbf{U_S}$ is the combination of eigenvectors that correspond to the signal subspace, $\mathbf{U_N}$ is the combination of eigenvectors that correspond to the noise subspace. Typically, $\mathbf{U_S}$ is defined as the first K columns of the eigenvector matrix $\mathbf{U}$. Where as $\mathbf{U_N}$ is the last $M_T - K$ columns of $\mathbf{U}$.

It is clear from (4.4) that the subspace spanned by $\mathbf{U_S}$ is equivalent to the subspace spanned by the manifold matrix $\mathbf{A}$. Consequently, $\mathbf{A}$ should be orthogonal to the noise subspace $\mathbf{U_N}$, as $\mathbf{U_S}$ is orthogonal to it because of their independence. The estimation of the angle θ can then be accomplished by searching for a value of θ that maximizes the cost function

$$J(\theta) = \frac{1}{\mathbf{a}(\theta)^H\mathbf{U_N}\mathbf{U_N}^H\mathbf{a}(\theta)} \tag{4.5}$$

where $\mathbf{a}(\theta)$ is the steering vector with a specific value of the angle. In the ULA case, the steering vector refers to the reference antenna is

$$\mathbf{a}(\theta) = \begin{bmatrix} 1 \\ e^{j\frac{2\pi d\cos\theta}{\lambda}} \\ e^{j\frac{2\pi 2d\cos\theta}{\lambda}} \\ \cdots \\ e^{j\frac{2\pi(M-1)d\cos\theta}{\lambda}}\end{bmatrix} \tag{4.6}$$

where θ is defined the same as in Fig.2.7.

4.1.1. 2-D MUSIC

In section 4.1, the notion of 1-D MUSIC is explained. Regarding the 2-D MUSIC algorithm, the processing of the data matrix remains unchanged. However, the structure of steering vector in a 2-D array is different, as shown previously in (2.7). The steering vector is now expressed as:

$$\mathbf{a}(\theta,\phi) = \begin{bmatrix} 1 \\ e^{j\frac{2\pi(d_{x1}\cos\phi + d_{y1}\sin\phi)\cos\theta}{\lambda}} \\ e^{j\frac{2\pi(d_{x2}\cos\phi + d_{y2}\sin\phi)\cos\theta}{\lambda}} \\ \cdots \\ e^{j\frac{2\pi(d_{xM}\cos\phi + d_{yM}\sin\phi)\cos\theta}{\lambda}}\end{bmatrix} \tag{4.7}$$

Then the cost function is to be maximized with respect to both the elevation angle θ and the azimuth angle ϕ, in contrast to the previous 1-D case where only one angle was considered in (4.5). Plot the spectrum as

$$J(\theta,\phi) = \frac{1}{\mathbf{a}(\theta,\phi)^H\mathbf{U_N}\mathbf{U_N}^H\mathbf{a}(\theta,\phi)} \tag{4.8}$$

and search for the combination of the angles that gives the peak in the spectrum.

The main problem of the MUSIC algorithm is its computational complexity as it is scanning across all possible angle combinations[2]. The accuracy of the MUSIC algorithm is directly proportional to the scanning step. The finer the scanning step, the longer the scanning would take, which would be impractical for indoor localization since the target could move in such a amount of time.

4.2. ESPRIT

As previously mentioned, the primary concern regarding the MUSIC algorithm, aside from its limited capability in handling multipath scenarios, lies in its computational cost. Basically, the result of MUSIC

estimation can only be one (or some) of the angles used in scanning with the steering vector $\mathbf{a}(\phi, \theta)$. That is to say, a finer estimation requires more scanning and thus takes up way more time to compute.

In contrast to angle scanning methods such as MUSIC, there is another category of DOA estimate techniques known as search-free algorithms. Examples of search-free algorithms are Root-MUSIC, Root-RARE, and ESPRIT. Given that other search-free approaches require specific array geometries, this paper will solely focus on 2-D ESPRIT as it offers broader applicability.

4.2.1. ESPRIT

The fundamental concept of the ESPRIT algorithm is to exploit the shift-invariance structure in the signal model [34]. In a 1-D scenario, the data model with M_T antennas ULA can be described as

$$\begin{aligned} \mathbf{X} &= \begin{bmatrix} \mathbf{x}_1 \\ \mathbf{x}_2 \\ \vdots \\ \mathbf{x}_{M_T} \end{bmatrix} \\ &= \begin{bmatrix} \mathbf{a}_1(\theta) \\ \mathbf{a}_2(\theta) \\ \vdots \\ \mathbf{a}_{M_T}(\theta) \end{bmatrix} \mathbf{S} \end{aligned} \tag{4.9}$$

where $\mathbf{S}$ is the signal matrix containing all d uncorrelated signals,

$$\mathbf{a}_k(\theta) = \begin{bmatrix} e^{-j\frac{2\pi d}{\lambda}k\cos\theta_1} & e^{-j\frac{2\pi d}{\lambda}k\cos\theta_2} & \cdots & e^{-j\frac{2\pi d}{\lambda}k\cos\theta_d} \end{bmatrix}^T$$

is the steering vector for the k-th antenna and in total d AOA for all sources.

Select the first M-1 rows of data matrix $\mathbf{X}$ as matrix $\mathbf{X}_1$ and the last M-1 rows as matrix $\mathbf{X}_2$, we have

$$\begin{cases} \mathbf{X}_1 = \mathbf{J}_1\mathbf{X} = \mathbf{A}_1(\theta)\mathbf{x} \\ \mathbf{X}_2 = \mathbf{J}_2\mathbf{X} = \mathbf{A}_2(\theta)\mathbf{x} \end{cases} \tag{4.10}$$

where $\mathbf{J}_1$ and $\mathbf{J}_2$ are the selection matrix given by

$$\begin{aligned} \mathbf{J_1} &= \begin{bmatrix} 1 & 0 & \cdots & 0 & 0 \\ 0 & 1 & \cdots & 0 & 0 \\ \vdots & \vdots & \ddots & \vdots & \vdots \\ 0 & 0 & \cdots & 1 & 0 \end{bmatrix} \in \mathbb{R}^{(M_T-1)\times M_T} \\ \mathbf{J_2} &= \begin{bmatrix} 0 & 1 & \cdots & 0 & 0 \\ 0 & 0 & \cdots & 0 & 0 \\ \vdots & \vdots & \ddots & \vdots & \vdots \\ 0 & 0 & \cdots & 0 & 1 \end{bmatrix} \in \mathbb{R}^{(M_T-1)\times M_T} \end{aligned} \tag{4.11}$$

, $\mathbf{A}_1(\boldsymbol{\theta})$ and $\mathbf{A}_2(\boldsymbol{\theta})$ are the steering matrices of these two selected subarrays. Based on the structure of the steering vectors, it can be shown that $\mathbf{A}_1(\boldsymbol{\theta})$ and $\mathbf{A}_2(\boldsymbol{\theta})$ represent neighboring antennas, thereby establishing the following connection:

$$\mathbf{A}_2(\boldsymbol{\theta}) = \mathbf{A}_1(\boldsymbol{\theta})\mathbf{Q}(\boldsymbol{\theta}) \tag{4.12}$$

where

$$\mathbf{Q}(\boldsymbol{\theta}) = \text{diag}\left\{ e^{j\frac{2\pi d_x}{\lambda}\sin\theta_1}, \quad e^{j\frac{2\pi d_x}{\lambda}\sin\theta_2}, \quad \cdots, \quad e^{j\frac{2\pi d_x}{\lambda}\sin\theta_d} \right\} \tag{4.13}$$

which contains the target angle-related information that could be easily converted into angle values. The relation between the diagonal element ϕ_i and the associated angle θ_i is

$$\theta_i = -\frac{\lambda}{2\pi d_x}\arcsin(\arg(\phi_i)) \tag{4.14}$$

Examine the structure of the noise-free covariance matrix $\mathbf{R_x} = \frac{1}{N}\mathbf{A}(\theta)\mathbf{R_s}\mathbf{A^T}(\theta)$. Apply eigen-decomposition to $\mathbf{R_x}$ and the matrix of eigenvectors is $\mathbf{E_s}$. Given the assumption of the incoherent signals, it can be inferred that the subspaces spanned by $\mathbf{E_s}$ and $\mathbf{A}(\theta)$ are equivalent. Hence, there is a nonsingular invertible transformation matrix $\mathbf{T}$ that fulfills:

$$\mathbf{E_s} = \mathbf{A}(\theta)\mathbf{T} \tag{4.15}$$

By calculating the covariance matrix and determining the eigenvectors using the given data vectors $\mathbf{x}_1$ and $\mathbf{x}_2$, the following results are obtained:

$$\mathbf{E_{s1}} = \mathbf{J_1}\mathbf{E_s} = \mathbf{J_1}\mathbf{A}(\boldsymbol{\theta})\mathbf{T} = \mathbf{A_1}(\boldsymbol{\theta})\mathbf{T} \tag{4.16}$$

$$= \mathbf{A_2}(\boldsymbol{\theta})\mathbf{Q}(\boldsymbol{\theta})\mathbf{T} = \mathbf{E_{s2}}\mathbf{T^{-1}}\mathbf{Q}(\boldsymbol{\theta})\mathbf{T} = \mathbf{E_{s2}}\boldsymbol{\Psi} \tag{4.17}$$

where

$$\boldsymbol{\Psi} = \mathbf{E_{s2}}^{\dagger}\mathbf{E_{s1}} \tag{4.18}$$

has the structure of eigen-decomposition and shares the same eigenvalues as the target matrix $\mathbf{Q}(\theta)$.

The typical 1-D ESPRIT method consists of the following steps:

- Determine the shift-invariance structure of the data matrix.
- Select the first and the last M-1 rows of the data matrix as specified in (4.10).
- Compute the eigen-decomposition on these two subarray data matrices and the results are denoted as $\mathbf{E_{s1}}$ and $\mathbf{E_{s2}}$.
- Compute the $\boldsymbol{\Psi}$ matrix according to (4.18).
- Apply eigen-decomposition on $\boldsymbol{\Psi}$.
- Recover the angles from eigenvalues extracted from the previous result.

4.2.2. Unitary ESPRIT

In wireless communication, the signals are all complex numbers, which add complexity to the eigendecomposition. The unitary ESPRIT algorithm converts the entire dataset into the real number domain, resulting in a significant reduction in complexity [35].

A significant requirement for a matrix to be transposed is that its geometry should be conjugate centro-symmetric. $\mathbf{\Pi}_n$ is the notation for the $n \times n$ anti-diagonal identity matrix, with 1 along its anti-diagonal and 0 elsewhere, i.e.

$$\mathbf{\Pi}_n = \begin{bmatrix} & & 1 \\ & 1 & \\ \cdots & & \\ 1 & & \end{bmatrix} \in \mathbb{R}^{n\times n} \tag{4.19}$$

Left-multiplying a matrix with $\mathbf{\Pi}_n$ equals reversing all the rows in the original matrix, while right-multiplying means reversing all the columns. If a matrix $\mathbf{Q}$ satisfies

$$\mathbf{\Pi}_n\mathbf{Q}^H = \mathbf{Q} \tag{4.20}$$

then it is called $\mathbf{\Pi}$-real, which is equivalent to conjugate centro-symmetric.

In unitary ESPRIT, at first, two sparse unitary matrices that would be used later are defined depending on whether the size is an odd number or an even one. The even version $\mathbf{Q}_{2n}$ is given as

$$\mathbf{Q}_{2n} = \frac{1}{\sqrt{2}}\begin{bmatrix} \mathbf{I}_n & j\mathbf{I}_n \\ \mathbf{\Pi}_n & -j\mathbf{\Pi}_n \end{bmatrix} \tag{4.21}$$

The odd version Q_{2n+1} is given as

$$\mathbf{Q}_{2n+1} = \frac{1}{\sqrt{2}}\begin{bmatrix} \mathbf{I}_n & \mathbf{0} & j\mathbf{I}_n \\ \mathbf{0}^T & \sqrt{2} & \mathbf{0}^T \\ \mathbf{\Pi}_n & \mathbf{0} & -j\mathbf{\Pi}_n \end{bmatrix} \tag{4.22}$$

where $\mathbf{0}$ is a vector of size n$\times 1$ whose elements are all 0.

With a given complex-number data matrix $\mathbf{X} \in \mathbb{R}^{M\times N}$, the transformation is given as

$$\mathcal{T}(\mathbf{X}) = \mathbf{Q}_M^H \begin{bmatrix} \mathbf{X} & \mathbf{\Pi}_M \bar{\mathbf{X}} \mathbf{\Pi}_N \end{bmatrix} \mathbf{Q}_{2N} \in \mathbb{R}^{M\times 2N} \tag{4.23}$$

Formulate the $\mathbf{E}_s$ matrix by selecting the largest d left eigenvectors of $\mathcal{T}(\mathbf{X})$. The relationship between the complex signal subspace matrix $\mathbf{U}_s$ and $\mathbf{E}_s$ is that

$$\mathbf{U}_s = \mathbf{Q}_M \mathbf{E}_s \tag{4.24}$$

And now the shift-invariance property to be investigated is in the transformed steering matrix $\mathbf{D}$

$$\mathbf{D} = \mathbf{Q}_M^H \mathbf{A} = \begin{bmatrix} \mathbf{d}(\theta_1) & \mathbf{d}(\theta_2) & \cdots & \mathbf{d}(\theta_d) \end{bmatrix} \in \mathbb{R}^{M\times d} \tag{4.25}$$

Since the transformation is a linear operation, the shift-invariance property remains, i.e.

$$\mathbf{K_1} \mathbf{D} \mathbf{\Omega} = \mathbf{K_2} \mathbf{D} \tag{4.26}$$

where $\mathbf{\Omega} = \text{diag}\left\{\tan(\frac{\mu_i}{2})\right\}_{i=1}^{d}$ is the target diagonal matrix containing the angle information, and $\mu_i = -\frac{2\pi d_x}{\lambda} \sin\theta_i$. What is worth noting is that the relationship between the elements in the target matrix and the actual angle values changes after the transformation.

Besides, both the steering matrix and the selection matrix are also transformed. The transformed selection matrices $\mathbf{K_1}$ and $\mathbf{K_2}$ are given by

$$\mathbf{K_1} = 2 \cdot \text{Re}\left\{\mathbf{Q_{M-1}^H J_2 Q_M}\right\} \tag{4.27}$$

$$\mathbf{K_2} = 2 \cdot \text{Im}\left\{\mathbf{Q_{M-1}^H J_2 Q_M}\right\} \tag{4.28}$$

where Re· and Im· represent the operations of extracting the real and imaginary parts of the complex number inside the brackets, respectively.

Similar to the conventional complex number case, t can be observed that the transformed steering matrix $\mathbf{D}$ and the transformed signal subspace matrix $\mathbf{E_s}$ span the same signal subspace. Thus, there must be a nonsingular transform matrix $\mathbf{T}$ that fulfills $\mathbf{D} = \mathbf{E_s T}$. Substitute the relationship into the shift-invariance equation (4.26), we obtain

$$\mathbf{K_1 E_s} \mathbf{\Upsilon} = \mathbf{K_2 E_s} \in \mathbb{R}^{(M-1)\times d} \tag{4.29}$$

where $\mathbf{\Upsilon} = \mathbf{T\Omega T}^{-1}$ whose eigenvalues are the same as the target matrix $\mathbf{\Omega}$. $\mathbf{\Upsilon}$ can be constructed as (4.18) in the least square way.

4.2.3. 2-D Unitary ESPRIT

In the 2-D scenario, it is necessary to have two distinct target diagonal matrices that include different angle information, as two angles need to be estimated. As can be seen from the array geometry, smoothing along the x-axis and the y-axis exploits the shift-invariance property in these two directions. Consider the 7×7 URA case; the process of selecting subarrays is depicted in Fig.4.1. In the figure, $\mathbf{J}_{\mu 1}$ and $\mathbf{J}_{\mu 2}$ denote two subarrays along the x-direction, $\mathbf{J}_{v1}$ and $\mathbf{J}_{v2}$ denote two subarrays along the y-direction, $M_x = 7$ and $M_y = 7$ represent the number of antennas in two directions, respectively, and the total number of antennas in the whole array is $M = M_x \times M_y$.

The next step is to construct the 2-D selection matrices. First, two 2-D selection matrices are defined the same in (4.10), denoted as $\mathbf{J}_1^7 \in \mathrm{R}^{6\times 7}$ and $\mathbf{J}_2^7 \in \mathrm{R}^{6\times 7}$ as $M_x = M_y = 7$. The superscript shows the size of the 2-D selection matrices in case $M_x \neq M_y$. All 2-D selection matrices can then be derived with them and some corresponding identity matrices. However, not all of them are specifically required, as shown in later parts.

$$\begin{aligned} \mathbf{J}_{\mu 1} &= \mathbf{I}_{M_y} \otimes \mathbf{J}_1^{M_x} \\ \mathbf{J}_{\mu 2} &= \mathbf{I}_{M_y} \otimes \mathbf{J}_2^{M_x} \\ \mathbf{J}_{v1} &= \mathbf{J}_1^{M_y} \otimes \mathbf{I}_{M_x} \\ \mathbf{J}_{v2} &= \mathbf{J}_2^{M_y} \otimes \mathbf{I}_{M_x} \end{aligned} \tag{4.30}$$

which, if implemented on the steering matrix, satisfy

$$\begin{aligned} \mathbf{J}_{\mu 1}\mathbf{A} &= \mathbf{J}_{\mu 2}\mathbf{A}\mathbf{\Phi}_\mu \\ \mathbf{J}_{v1}\mathbf{A} &= \mathbf{J}_{v2}\mathbf{A}\mathbf{\Phi}_v \end{aligned} \tag{4.31}$$

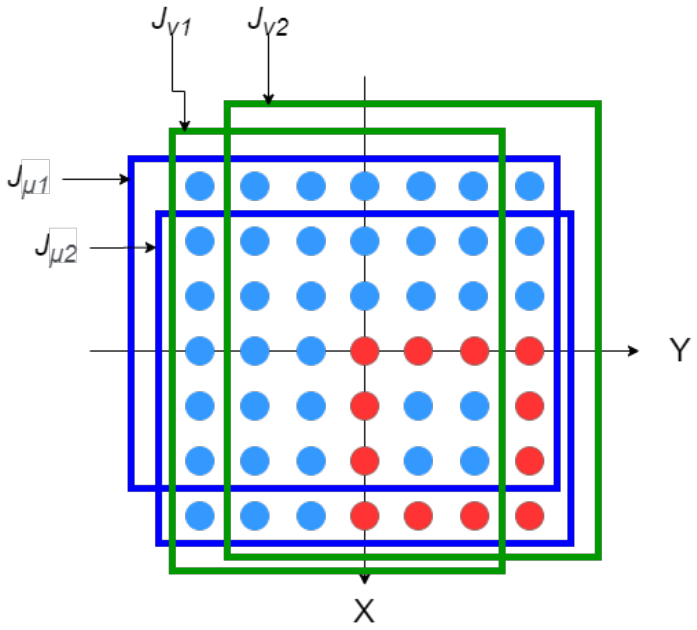

Figure 4.1: Illustration of ESPRIT Subarrays in a 7×7 Virtual URA.

where the diagonal matrices contain the angle information.

$$\begin{aligned} \mathbf{\Phi_\mu} &= \text{diag}\left\{e^{j\frac{2\pi d_x}{\lambda}\cos\phi_i\cos\theta_i}\right\}_{i=1}^{d} \\ \mathbf{\Phi}_v &= \text{diag}\left\{e^{j\frac{2\pi d_y}{\lambda}\sin\phi_i\cos\theta_i}\right\}_{i=1}^{d} \end{aligned} \tag{4.32}$$

Just like the 1-D case, then all selection matrices are transformed as

$$\begin{aligned} \mathbf{K}_{\mu 1} &= 2\cdot\text{Re}\left\{\mathbf{Q}_{M_x}^H\mathbf{J}_{\mu 2}\mathbf{Q}_M\right\} \\ \mathbf{K}_{\mu 2} &= 2\cdot\text{Im}\left\{\mathbf{Q}_{M_x}^H\mathbf{J}_{\mu 2}\mathbf{Q}_M\right\} \\ \mathbf{K}_{v1} &= 2\cdot\text{Re}\left\{\mathbf{Q}_{M_y}^H\mathbf{J}_{v2}\mathbf{Q}_M\right\} \\ \mathbf{K}_{v2} &= 2\cdot\text{Im}\left\{\mathbf{Q}_{M_y}^H\mathbf{J}_{v2}\mathbf{Q}_M\right\} \end{aligned} \tag{4.33}$$

and the transformed $\mathbf{\Phi_\mu}$ and $\mathbf{\Phi}_v$ as

$$\begin{aligned} \mathbf{\Phi_\mu} &= \text{diag}\left\{tan(\tfrac{2\pi d_x}{\lambda}\cos\phi_i\cos\theta_i/2)\right\}_{i=1}^{d} \\ \mathbf{\Phi_v} &= \text{diag}\left\{tan(\tfrac{2\pi d_y}{\lambda}\sin\phi_i\cos\theta_i/2)\right\}_{i=1}^{d} \end{aligned} \tag{4.34}$$

The signal subspace eigenvectors $\mathbf{E_s}$ are again selected from the eigenvectors of the covariance matrix, which correspond to the d largest eigenvalues. With the data after spatial smoothing, only the covariance matrix $\mathbf{R}$, not the data itself are known. $\mathbf{E_s}$ is then computed from the real-valued covariance matrix $\mathbf{R}_{real}$ which is

$$\mathbf{R}_{real} = \text{Re}\left\{\mathbf{Q}_M^H\mathbf{R}\mathbf{Q}_M\right\} \tag{4.35}$$

Since the transformed steering matrix $\mathbf{D} = \mathbf{Q}_M^H\mathbf{A}$ should span the same subspace as $\mathbf{E_s}$, there is a nonsingular transformation matrix $\mathbf{T}$ satisfies $\mathbf{D} = \mathbf{E}_s\mathbf{T}$. The 2-D version of (4.29) is

$$\begin{aligned} \mathbf{K_{\mu 1}E_s} &= \mathbf{K_{\mu 2}E_s}\mathbf{\Upsilon_\mu} \\ \mathbf{K_{v1}E_s} &= \mathbf{K_{v2}E_s}\mathbf{\Upsilon_v} \end{aligned} \tag{4.36}$$

where $\mathbf{\Upsilon_\mu} = \mathbf{T\Omega_\mu T}^{-1}$ and $\mathbf{\Upsilon}_v = \mathbf{T\Omega}_v\mathbf{T}^{-1}$ are the target diagonal matrices.

However, instead of solving (4.36) separately, since $\boldsymbol{\Upsilon}_\mu$ and $\boldsymbol{\Upsilon}_v$ share the same eigenvectors from $\mathbf{T}$, they can be solved together through automatic pairing them together [34], i.e.

$$\boldsymbol{\Upsilon}_{\boldsymbol{\mu}} + j\boldsymbol{\Upsilon}_v = \mathbf{T}(\boldsymbol{\Omega}_{\boldsymbol{\mu}} + j\boldsymbol{\Omega}_v)\mathbf{T}^{-1} \tag{4.37}$$

After gaining $\boldsymbol{\Omega}_{\boldsymbol{\mu}}$ and $\boldsymbol{\Omega}_v$ from the real and imaginary parts of the eigenvalues, respectively, the angle values can be recovered.

4.3. Multipath Mitigation

Multipath effects are a prominent source of error in the context of indoor localization. The rank of the data covariance matrix is diminished by the presence of multipath signals, particularly in the case of subspace algorithms such as MUSIC and ESPRIT. In the basic idea of MUSIC, the signal space is spanned of steering vectors only when the signal matrix has full rank. This is due to the fact that the multipath signal essentially represents an delayed and attenuated version of the LOS signal. This section begins with discussing the impact of multipath signals on the rank of the covariance matrix, followed by an introduction to several techniques employed for mitigating the effects of multipath.

Recall that the multipath signals are in the form of:

$$\begin{aligned}\mathbf{s}(t) &= \begin{bmatrix} 1 \\ \alpha_1 e^{-\tau_1} \\ \vdots \\ \alpha_{K-1} e^{-\tau_{K-1}} \end{bmatrix} \mathbf{s}_0(t) \\ &= \boldsymbol{\Gamma}\mathbf{s}_0(t)\end{aligned} \tag{4.38}$$

where α indicates the attenuation in amplitude, τ indicates the phase delay introduced by distances between each antenna and the transmitter, and $\mathbf{s}_0(t)$ is the LOS signal of interest. (4.38) shows the multipath signals can be expressed as a linear combination $\boldsymbol{\Gamma}$ of the LOS signal. Then the data received at the antenna array at this instant is

$$\begin{aligned}\mathbf{x}(t) &= \mathbf{A}(\boldsymbol{\theta}, \boldsymbol{\phi})\mathbf{s}(t) \\ &= \mathbf{A}(\boldsymbol{\theta}, \boldsymbol{\phi})\boldsymbol{\Gamma}\mathbf{s}_0(t)\end{aligned} \tag{4.39}$$

where $\mathbf{A}(\boldsymbol{\theta}, \boldsymbol{\phi})$ is the directional antenna steering matrix explicitly explained in (2.15).

Now consider the sample covariance matrix $\hat{\mathbf{R}_X}$, which is calculated from the observed data matrix $\mathbf{X}$.

$$\begin{aligned}\hat{\mathbf{R}_X} &\doteq \frac{1}{N}\mathbf{X}\mathbf{X}^H \\ &= \frac{1}{N}\left(\mathbf{A}\boldsymbol{\Gamma}\mathbf{s}_0 + \mathbf{N}\right)\left(\mathbf{A}\boldsymbol{\Gamma}\mathbf{s}_0 + \mathbf{N}\right)^H \\ &= \frac{1}{N}\left(\mathbf{A}\boldsymbol{\Gamma}\mathbf{s}_0\mathbf{s}_0^H\boldsymbol{\Gamma}^H\mathbf{A}^H\right) + \frac{1}{N}\mathbf{N}\mathbf{N}^H \\ &= \mathbf{A}\boldsymbol{\Gamma}\hat{\mathbf{R}}_{s_0}\boldsymbol{\Gamma}^H\mathbf{A}^H + \sigma^2\mathbf{I}\end{aligned} \tag{4.40}$$

Given that $\mathbf{s}_0$ represents a one-row vector comprising N snapshots of LOS data, it is evident that $\hat{\mathbf{R}}_{s_0}$ is a rank-1 matrix in this scenario with perfect coherence. Then with the MUSIC algorithm, only one direction of arrival would be detected instead of all K signals. And since the steering matrix for LOS signals is now $\mathbf{A}(\boldsymbol{\theta}, \boldsymbol{\phi})\boldsymbol{\Gamma}$ instead of $\mathbf{A}(\boldsymbol{\theta}, \boldsymbol{\phi})$, the process of scanning angles and identifying the noise subspace orthogonal vector does not yield the desired LOS angle. Instead, it produces a linear combination of all multipath angles.

Furthermore, with all these multipath parameters unknown, it is impossible to recover the LOS angle from the result. Thus, the subspace algorithms fail.

4.3.1. Spatial Smoothing for Coherent Signals

The failure of subspace-based AoA estimate algorithms in a coherent scenario can be attributed to the need for decorrelating the signals and restoring the rank of the covariance matrix in order to effectively

mitigate multipath interference for subspace approaches. Typically, spatial smoothing is employed for this purpose. According to Tuncer, it is generally observed that other approaches such as the Forward-Backward Approach and Toeplitz Completion exhibit comparatively lower performance than FBSS [28].

T.J. Shan introduced the idea of averaging the covariance matrices of different subarrays for decorrelation [36] [37] . Nevertheless, the implementation of forward-only smoothing requires a significant amount of antennae. An advanced method called Forward-backward Spatial Smoothing (FBSS) is brought up [38]. In general, the spatial smoothing technique necessitates pre-processing through the partitioning of the antenna array into overlapping subarrays. Yi employed the FBSS method to the URA scenario and proved its validity [39].

Consider a URA with a size of $M \times N$. This URA can be divided into overlapping rectangular subarrays, each with a size of $M_s \times N_s$. In each direction, there will be $L_M = M - M_s + 1$ and $L_N = N - N_s + 1$ subarrays respectively. Consequently, the total number of subarrays will be $L_M \times L_N$. The reference subarray is defined as the first $M_s \times N_s$ square antenna array starting at the upper-left corner. Ihe data in the vector of each subarrayis stacked along the x-direction. For example, the first subarray on both axes, i.e., the (1,1)-th subarray, has the $M_s N_s \times 1$ data vector:

$$\mathbf{x}_{1,1}(t) = [x_{1,1}(t), x_{2,1}(t), \cdots, x_{M_s,1}(t), x_{1,2}(t), \cdots, x_{M_s,N_s}(t)]^T \tag{4.41}$$

where the subscript (1,1) on the vector on the left side indicates the first subarray on the x-direction and on the y-direction, while the subscript (m,n) on the right side indicates the position of each antenna within this particular subarray. Fig.4.2 shows an example of a 3×3 subarray, i.e., $M_s = N_s = 3$, and the antennas within it.

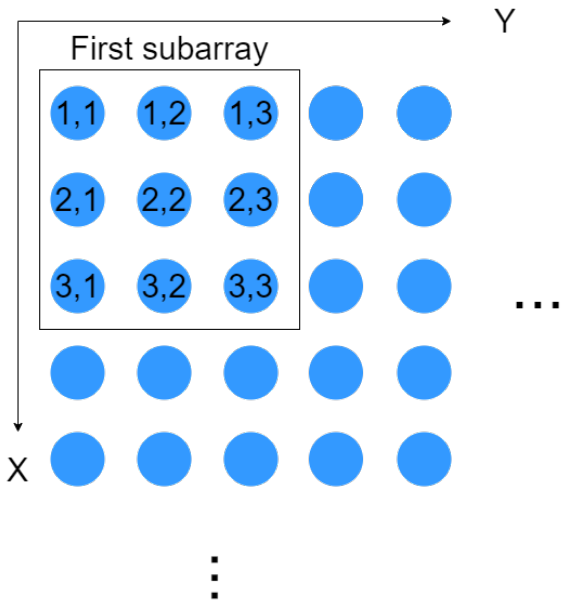

Figure 4.2: Illustration of a 3×3 Subarray.

Let the $M_s N_s \times k$ matrix $\mathbf{A}_1$ denote the steering matrix of the first subarray. Then the (m,n)-th subarray is expressed as

$$\mathbf{x}_{m,n}(t) = \mathbf{A}_1 \mathbf{D}_x^{m-1} \mathbf{D}_y^{n-1} \mathbf{s}(t) + \mathbf{n}_{m,n}(t) \tag{4.42}$$

where $\mathbf{n}_{m,n}(t)$ is the Gaussian noise vector of this subarray, $\mathbf{D}_x$ and $\mathbf{D}_y$ are the $K \times K$ diagonal matrix of phase-shift for each multipath signal that is explicitly expressed as

$$\mathbf{D}_Y = \text{diag}\left[\gamma_1, \gamma_2, \cdots, \gamma_k\right]; \gamma_i = \exp(j2\pi d_y \sin\phi_i \sin\theta_i / \lambda) \tag{4.43}$$

and

$$\mathbf{D}_X = \text{diag}\left[\beta_1, \beta_2, \cdots, \beta_k\right]; \gamma_i = \exp(j2\pi d_x \cos\phi_i \sin\theta_i / \lambda) \tag{4.44}$$

The covariance matrix of the (m,n)-th subarray is then given by

$$\mathbf{R}_{m,n} = \mathbf{A}_1 \mathbf{D}_x^{m-1} \mathbf{D}_y^{n-1} \mathbf{R}_s (\mathbf{D}_y^{n-1})^H (\mathbf{D}_x^{m-1})^H \mathbf{A}_1^H + \sigma^2 \mathbf{I} \tag{4.45}$$

By adding all these covariance matrices of subarrays together and averaging them, we have the forward-smoothed covariance matrix $\mathbf{R}^f$:

$$\begin{aligned} \mathbf{R}^f &= \frac{1}{M_0 N_0} \sum_{m=1}^{M_0} \sum_{n=1}^{N_0} \mathbf{R}_{m,n} \\ &= \mathbf{A}_1 \mathbf{R}_s \mathbf{A}_1^H + \sigma^2 \mathbf{I} \end{aligned} \tag{4.46}$$

where $\mathbf{R}_s$ is the smoothed signal covariance matrix.

The rank of $\mathbf{R}_s$ is recovered by constructing the Vandermonde matrix structure. Expand $\mathbf{R}_s$:

$$\mathbf{R}_s = \frac{1}{M_0 N_0} \mathbf{G} \mathbf{G}^H \tag{4.47}$$

Exploit the structure of the $\mathbf{G}$ matrix:

$$\mathbf{G} = \begin{bmatrix} \mathbf{G}_x & \mathbf{D}_y \mathbf{G}_x & \mathbf{D}_y^2 \mathbf{G}_x & \cdots & \mathbf{D}_y^{N_0} \mathbf{G}_x \end{bmatrix} \tag{4.48}$$

where

$$\begin{aligned} \mathbf{G}_x &= \begin{bmatrix} \mathbf{\Gamma} & \mathbf{D}_x \mathbf{\Gamma} & \mathbf{D}_x^2 \mathbf{\Gamma} & \cdots & \mathbf{D}_x^{M_0} \mathbf{\Gamma} \end{bmatrix} \\ &= \begin{bmatrix} \alpha_1 & \alpha_1\beta_1 & \cdots & \alpha_1\beta_1^{M_0} \\ \alpha_2 & \alpha_2\beta_2 & \cdots & \alpha_2\beta_2^{M_0} \\ & & \cdots & \\ \alpha_K & \alpha_K\beta_K & \cdots & \alpha_K\beta_K^{M_0} \end{bmatrix} \\ &= \text{diag}(\alpha_1, \alpha_2, \cdots, \alpha_K) \begin{bmatrix} 1 & \beta_1 & \beta_1^2 & \cdots & \beta_1^{M_0} \\ 1 & \beta_2 & \beta_2^2 & \cdots & \beta_2^{M_0} \\ & & \vdots & & \\ 1 & \beta_K & \beta_K^2 & \cdots & \beta_K^{M_0} \end{bmatrix} \end{aligned} \tag{4.49}$$

It shows the Vandermonde structure of matrix $\mathbf{G}_x$.

For indoor scenarios, it is assumed that each multipath exhibits distinct attenuation and time delay, i.e. $\alpha_i \neq \alpha_j$ when $i \neq j$. As a result, the diagonal matrix of the multipath parameters is full rank. Then the rank of $\mathbf{G}_x$ is the same as the later part. Multipath signals are expected to arrive at each antenna with different angles. Then in the most extreme case where $\gamma_1 = \gamma_2 = \cdots = \gamma_K$, $\text{rank}(\mathbf{R}_s) = \text{rank}(\mathbf{G}) = \text{rank}(\mathbf{G}_x) = \min(K, M_0)$. This implies that there are no smoothing effects in the y-direction. After interchanging the order of $\mathbf{D}_x$ and $\mathbf{D}_y$, the same process can be applied. And with the extreme case of $\beta_1 = \beta_2 = \cdots = \beta_K$, we have $\text{rank}(\mathbf{R}_s) = \text{rank}(\mathbf{G}) = \text{rank}\mathbf{G}_y) = \min(K, N_0)$, where $\mathbf{G}_y = \begin{bmatrix} \mathbf{\Gamma} & \mathbf{D}_y \mathbf{\Gamma} & \mathbf{D}_y^2 \mathbf{\Gamma} & \cdots & \mathbf{D}_y^{N_0} \mathbf{\Gamma} \end{bmatrix}$.

Therefore, in order to completely eliminate the correlation between K coherent multipath signals in both the x and y directions, it is necessary to apply a minimum of K smoothing operations in each direction. This can be expressed as $M_0 \geq K$ and $N_0 \geq K$.

The backward spatial smoothing method is defined in a similar manner, but with a reversal of the data collecting sequence in both the x and y dimensions. The initial subarray located at the rear of a 5×5 antenna array is seen in Figure 4.3.

The 2-D FBSS covariance matrix $\mathbf{R}^{fb}$ is defined as

$$\begin{aligned} \mathbf{R}^{fb} &= \frac{1}{2} \left[\mathbf{R}^f + \mathbf{J} (\mathbf{R}^f)^* \mathbf{J} \right] \\ &= \mathbf{A}_1 \mathbf{R}_s^{fb} \mathbf{A}_1^H + \sigma^2 \mathbf{I} \end{aligned} \tag{4.50}$$

where $*$ represents complex conjugate operation, $\mathbf{J}$ is an exchange matrix with ones on its antidiagonal and zero elsewhere, $\mathbf{R}_s^{fb}$ refers to the forward/backward version of signal covariance.

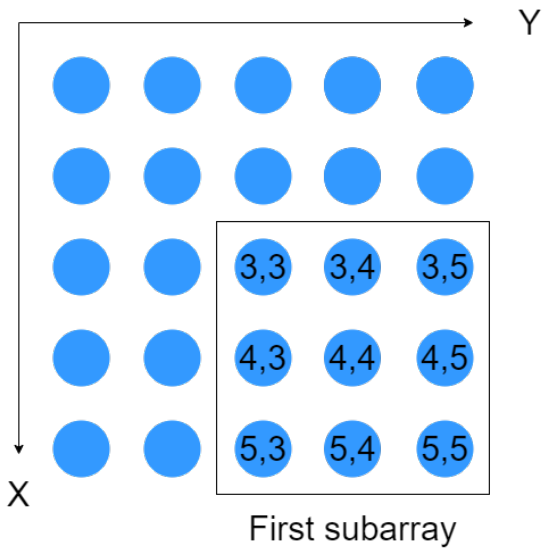

Figure 4.3: Illustration of the First Backward Subarray in a 5×5 Array.

As proved in [40], 2-D backward smoothing requires the geometry of the antenna array to satisfy some conditions. In order to successfully implement backward smoothing, every subarray and the entire array should be center symmetric. The subarray size must satisfy the condition $M_s \geq (k+1)$ and $N_s \geq (k+1)$ in order to ensure the extended linear independence property of the source phase vectors [41]. In summary, in order to achieve complete decorrelation of K coherent multipath signals, it is necessary for the full rectangular array to have a minimum size of $2K \times 2K$.

Based on the aforementioned explanation, it is apparent that the presence of additional antennas leads to an increase in the capacity to decorrelate a greater number of multipath signals. Nevertheless, the upper limit for the number of antennae is also constrained by the length of the CTE. CTE has a maximum length of 160µs and a minimum sample and switch period of 1µs per slot. It is capable of accommodating 74 samples, which is sufficient to include a single snapshot of samples from either a 8×8 URA or a rim URA with 18 antennas on each edge.

4.4. Toeplitz Matrix Reconstruction

In addition to the Spatial Smoothing technique, another strategy for reducing the effects of multipath signals is to restore the rank of the covariance matrix by generating a Toeplitz structured matrix and then using an ESPRIT-like method for angle estimation.

The Toeplitz structure denotes a matrix is diagonal constant matrix with its descending diagonal elements from left to right (or anti-diagonal) constant [42]. As an example:

$$\mathbf{T} = \begin{bmatrix} t_1 & t_2 & t_3 \\ t_4 & t_1 & t_2 \\ t_5 & t_4 & t_1 \\ t_6 & t_5 & t_4 \end{bmatrix} \tag{4.51}$$

is a Toeplitz matrix. Each of the diagonal elements t_i is not necessarily the same as t_j when $i \neq j$. Toeplitz reconstruction methods rearrange the elements or vectors in the covariance matrix into a Toeplitz structure so the rank of the result matrix is not relevant with the signal coherence anymore.

4.4.1. Toeplitz Matrix Construction

Han first proposed an ESPRIT-like algorithm for coherent DoA estimation in 1-D scenario [43]. In [44], such a method is generalized to 2-D DoA estimation. Using the data model in 4.2, the correlation

between the (m,n)-th antenna and the (p,q)-th antenna, detoted as $r(m,n;p,q)$, is

$$\begin{aligned} r(m,n;p,q) &= \mathsf{E}(s_0(t)s_0^*(t)) \sum_{k_1=1}^{K}\sum_{k_2=1}^{K} \alpha_{k_1}\alpha_{k_2}^*\beta_{k_1}^m\gamma_{k_1}^n\beta_{k_2}^{-p}\gamma_{k_2}^{-q} + \sigma_n^2\delta_{mp}\delta_{nq} \\ &= \sum_{k_2=1}^{K} d_{k2,m,n}\beta_{k_2}^{-p}\gamma_{k_2}^{-q} + \sigma_n^2\delta_{mp}\delta_{nq} \end{aligned} \tag{4.52}$$

where E indicates the expectation operation, $\delta_{ij} = \delta(i-j)$, and $d_{k2,m,n} = \mathsf{E}(s(t)s^*(t)\sum_{k_1=1}^{K}\alpha_{k_1}\beta_{k_1}^m\gamma_{k_1}^n$. Redefine the K_2-th signal as the k-th signal so $d_{k2,m,n} = d_{k,m,n}$, (4.52) becomes:

$$\begin{aligned} \mathbf{R}(m,n;p) &= \begin{bmatrix} r(m,n;p,0) & r(m,n;p,1) & & r(m,n;p,N-Q) \\ r(m,n;p,1) & \ddots & & \vdots \\ \vdots & & \ddots & \\ r(m,n;p,Q-1) & \cdots & & r(m,n;p,N-1) \end{bmatrix} \\ &= \mathbf{A}\sum_p D(m,n)\bar{\mathbf{A}}^T + \sigma_n^2\delta_{mp}\mathbf{N}_n \end{aligned} \tag{4.53}$$

where $\sum_p = \mathsf{diag}(\beta_1^{-p},\cdots,\beta_K^{-p})$, $\mathbf{D}(m,n) = \mathsf{diag}[d_{1,m,n},\cdots,d_{K,m,n}]$, $\mathbf{A} = \begin{bmatrix}\mathbf{a}_1 & \cdots & \mathbf{a}_K\end{bmatrix} \in \mathbb{C}^{Q\times K}$ with $\mathbf{a}_i = \begin{bmatrix}1 & \gamma_i^{-1} & \cdots & \gamma_i^{-(Q-1)T}\end{bmatrix}$, $\bar{\mathbf{A}} = \begin{bmatrix}\bar{\mathbf{a}}_1 & \cdots & \bar{\mathbf{a}}_K\end{bmatrix} \in \mathbb{C}^{(N-Q+1)\times K}$ with $\bar{\mathbf{a}}_i = \begin{bmatrix}1 & \gamma_i^{-1} & \cdots & \gamma_i^{-(N-Q)T}\end{bmatrix}$, and $N_n \in \mathbb{C}^{Q\times(N-Q+1)}$. The structure of $\mathbf{N}_n$ is introduced in [44].

Next, construct a block Hankel matrix $\mathbf{R}(m,n)$ with $\mathbf{R}(m,n;p)$ from $p = 0,\cdots,M-1$:

$$\begin{aligned} \mathbf{R}(m,n) &= \begin{bmatrix} \mathbf{R}(m,n;0) & \mathbf{R}(m,n;1) & \cdots & \mathbf{R}(m,n;M-P) \\ \mathbf{R}(m,n;1) & \mathbf{R}(m,n;2) & \cdots & \mathbf{R}(m,n;M-P+1) \\ \vdots & \vdots & \ddots & \vdots \\ \mathbf{R}(m,n;P-1) & \mathbf{R}(m,n;P) & \cdots & \mathbf{R}(m,n;M-1) \end{bmatrix} \\ &= \mathbf{B}\mathbf{D}(m,n)\bar{\mathbf{B}}^T + \sigma_n^2\mathbf{N}_m\otimes\mathbf{N}_n \end{aligned} \tag{4.54}$$

where $\mathbf{B} = \begin{bmatrix}\mathbf{b}_1 & \cdots & \mathbf{b}_K\end{bmatrix}$ with $\mathbf{b}_i = \begin{bmatrix}1 & \beta_i^{-1} & \cdots & \beta_i^{-(P-1)}\end{bmatrix}^T \otimes \begin{bmatrix}1 & \gamma_i^{-1} & \cdots & \gamma_i^{-(Q-1)}\end{bmatrix}^T \in \mathbb{C}^{PQ\times 1}$,
and $\bar{\mathbf{B}} = \begin{bmatrix}\bar{\mathbf{b}}_1 & \cdots & \bar{\mathbf{b}}_K\end{bmatrix}$ with $\bar{\mathbf{b}}_i = \begin{bmatrix}1 & \beta_i^{-1} & \cdots & \beta_i^{-(M-P)}\end{bmatrix}^T \otimes \begin{bmatrix}1 & \gamma_i^{-1} & \cdots & \gamma_i^{-(N-Q)}\end{bmatrix}^T \in \mathbb{C}^{(N-Q+1)(M-P+1)\times 1}$.

The limitation of such a Toeplitz construction approach is still the number of antennas. It was demonstrated in [45] that for such a matrix $\mathbf{R}(m,n)$ to restore the rank of the covariance matrix without requiring signal coherency, the P and Q values should be carefully set as suggested:

$$M-P+1 \geq P \geq K \quad N-Q+1 \geq Q \geq K \tag{4.55}$$

4.4.2. Toeplitz Angle Estimation

Although the constructed matrix in (4.54) appears to have a similar form of a regular covariance matrix, $\mathbf{N}_m \otimes \mathbf{N}_n$ is not always an identity matrix. Thus, instead of the MUSIC algorithm, we explore the shift-invariance property in the Hankel matrix $\mathbf{R}(m,n)$ and apply an ESPRIT-like algorithm for angle estimation.

Compute the singular value decomposition (SVD) of $\mathbf{R}(m,n)$ and extract $\mathbf{E_s}$ as the singular vectors corresponding to the K largest singular values. $\mathbf{E_s}$ and $\mathbf{B}$ thus should span the same signal subspace. Therefore, $\mathbf{E_s}$ and $\mathbf{B}$ can transfer into each other with an invertable transfer matrix T such that $\mathbf{E_s} = \mathbf{B}T$. Reminding that $\mathbf{R}(m,n)$ is a $(P-1)(Q-1)\times(M-P+1)(N-Q+1)$ matrix, the shift invariance property is explored by selecting the first and last $(P-1)Q$ rows of both $\mathbf{E_s}$ and $\mathbf{B}$ as $\mathbf{E}_{1\beta}$,$\mathbf{E}_{2\beta}$ and $\mathbf{B}_{1\beta}$,$\mathbf{B}_{2\beta}$. The relations between these four matrices are:

$$\begin{aligned} \mathbf{E}_{1\beta} &= \mathbf{B}_{1\beta}\mathbf{T} \\ \mathbf{E}_{2\beta} &= \mathbf{B}_{2\beta}\mathbf{T} \\ \mathbf{B}_{2\beta} &= \mathbf{B}_{1\beta}\mathbf{\Phi}_\beta \end{aligned} \tag{4.56}$$

where $\mathbf{\Phi}_\beta = \text{diag}(\beta_1, \cdots, \beta_K)$.

For estimating γ, first rearrange $\mathbf{B}$ into $\mathbf{B}_\gamma = \begin{bmatrix} \hat{\mathbf{b}}_1 & \cdots & \hat{\mathbf{b}}_K \end{bmatrix}$ with $\hat{\mathbf{b}}_i = \begin{bmatrix} 1 & \gamma_i^{-1} & \cdots & \gamma_i^{-(Q-1)} \end{bmatrix}^T \otimes \begin{bmatrix} 1 & \beta_i^{-1} & \cdots & \beta_i^{-(P-1)} \end{bmatrix}^T$. This transformation can be done by a permutation matrix $\mathbf{P}$ so that $\hat{\mathbf{b}}_i = \mathbf{P}\mathbf{b}_i$ and $\hat{\mathbf{E}_s} = \mathbf{P}\mathbf{E}_s$. Similarly, select the first and last $(Q-1)P$ rows of $\hat{\mathbf{B}}$ and $\hat{\mathbf{E}_s}$ as $\mathbf{E}_{1\gamma}$,$\mathbf{E}_{2\gamma}$ and $\mathbf{B}_{1\gamma}$,$\mathbf{B}_{2\gamma}$. The relationship between them:

$$\begin{aligned} \mathbf{E}_{1\gamma} &= \mathbf{B}_{1\gamma}\mathbf{T} \\ \mathbf{E}_{2\gamma} &= \mathbf{B}_{2\gamma}\mathbf{T} \\ \mathbf{B}_{2\gamma} &= \mathbf{B}_{1\gamma}\mathbf{\Phi}_\gamma \end{aligned} \tag{4.57}$$

where $\mathbf{\Phi}_\gamma = \text{diag}[\gamma_1, \cdots, \gamma_K]$. Combine (4.56) and (4.57) together, we have

$$\begin{aligned} \mathbf{T}^{-1}\mathbf{\Phi}_\beta\mathbf{T} &= \mathbf{E}_{1\beta}^\dagger\mathbf{E}_{2\beta} \\ \mathbf{T}^{-1}\mathbf{\Phi}_\gamma\mathbf{T} &= \mathbf{E}_{1\gamma}^\dagger\mathbf{E}_{2\gamma} \end{aligned} \tag{4.58}$$

where † means pseudo inverse.

4.4.3. Automatic Pairing in 2D-ESPRIT-like Algorithm

While it is possible to solve (4.58) using the basic ESPRIT method, a limitation arises due to the fact that both γ and β are not the actual target angles. Solving them individually may lead to the issue of pairing.

Chen introduced a pair-free approach for estimating frequency and subsequently employed it in the context of 2-D angle estimation [46][44]. The transfer matrix $\mathbf{T}$ is the link between γ and β. Compute eigenvalue decomposition (EVD) on $\mathbf{E}_{1\beta}^\dagger\mathbf{E}_{2\beta}$ then:

$$\mathbf{E}_{1\beta}^\dagger\mathbf{E}_{2\beta} = \mathbf{W}\mathbf{\Phi}_\beta\mathbf{W}^{-1} \tag{4.59}$$

When comparing equations (4.59) and (4.58), it can be observed that if all elements in $\mathbf{\Phi}_\beta$ are distinct, then both $\mathbf{T}^{-1}$ and $\mathbf{W}$ contain the linearly independent eigenvectors of $\mathbf{E}_{1\beta}^\dagger\mathbf{E}_{2\beta}$. Consequently, these matrices can be transformed into each other using a full-rank diagonal transfer matrix $\mathbf{G}$, such that $\mathbf{T}^{-1} = \mathbf{W}\mathbf{G}$. Then the $\mathbf{\Phi}_\gamma$ is computed as

$$\mathbf{\Phi}_\gamma = \mathbf{W}^{-1}\mathbf{E}_{1\gamma}^\dagger\mathbf{E}_{2\gamma}\mathbf{W} \tag{4.60}$$

Using the same $\mathbf{T}$ matrix,the results from $\mathbf{\Phi}_\beta$ and $\mathbf{\Phi}_\gamma$ are then automatically matched.

Finally, the two angles are computed from $\boldsymbol{\beta}$ and $\boldsymbol{\gamma}$ as

$$\begin{aligned} \theta_i &= \arctan\frac{\angle\gamma_i}{\angle\beta_i} \\ \phi_i &= \arccos\frac{1}{\pi}\sqrt{(\angle\gamma_i)^2 + (\angle\beta_i)^2} \end{aligned} \tag{4.61}$$

4.5. Proposed Virtual Antenna Extension

One limitation of spatial smoothing, particularly in this project, relates to the constrained number of antennas available. In order to differentiate all K sources, a minimum of K antennas is required for ULA. For forward-only 2-D smoothing, a $2K \times 2K$ antenna configuration is necessary, as stated by Chen et al. [41]. Similarly, for 2-D FBSS, a $3K/2 \times 3K/2$ antenna configuration is recommended, as mentioned by Yi et al. [39]. In order to ensure linear independence of the source vectors, it is necessary to impose a minimum constraint on the size of subarrays, denoted as $L_M \geq (K+1)$ and $L_N \geq (K+1)$ [41]. Such a constrain of sizes for both the subarray and the entire array has a detrimental impact on the performance of multipath mitigation with present hardware design.

Additionally, it should be noted that the 12-antenna array indicated before does not conform to the ideal URA configuration, as it lacks 4 antennas in the center of the array. The utilization of a structure referred to as a 'rim' or 'square' array introduces challenges in the process of identifying suitable subarrays.

As a result, the concept of a virtual array is proposed as a way to increase the equivalent quantity of antennas and enhance the efficacy of spatial smoothing.

Recall the basic data model of (4.39), the sampled covariance matrix is:

$$\hat{\mathbf{R}}_X = \mathbf{A}\boldsymbol{\Gamma}\hat{\mathbf{R}}_{S_0}\boldsymbol{\Gamma}^H\mathbf{A}^H + \sigma^2\mathbf{I} \tag{4.62}$$

After vectorizing, with the property $\text{vec}(\mathbf{ABC}) = (\mathbf{C}^T \otimes \mathbf{A})\text{vec}(\mathbf{B})$ and $(\mathbf{AB}) \otimes (\mathbf{CD}) = (\mathbf{A} \otimes \mathbf{C})(\mathbf{B} \otimes \mathbf{D})$, the equation becomes:

$$\begin{aligned}
\text{vec}(\hat{\mathbf{R}}_X) &= \text{vec}(\mathbf{A}\boldsymbol{\Gamma}\hat{\mathbf{R}}_{S_0}\boldsymbol{\Gamma}^H\mathbf{A}^H) + \text{vec}(\sigma^2\mathbf{I}) \\
&= \left[(\boldsymbol{\Gamma}^H\mathbf{A}^H)^T \otimes (\mathbf{A}\boldsymbol{\Gamma})\right] \text{vec}(\hat{R}_{S_0}) + \sigma^2\text{vec}(\mathbf{I}) \\
&= \left[(\mathbf{A}^*\boldsymbol{\Gamma}^*) \otimes (\mathbf{A}\boldsymbol{\Gamma})\right] \mathbf{p} + \sigma^2\text{vec}(\mathbf{I}) \\
&= (\mathbf{A}^* \otimes \mathbf{A})\,(\boldsymbol{\Gamma}^* \otimes \boldsymbol{\Gamma})\,\mathbf{p} + \sigma^2\mathbf{1}_e \\
&= (\mathbf{A}^* \otimes \mathbf{A})\,\mathbf{S}_v + \sigma^2\mathbf{1}_e
\end{aligned} \tag{4.63}$$

where p is a scalar representing the power of the input LOS signal, and $\mathbf{1}_e = \begin{bmatrix}\mathbf{e}_1^T & \mathbf{e}_2^T & \dots & \mathbf{e}_k^T\end{bmatrix}^T$ with i-th row $\mathbf{e}_i$ a vector has 1 at its i-th column and 0 anywhere else, $\otimes$ is the Kronecker product, and $\mathbf{S}_v = (\boldsymbol{\Gamma}^* \otimes \boldsymbol{\Gamma})\,\mathbf{p}$ is the virtual signal vector.

In (4.63), a new virtual data model is constructed, with a new manifold matrix $\mathbf{A}^* \otimes \mathbf{A}$. When K signals are not coherent, (4.62) then changes into:

$$\hat{\mathbf{R}}_\mathbf{X} = \mathbf{A}\hat{\mathbf{R}}_\mathbf{S}\mathbf{A}^H + \sigma^2\mathbf{I} \tag{4.64}$$

where the sample signal covariance matrix

$$\begin{aligned}
\hat{\mathbf{R}}_\mathbf{S} &= E(\mathbf{S}\mathbf{S}^H) \\
&= \text{diag}(p_1, p_2, \cdots, p_K)
\end{aligned} \tag{4.65}$$

is a $K \times K$ matrix with diagonal elements as the power of each signal and others as zero. Since $\hat{\mathbf{R}}_\mathbf{S}$ is a diagonal matrix, it can be simplified using another property of vec operator:

$$\text{vec}(\mathbf{ABC}) = (\mathbf{C}^T \circ \mathbf{A})\text{diag}(\mathbf{B}) \tag{4.66}$$

where $\circ$ stands for Khatri-Rao product and $\text{diag}(\mathbf{B})$ is the vector containing all the diagonal elements of the diagonal matrix $\mathbf{B}$. Then (4.63) becomes

$$\begin{aligned}
\text{vec}(\hat{\mathbf{R}}_\mathbf{X}) &= (\mathbf{A}^* \circ \mathbf{A})\,\text{diag}(\hat{\mathbf{R}}_\mathbf{S}) \\
&= \begin{bmatrix}\mathbf{a_1}^* \circ \mathbf{a_1} & \mathbf{a_2}^* \circ \mathbf{a_2} & \cdots & \mathbf{a_K}^* \circ \mathbf{a_K}\end{bmatrix} \text{diag}(\hat{\mathbf{R}}_\mathbf{S})
\end{aligned} \tag{4.67}$$

The Khatri-Rao product, or the column-wise Kronecker product, ensures that for each combination of

corresponding columns $\mathbf{a_i}^* \circ \mathbf{a_i}$, there is only angle interaction within the same source, written explicitly:

$$\mathbf{a_i}^* \circ \mathbf{a_i} = \begin{bmatrix} 1 \\ e^{-\beta_i} \\ e^{-2\beta_i} \\ \vdots \\ e^{-(M-1)\beta_i} \\ e^{-\gamma_i} \\ e^{-\beta_i\gamma_i} \\ \vdots \\ e^{-(M-1)\beta_i(N-1)\gamma_i} \end{bmatrix}^* \circ \begin{bmatrix} 1 \\ e^{-\beta_i} \\ e^{-2\beta_i} \\ \vdots \\ e^{-(M-1)\beta_i} \\ e^{-\gamma_i} \\ e^{-\beta_i+\gamma_i} \\ \vdots \\ e^{-(M-1)\beta_i(N-1)+\gamma_i} \end{bmatrix}$$

$$= \begin{bmatrix} 1 \\ e^{-\beta_i} \\ e^{-2\beta_i} \\ \vdots \\ e^{-(M-1)\beta_i} \\ e^{-\gamma_i} \\ e^{-\beta_i+\gamma_i} \\ \vdots \\ e^{-(M-1)\beta_i(N-1)\gamma_i} \\ e^{+\beta_i} \\ e^{+\beta_i}e^{-\beta_i} \\ e^{+\beta_i}e^{-2\beta_i} \\ \vdots \\ e^{+\beta_i}e^{-(M-1)\beta_i} \\ e^{+\beta_i}e^{-\gamma_i} \\ e^{+\beta_i}e^{-\beta_i+\gamma_i} \\ \vdots \\ e^{+\beta_i}e^{-(M-1)\beta_i(N-1)+\gamma_i} \\ \vdots \end{bmatrix} \in \mathbb{C}^{(MN)^2\times 1} \tag{4.68}$$

where β_i and γ_i are defined as in (4.43) and (4.44). Because the multiplication between natural exponents is the addition or subtraction of their index, the column-wise Kronecker product, unlike the conventional Kronecker product, constructs the antenna manifold by computing within each source itself. The result, still a vector of exponents with an index combining only β_i and γ_i and no angles from other sources, preserves the structure of the steering vector but extends the variety of positions.

However, in cases where the signals exhibit coherence, the property stated in (4.66) is not applicable, and the standard Kronecker product remains practical. The constructed manifold is then transformed into:

$$\mathbf{A}^* \otimes \mathbf{A} = \begin{bmatrix} \mathbf{a_1}^* \otimes \mathbf{A} & \mathbf{a_2}^* \otimes \mathbf{A} & \cdots & \mathbf{a_K}^* \otimes \mathbf{A} \end{bmatrix}$$

$$= \begin{bmatrix} a^*_{1,(1,1)}\mathbf{A} & a^*_{2,(1,1)}\mathbf{A} & \cdots & a^*_{K,(1,1)}\mathbf{A} \\ a^*_{1,(1,2))}\mathbf{A} & a^*_{2,(1,2)}\mathbf{A} & \cdots & a^*_{K,(1,2)}\mathbf{A} \\ & \cdots & \cdots & \\ a^*_{1,(M,N)}\mathbf{A} & a^*_{2,MN}\mathbf{A} & \cdots & a^*_{K,MN}\mathbf{A} \end{bmatrix} \in \mathbb{C}^{(MN)^2\times K^2} \tag{4.69}$$

where $\mathbf{a}_1 \in \mathbb{C}^{MN\times 1}$ is the i-th column of the steering matrix $\mathbf{A}$ indicating the steering vector of the i-th source, and $a_{i,(m,n))}$ is the steering element for the (m,n)-th antenna corresponding to the i-th source.

The problem of the virtual array extension arises in the $a^*_{i,(m,n)}\mathbf{A}$ as

$$
\begin{aligned}
a^*_{i,(m,n)}\mathbf{A} &= e^{(m-1)\beta_i+(n-1)\gamma_i}\mathbf{A} \\
&= e^{(m-1)\beta_i+(n-1)\gamma_i}\begin{bmatrix} 1 & 1 & \cdots & 1 \\ e^{-\beta_1} & e^{-\beta_2} & \cdots & e^{-\beta_K} \\ & \vdots & & \\ e^{-(m-1)\beta_1-(n-1)\gamma_1} & e^{-(m-1)\beta_2-(n-1)\gamma_2} & \cdots & e^{-(m-1)\beta_K-(n-1)\gamma_K} \end{bmatrix}
\end{aligned}
\tag{4.70}
$$

In equation (4.70), the preservation of the steering vector structure, as shown in equation (4.66), only occurs when the multiplication of $a^*_{i,(m,n)}$ with the i-th column in the steering matrix $\mathbf{A}$ takes place. The Kronecker product produces a cross-term in the j-th column, where $j \neq i$, which includes angles originating from various multipath sources.

When signals shows complete coherence, particularly in the context of multipath generated from a single point source, the Kronecker product of the multipath profile vector $\mathbf{\Gamma}^* \otimes \mathbf{\Gamma} \in \mathbb{C}^{K^2\times 1}$ increases the number of multipath from K to K^2. In order to achieve complete decorrelation of virtual multipath signals, a substantial increase in the number of virtual antennas is necessary.

In addition to the virtual array construction, which enables direct vectorization of the covariance matrix, there is also considerable discussion about a comparable extension method that utilizes fourth-order cumulant [47]. However, non-coherent signals still requires for cumulant methods.

On the other hand, if the signals are not coherent, the signal covariance matrix is diagonal. Then the VA model is able to actually extend the number of antennas by transforming the equivalent steering matrix $\mathbf{A}^* \odot \mathbf{A}$ as:

$$
\begin{aligned}
\mathbf{A}^* \odot \mathbf{A} &= \begin{bmatrix} \mathbf{a}^*(\phi_1,\theta_1) & \mathbf{a}^*(\phi_2,\theta_2) & \ldots & \mathbf{a}^*(\phi_k,\theta_k) \end{bmatrix} \odot \begin{bmatrix} \mathbf{a}(\phi_1,\theta_1) & \mathbf{a}(\phi_2,\theta_2) & \ldots & \mathbf{a}(\phi_k,\theta_k) \end{bmatrix} \\
&= \begin{bmatrix} 1 & 1 & \cdots & 1 \\ b_1(-x_1,-y_1) & b_2(-x_1,-y_1) & & b_k(-x_1,-y_1) \\ & \vdots & & \\ b_1(-x_{M-1},-y_{M-1}) & b_2(-x_{M-1},-y_{M-1}) & \ldots & b_k(-x_{M-1},-y_{M-1}) \end{bmatrix} \odot \\
&\quad \begin{bmatrix} 1 & 1 & \ldots & 1 \\ b_1(x_1,y_1) & b_2(x_1,y_1) & & b_k(x_1,y_1) \\ & \vdots & & \\ b_1(x_{M-1},y_{M-1}) & b_2(x_{M-1},y_{M-1}) & \ldots & b_k(x_{M-1},y_{M-1}) \end{bmatrix} \\
&= \begin{bmatrix} \mathbf{a}(\phi_1,\theta_1) & \mathbf{a}(\phi_2,\theta_2) & \ldots & \mathbf{a}(\phi_k,\theta_k) \\ b_1(-x_1,-y_1)\mathbf{a}(\phi_1,\theta_1) & b_2(-x_1,-y_1)\mathbf{a}(\phi_2,\theta_2) & & b_k(-x_1,-y_1)\mathbf{a}(\phi_k,\theta_k) \\ & \vdots & & \\ b_1(-x_{M-1},-y_{M-1})\mathbf{a}(\phi_1,\theta_1) & b_2(-x_{M-1},-y_{M-1})\mathbf{a}(\phi_2,\theta_2) & \ldots & b_k(-x_{M-1},-y_{M-1})\mathbf{a}(\phi_k,\theta_k) \end{bmatrix}
\end{aligned}
\tag{4.71}
$$

where $b_i(x_m,y_n) = e^{j\frac{2\pi(d_{x_m}\cos\phi_k\cos\theta_k + d_{y_n}\sin\phi_k\cos\theta_k)}{\lambda}}$ indicates the entry of the steering vector of the i-th source at the antenna with coordinates (x_m,y_n). It is easy to see that, multiplying the complex conjugate of steering elements with the original steering vector generates the steering element corresponding to a virtual position with the coordinates of the difference of their own ones.

Then, rows in vec $(\mathbf{R_X})$ that correspond to the same virtual position is removed and reordered according to their virtual coordinates. Fig.4.4 shows the placement for a 7×7 virtual array, with reference origin unmoved. Dots in red are the physical antennas and those in blue are the virtual antennas. After reordering,

As the constructed virtual array is a URA with size 7×7 and no 'holes' within, the FBSS technique can be directly applied. Fig.4.5 shows the 3×3 subarrays spreading in both the x and y directions.

The virtual covariance matrix after smoothing is a 9×9 one with full rank, which means the signals are uncorrelated. After smoothing, direction-finding methods like MUSIC and ESPRIT can be applied.

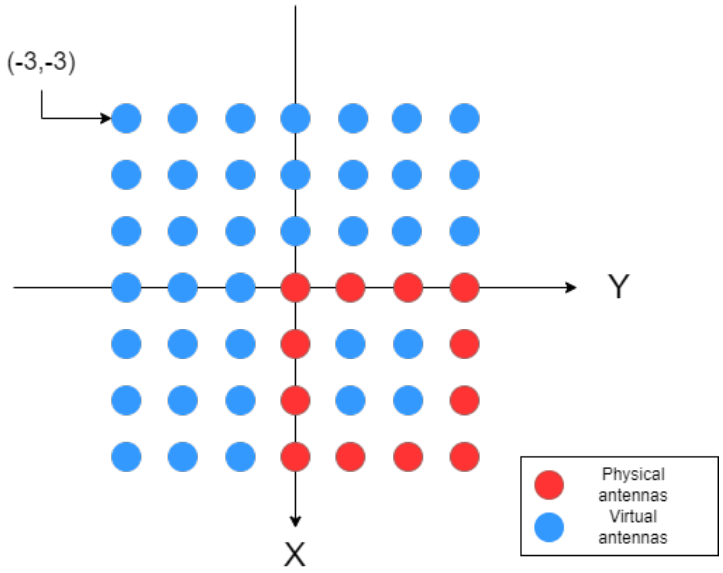

Figure 4.4: Illustration of Virtual Array.

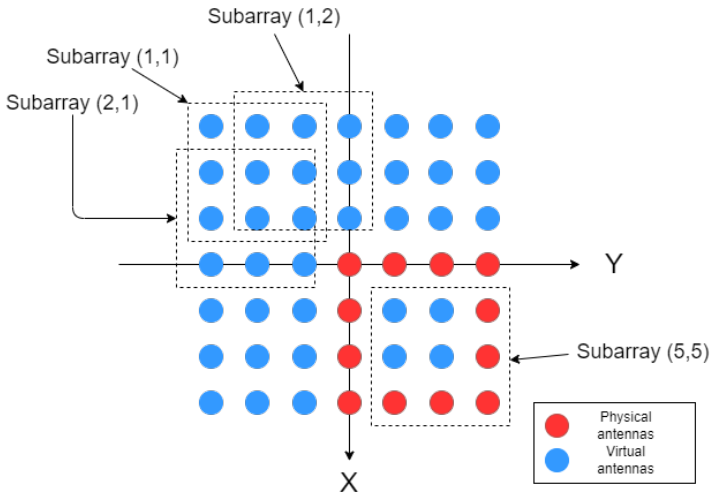

Figure 4.5: Illustration of 3×3 Virtual Subarrays.

4.6. Source Number Detection

As evidenced in previous sections, both MUSIC and ESPRIT, being subspace-based techniques, need the construction of a matrix dependent upon the number of sources. While the value of multipath is known in simulation, it is difficult to estimate in practical settings due to the presence of an unknown number of multipath.

Multiple indicators for source detection exist. The majority of these approaches are founded upon the idea that signals possess much greater energy levels in comparison to noise. Hence, an estimation of the quantity of signals can be derived by examining the count of the most prominent eigenvalues of the covariance matrix. The problem at hand is to the determination of an appropriate threshold for eigenvalues. Within this particular section, three distinct methods have been used for the simulation, namely the Akaike information criterion (AIC), Minimum Description Length (MDL), and SORTE.

4.6.1. AIC

AIC was first brought up in 1974 [48]. The indicator is a combination of two parts. The first one is a log-likelihood of the maximum likelihood estimates and the second one is a bias correction term, inserted to make the AIC an estimate of the mean Kulback-Liebler distance between the true distribution and

the estimated one. The AIC of the k-th eigenvalue is:

$$\mathrm{AIC}(k) = -2\log\left(\frac{\prod_{i=k+1}^{M}\ell_i}{\left(\frac{1}{M-k}\sum_{i=k+1}^{M}\ell_i\right)^{M-k}}\right)^{N} + 2k(2M-k). \tag{4.72}$$

where M is the number of antennas, N is the number of snapshots, and ℓ is the eigenvalue. After computing the AIC for all the eigenvalues, the number of sources $\hat{k}$ is determined as the k which corresponds to the minimum AIC, i.e.

$$\hat{k} = \mathrm{argmin}_k \mathrm{AIC}(k) \tag{4.73}$$

4.6.2. MDL

MDL, introduced by Rissanen in 1978 [49], is based on the idea of selecting the parameters that make the least code length of the encoded observation. The MDL of the k-th eigenvalue is:

$$\mathrm{MDL}(k) = -\log\left(\frac{\prod_{i=k+1}^{M}\ell_i}{\left(\frac{1}{M-k}\sum_{i=k+1}^{M}\ell_i\right)^{M-k}}\right) + \frac{1}{2}k(2M-k)\log N. \tag{4.74}$$

The same as AIC, the number of sources is the value that minimizes the MDL, i.e.

$$\hat{k} = \mathrm{argmin}_k \mathrm{MDL}(k) \tag{4.75}$$

4.6.3. SORTE

SORTE is another eigenvalue-based method[50]. The indicator is computing over all possible values for number of sources. The SORTE value with number k is defined as:

$$\mathrm{SORTE}(k) = \begin{cases} \frac{\mathrm{var}\left(\{\nabla\ell_i\}_{i=k+1}^{M-1}\right)}{\mathrm{var}\left(\{\nabla\ell_i\}_{i=k}^{M-1}\right)}, & \mathrm{var}\left(\{\nabla\ell_i\}_{i=k}^{M-1}\right) \neq 0 \\ +\infty & \mathrm{var}\left(\{\nabla\ell_i\}_{i=k}^{M-1}\right) = 0 \end{cases} \tag{4.76}$$

where $\nabla\ell = \ell_k - \ell_{k+1}$, and var stands for the variation computation which is defined as:

$$\mathrm{var}\left(\{\nabla\ell_i\}_{i=k}^{M-1}\right) = \frac{1}{M-k}\sum_{i=k}^{M-1}\left(\nabla\ell_i - \frac{1}{M-k}\sum_{j=k}^{M-1}\nabla\ell_j\right)^2 \tag{4.77}$$

Like the other two indicators, the number of sources gives the smallest value, i.e.

$$\hat{k} = \mathrm{argmin}_k \mathrm{SORTE}(k) \tag{4.78}$$

4.6.4. The Effect of Source Number Estimation

Although multiple ways of estimating the source number are available, the actual source number in the algorithm is always set to 2. Since both the simulation and experiment are conducted with a single source emitter and its attenuated delayed multipath, all the signals are correlated, while these indicators work under the assumption of uncorrelated sources. In [8], it is proved that with correlated sources, the best performance of the MUSIC algorithm does not always happen with the correct source number estimation.

In the following simulation, 1 LOS signal with 1 multipath scenario is constructed, and the test is conducted with 3 situations: the underestimated $(\hat{k} = 1)$, the correct estimation $(\hat{k} = 2)$, and the overestimated $(\hat{k} = 3)$. It is obvious that all three methods show nearly no difference in all scenarios.

4.7. Conclusion

In this section, we introduce the most commonly used and studied subspace methods, like MUSIC and ESPRIT. Both methods work well only with uncorrelated signals but would fail with coherent signals

such as multipath signals, which are unavoidable in indoor scenarios. Since the failure is due to the rank deficiency in the covariance matrix, several decorrelate algorithms, such as Spatial Smoothing and Toeplitz Construction are explained by restoring the rank of the covariance matrix.

However, in order to totally decorrelate all the multipath signals, both algorithms require that the number of antennas in two directions cannot be too small. For BLE data, the number of antennas and number of snapshots are all limited due to the limited maximum length of the CTE packet, which is only 160μs.

5

Positioning with Angle of Arrival

In previous chapters, just one receiver with 12 antennas and one set of angles (ϕ, θ) was involved. Because it simply provides a line of direction, this set of results is insufficient to locate the transmitter. To estimate the true position, multiple receivers and their associated angles are required. The positioning solution with measured AoA data will be formulated and discussed in this chapter. We will begin with a simple 2-D example and then move on to a 3-D scenario.

5.1. 2D Triangulation

The simplest case of triangulation is 2 receivers in a 2-D plane, as illustrated in Fig.5.1. The blue node

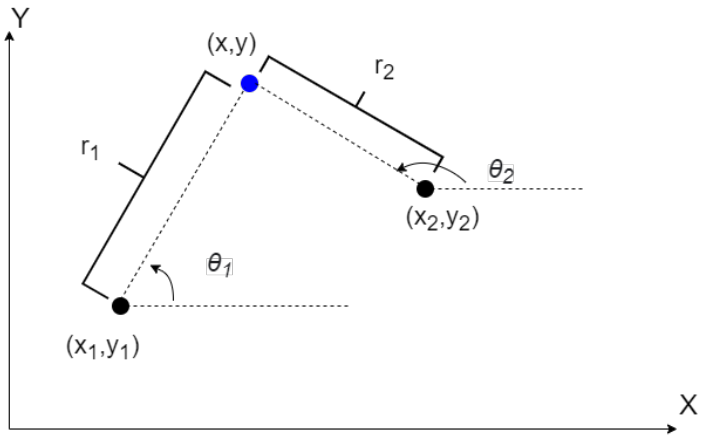

Figure 5.1: Illustration of 2-D Triangulation with Two Receivers.

represents the target transmitter, while the black nodes represent the known two receivers. θ_1 and θ_2 are the estimated azimuth angles of two receivers, respectively. The coordinates of the receivers are (x_1,y_1) and (x_2,y_2) in the global coordinate system. (x,y) is the transmitter's target position to be approximated using the same coordinate system. r_1 and r_2 are the distances between the transmitter and the associated receiver, respectively.

$$\begin{aligned} r_1 &= \sqrt{|x - x_1|^2 + |y - y_1|^2} \\ r_2 &= \sqrt{|x - x_2|^2 + |y - y_2|^2} \end{aligned} \tag{5.1}$$

The geometry problem can thus be formulated as

$$\begin{cases} r_1 \cos\theta_1 = x - x_1 \\ r_1 \sin\theta_1 = y - y_1 \end{cases} \tag{5.2}$$

for node (x_1,y_1) and

$$\begin{cases} r_2 \cos\theta_2 = x - x_2 \\ r_2 \sin\theta_2 = y - y_2 \end{cases} \tag{5.3}$$

for node (x_2,y_2).

Then, with n receivers, a similar relationship between arbitrary two receivers is established. For example, with receivers sorted as 1,2,3,$\cdots$,n, if only the relationship between two receivers of adjacent order is retrieved, the overestimated equations are obtained.

$$\mathbf{\Delta} \begin{bmatrix} r_1 \\ r_2 \\ \vdots \\ r_n \end{bmatrix} = \begin{bmatrix} -x_1 + x_2 \\ -y_1 + y_2 \\ -x_2 + x_3 \\ -y_2 + y_3 \\ \vdots \\ -x_{n-1} + x_n \\ -y_{n-1} + y_n \end{bmatrix} \tag{5.4}$$

where $\mathbf{\Delta} = \text{blkdiag}(\mathbf{\Delta}_1, \mathbf{\Delta}_2, \cdots, \mathbf{\Delta}_{n-1})$ and

$$\mathbf{\Delta}_i = \begin{bmatrix} \cos\theta_i & -\cos\theta_{i+1} \\ \sin\theta_i & -\sin\theta_{i+1} \end{bmatrix}$$

Compress (5.4) into matrix form, it would be

$$\mathbf{\Delta}[r_1, r_2, \cdots, r_n]^T = \mathbf{b} \tag{5.5}$$

where **b** is the vector on the right side. (5.5) can be solved as a least square problem, given the result

$$[\hat{r_1}, \hat{r_2}, \cdots, \hat{r_n}] = (\mathbf{\Delta}^T \mathbf{\Delta})^{-1} \mathbf{\Delta}^T \mathbf{b} \tag{5.6}$$

After estimating the distance, the position can be computed from any of the following equation

$$\begin{gathered} (\hat{x}, \hat{y}) = (x_1, y_1) + \hat{r_1}(\cos\theta_1, \sin\theta_1) \\ (\hat{x}, \hat{y}) = (x_2, y_2) + \hat{r_2}(\cos\theta_2, \sin\theta_2) \\ \vdots \\ (\hat{x}, \hat{y}) = (x_n, y_n) + \hat{r_n}(\cos\theta_n, \sin\theta_n) \end{gathered} \tag{5.7}$$

However, when the target coordinates (x,y) are inserted into the vector to be solved, equation (5.4) is modified into

$$\begin{bmatrix} \cos\theta_1 & 0 & 0 & \cdots & & -1 & 0 \\ \sin\theta_1 & 0 & 0 & & & 0 & -1 \\ 0 & \cos\theta_2 & 0 & & & -1 & 0 \\ 0 & \sin\theta_2 & 0 & & & 0 & -1 \\ \vdots & & & \ddots & & & \vdots \\ & \cdots & & & \cos\theta_n & -1 & 0 \\ & & & & \sin\theta_n & 0 & -1 \end{bmatrix} \begin{bmatrix} r_1 \\ r_2 \\ \vdots \\ r_n \\ x \\ y \end{bmatrix} = \begin{bmatrix} -x_1 \\ -y_1 \\ \vdots \\ -x_n \\ -y_n \end{bmatrix} \tag{5.8}$$

which can be compressed into matrix form as

$$\mathbf{M}[r_1, r_2, \cdots, r_n, x, y]^T = \mathbf{n} \tag{5.9}$$

where

$$\mathbf{M} = \begin{bmatrix} \cos\theta_1 & 0 & 0 & \cdots & & -1 & 0 \\ \sin\theta_1 & 0 & 0 & & & 0 & -1 \\ 0 & \cos\theta_2 & 0 & & & -1 & 0 \\ 0 & \sin\theta_2 & 0 & & & 0 & -1 \\ \vdots & & & \ddots & & & \vdots \\ & \cdots & & & \cos\theta_n & -1 & 0 \\ & & & & \sin\theta_n & 0 & -1 \end{bmatrix} \tag{5.10}$$

and

$$\mathbf{n} = \begin{bmatrix} -x_1 \\ -y_1 \\ \vdots \\ -x_n \\ -y_n \end{bmatrix} \tag{5.11}$$

which can be solved as a least square problem

$$[\hat{r_1}, \hat{r_2}, \cdots, \hat{r_n}, \hat{x}, \hat{y}]^T = (\mathbf{M}^T\mathbf{M})^{-1}\mathbf{M}^T\mathbf{n} \tag{5.12}$$

Nevertheless, only $\hat{x}$ and $\hat{y}$ are needed, thus the target position can be directly selected from the solution in (5.12) like

$$\begin{bmatrix} \hat{x} \\ \hat{y} \end{bmatrix} = \begin{bmatrix} 0 & \cdots & 0 & 1 & 0 \\ 0 & \cdots & 0 & 0 & 1 \end{bmatrix} (\mathbf{M}^T\mathbf{M})^{-1}\mathbf{M}^T\mathbf{n} \tag{5.13}$$

5.2. 3-D Triangulation

The geometric representation of the problem is depicted in Fig.5.2. It is important to highlight that the estimated angle values are calculated within the local coordinate system of each locator, whereby the reference antenna of each array functions as origin point of its local coordinate system.

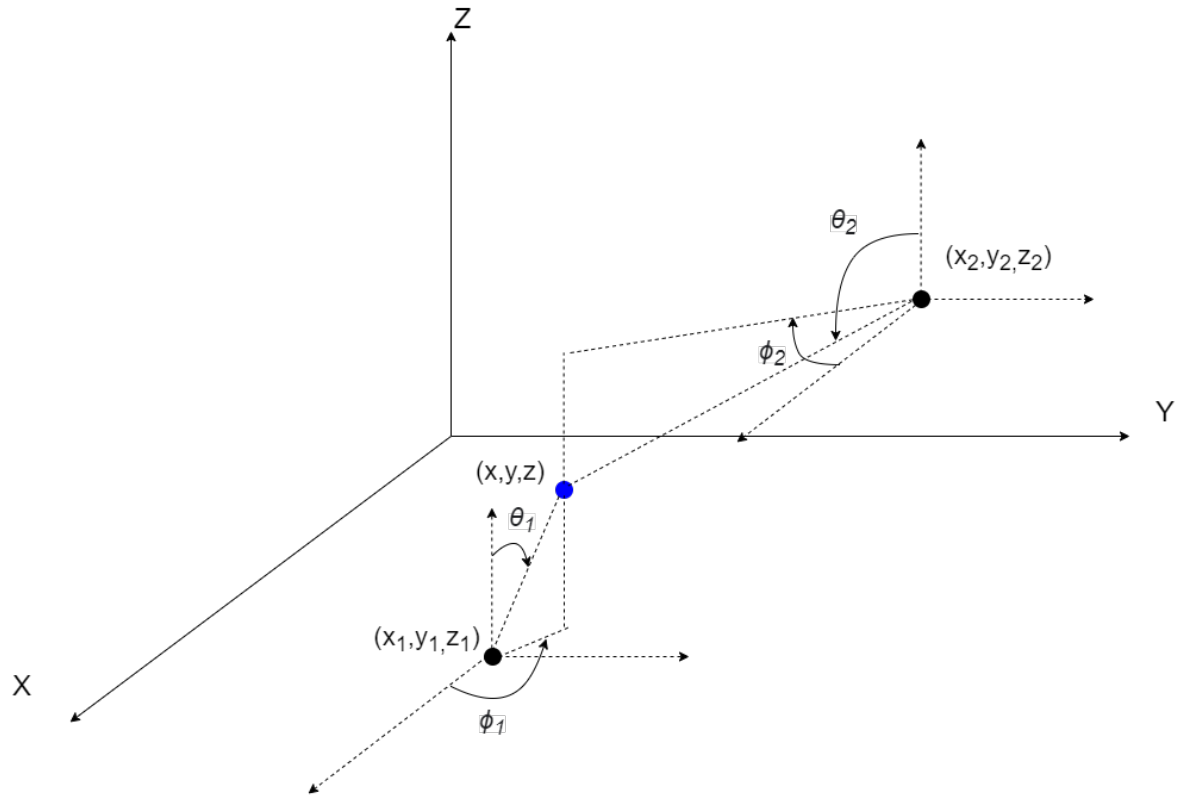

Figure 5.2: Illustration of 3-D Triangulation with Two Receivers.

5.2.1. Matlab Method

The blePositionEstimate function in Matlab has been developed to compute the position of the transmitter based on provided estimated results. Instead of simultaneously calculating all three coordinates, this function initially estimates the values of x and y. This is based on the observation that there exists a correlation between the i-th locator (x_i, y_i, z_i) and the position that needs to be approximated:

$$(x - x_i)\tan\phi_i = y - y_i \tag{5.14}$$

where ϕ_i is the estimated azimuth angle on the i-th locator. Stacking all M locators together and listing the $\begin{bmatrix} x & y \end{bmatrix}^T$ as the vector to be solved, we have

$$\begin{bmatrix} \tan\phi_1 & -1 \\ \tan\phi_2 & -1 \\ \vdots & \vdots \\ \tan\phi_M & -1 \end{bmatrix} \begin{bmatrix} x \\ y \end{bmatrix} = \begin{bmatrix} x_1 \tan\phi_1 - y_1 \\ x_2 \tan\phi_2 - y_2 \\ \vdots \\ x_M \tan\phi_M - y_M \end{bmatrix} \tag{5.15}$$

which, if compressed into matrix form, is:

$$\mathbf{A} \begin{bmatrix} x \\ y \end{bmatrix} = \mathbf{B} \tag{5.16}$$

Solve (5.16) in the least square way, giving

$$\begin{bmatrix} x \\ y \end{bmatrix} = (\mathbf{A}^T\mathbf{A})^{-1}\mathbf{A}^T\mathbf{B} \tag{5.17}$$

Then the z coordinate is calculated with estimated elevation angles. Note that here in Matlab algorithm, the elevation angle θ angle is defined differently as previously in thesis project. It is illustrated as in Fig.5.2. To begin, calculate the distance d on the x-y plane by computing the distance between the estimated coordinates $(\hat{x}, \hat{y})$ and the known coordinates of the locators (x,y):

$$d = \sqrt{\left(\begin{bmatrix} \hat{x} \\ \hat{x} \\ \vdots \\ \hat{x} \end{bmatrix} - \begin{bmatrix} x_1 \\ x_2 \\ \vdots \\ x_M \end{bmatrix} \right)^2 + \left(\begin{bmatrix} \hat{y} \\ \hat{y} \\ \vdots \\ \hat{y} \end{bmatrix} - \begin{bmatrix} y_1 \\ y_2 \\ \vdots \\ y_M \end{bmatrix} \right)^2} \tag{5.18}$$

With (5.18) and the geometry of z and elevation angle θ_i from the i-th locator :

$$z - z_i = d\tan\theta_i \tag{5.19}$$

So the $\hat{z}$ is calculated from (5.19) and (5.18) as

$$\hat{z} = \frac{(z_1 + d\tan\theta_1) + (z_2 + d\tan\theta_2) + \cdots + (z_M + d\tan\theta_{M_T})}{M_T} \tag{5.20}$$

The main problem with the Matlab approach described in (5.17) is that the matrix A solely consists of azimuth angles. Consequently, when two azimuth angles are sufficiently close, denoted as $\phi_1 \approx \phi_2$, the least squares solution becomes invalid. So the locators need to be carefully placed.

5.2.2. Proposed 3-D Least Square Positioning

One limitation of the Matlab method is its decomposition of the estimation of three coordinates into two separate steps, namely the estimation of the x-y coordinates and the estimation of the z coordinate. A novel approach is presented in this project, wherein a 3-D least squares method is introduced to simultaneously address the three unknown variables.

This method is still based on the geometry relationship between the (x, y, z) and the i-th locator (x_i, y_i, z_i):

$$\begin{cases} r_i\cos\theta_i\cos\phi_i = x - x_i \\ r_i\cos\theta_i\sin\phi_i = y - y_i \\ r_i\sin\theta_i = z - z_i \end{cases} \tag{5.21}$$

where $r_i = \sqrt{(x-x_i)^2 + (y-y_i)^2 + (z-z_i)^2}$ is the distance between the transmitter and the i-th loca-

tor.Extracting the distance $\mathbf{r} = [r_1, r_2, \cdots, r_{M_T}]^T$ as unknown, we have:

$$\mathbf{\Delta r} = \begin{bmatrix} x_1 - x_2 \\ y_1 - y_2 \\ z_1 - z_2 \\ x_2 - x_3 \\ y_2 - y_3 \\ z_2 - z_3 \\ \vdots \\ x_{M_T-1} - x_{M_T} \\ y_{M_T-1} - y_{M_T} \\ z_{M_T-1} - z_{M_T} \end{bmatrix} \tag{5.22}$$

where $\mathbf{\Delta}$ is a block diagonal matrix with $\mathbf{\Delta}_i, \in (1, 2, \cdots, M-1)$ but two adjacent diagonal matrices with the first column of the later matrix lying under the same column of the previous one's last column. And for each $\mathbf{\Delta}_i$, it is explicitly written as:

$$\mathbf{\Delta}_i = \begin{bmatrix} \cos\theta_i \cos\phi_i & -\cos\theta_{i+1} \cos\phi_{i+1} \\ -\cos\theta_i \sin\phi_i & \cos\theta_{i+1} \sin\phi_{i+1} \\ -\sin\theta_i & \sin\theta_{i+1} \end{bmatrix}$$

If the (x, y, z) is added into the unknown vector, then the relation estimated angles (ϕ_i, θ_i) and the unknown distance and coordinates (r_i, x_i, y_i, z_i) are as (5.21) whose matrix form is:

$$\begin{bmatrix} \cos\theta_i \cos\phi_i & -1 & 0 & 0 \\ \cos\theta_i \sin\phi_i & 0 & -1 & 0 \\ \sin\theta_i & 0 & 0 & -1 \end{bmatrix} \begin{bmatrix} r_i \\ x \\ y \\ z \end{bmatrix} = \begin{bmatrix} -x_i \\ -y_i \\ -z_i \end{bmatrix} \tag{5.23}$$

To simplify the notation, the left part of the first matrix in (5.23) is substituted by

$$\mathbf{M}_i = \begin{bmatrix} -\cos\theta_i \cos\phi_i & \cos\theta_i \sin\phi_i & \cos\theta_i \end{bmatrix}^T$$

and the coordinate-related vector for the i-th locator $\begin{bmatrix} -x_i & -y_i & -z_i \end{bmatrix}^T$ is represented as $\mathbf{b}_i$.

Expanding (5.23) for all m locators and stacking them together, the overall matrix form becomes:

$$\mathbf{A\ n = B} \tag{5.24}$$

where matrix $\mathbf{A} = \begin{bmatrix} \mathbf{M} & -\mathbf{1}_{m\times 1} \otimes \mathbf{I}_3 \end{bmatrix}$ is a matrix consists of the block-diagonal matrix $\mathbf{M} = \text{blkdig}()\mathbf{M}_1, \mathbf{M}_2, \cdots, \mathbf{M}_m)$ and the Kronecker product matrix $-\mathbf{1}_{m\times 1} \otimes \mathbf{I}_3$ where $\mathbf{1}_{m\times 1}$ is an all one vector of size $m \times 1$ and $\mathbf{I}_3$ represents an identity matrix of size 3×3, the unknown distance and coordinates vector $\mathbf{n} = \begin{bmatrix} r_1 & r_2 & \cdots & r_m & x & y & z \end{bmatrix}^T$, right matrix $\mathbf{B} = \begin{bmatrix} b_1 & b_2 & \cdots & b_m \end{bmatrix}^T$.

Solve (5.24) with the least square method, then the vector n becomes

$$\mathbf{n} = (\mathbf{A}^T\mathbf{A})^{-1}\mathbf{A}^T\mathbf{B} \tag{5.25}$$

Since only the position elements are the final results we need, the estimated positioning vector is $[\hat{x}, \hat{y}, \hat{z}]^T$ is selected as the last 3 rows of the estimated vector $\mathbf{n}$, denoted as $\mathbf{n}_3$

$$\mathbf{n}_3 = \begin{bmatrix} 0 & & 1 & 0 & 0 \\ 0 & \ddots & 0 & 1 & 0 \\ 0 & & 0 & 0 & 1 \end{bmatrix} \mathbf{n} \tag{5.26}$$

5.2.3. Total Least Square 3-D Positioning

Consider the equation presented in (5.24). The least square method only takes into account the error in $\mathbf{B}$, i.e.

$$\mathbf{Ax} = (\mathbf{B} + \mathbf{E}_B) \tag{5.27}$$

where $\mathbf{E}_B$ is the unknown error in $\mathbf{B}$, i.e. the error in assumed pre-known locations of locators. Compared to the least square method, the TLS method also considers the error in matrix $\mathbf{A}$, which was first proposed by [51]. In other words, the model changes into:

$$(\mathbf{A} + \mathbf{E}_A)x = (\mathbf{B} + \mathbf{E}_B) \tag{5.28}$$

where $\mathbf{E}_A$ is the error in matrix $\mathbf{A}$.

When considering BLE AoA positioning, it is more appropriate to utilize the TLS approach due to the fact that the primary source of triangulation error is from the $\mathbf{A}$ matrix, which encompasses the estimated angles (ϕ, θ). The TLS problem is expressed as:

$$\begin{aligned} &\min \|[\mathbf{E}_A, \mathbf{E}_B]\|_F^2 \\ &\text{suchthat } (\mathbf{A} + \mathbf{E}_A)\, n = \mathbf{B} + \mathbf{E}_B \end{aligned} \tag{5.29}$$

where $\|\cdot\|_F$ stands for the Frobenius norm.

In order to ensure a unique solution for the minimization problem in (5.29), it is necessary to find the smallest matrix $[\mathbf{E}_A, \mathbf{E}_B]$ that changes the rank of matrix $[\mathbf{A}, \mathbf{B}]$ from N+1 to N [52]. Since vector B does not lie in the subspace spanned by matrix A, all N+1 columns of the augmented matrix are linearly independent. The conventional way of addressing this issue is to eliminate the smallest singular value, which contains the least significant information.

The SVD of the combined matrix $[\mathbf{A}, \mathbf{B}]$ is shown as:

$$\begin{bmatrix} \mathbf{A} & \mathbf{B} \end{bmatrix} = \begin{bmatrix} \mathbf{U}_p & \mathbf{u}_q \end{bmatrix} \begin{bmatrix} \mathbf{\Sigma}_p & \\ & \sigma_q \end{bmatrix} \begin{bmatrix} \mathbf{V}_{pp} & \mathbf{v}_{pq} \\ \mathbf{v}_{qp} & v_{qq} \end{bmatrix}^\top \tag{5.30}$$

where $\mathbf{U}_p$ and $\mathbf{u}_q$ are respectively the first n and last single column of the left-eigenvector matrix $\mathbf{U}$, $\mathbf{\Sigma}_p$ and σ_q respectively first n and last eigenvalues with a descending order, $\mathbf{V}_{pp}$ is the $n \times n$ matrix within right-eigenvector matrix $\mathbf{V}$, $\mathbf{v}_{pq}$ and $\mathbf{v}_{qp}$ are respectively $n \times 1$ and $1 \times n$ vector, v_{qq} is a scalar in the partitioning.

As previously stated, after the approximation, matrix $[\mathbf{A} + \mathbf{E}_A, \mathbf{B} + \mathbf{E}_B]$ discards the smallest eigenvalue σ_q, so its SVD result is shown as:

$$\begin{bmatrix} \mathbf{A} + \mathbf{E}_A & \mathbf{B} + \mathbf{E}_B \end{bmatrix} = \begin{bmatrix} \mathbf{U}_p & \mathbf{u}_q \end{bmatrix} \begin{bmatrix} \mathbf{\Sigma}_p & \\ & 0 \end{bmatrix} \begin{bmatrix} \mathbf{V}_{pp} & \mathbf{v}_{pq} \\ \mathbf{v}_{qp} & v_{qq} \end{bmatrix}^\top \tag{5.31}$$

Comparing (5.30) and (5.31) and considering that the error part $[\mathbf{E}_A, \mathbf{E}_B]$ simply represents the difference between $[\mathbf{A} + \mathbf{E}_A, \mathbf{B} + \mathbf{E}_B]$ and $[\mathbf{A}, \mathbf{B}]$, the equality can be restated as

$$[\mathbf{A} + \mathbf{E}_A, \mathbf{B} + \mathbf{E}_B] = [\mathbf{A}, \mathbf{B}] + [\mathbf{E}_A, \mathbf{E}_B] \tag{5.32}$$

$$= [\mathbf{A}, \mathbf{B}] + \begin{bmatrix} \mathbf{U}_p & \mathbf{u}_q \end{bmatrix} \begin{bmatrix} \mathbf{0}_{n\times n} & \\ & \sigma_q \end{bmatrix} \begin{bmatrix} \mathbf{V}_{pp} & \mathbf{v}_{pq} \\ \mathbf{v}_{qp} & v_{qq} \end{bmatrix}^\top \tag{5.33}$$

$$= [A, B] + \begin{bmatrix} \mathbf{0}_{m\times n} & \sigma_q \end{bmatrix} \begin{bmatrix} \mathbf{V}_{pp} & \mathbf{v}_{pq} \\ \mathbf{v}_{qp} & v_{qq} \end{bmatrix}^\top \tag{5.34}$$

$$= [\mathbf{A}, \mathbf{B}] - \mathbf{u}_q \sigma_q \begin{bmatrix} \mathbf{v}_{pq} \\ v_{qq} \end{bmatrix}^\top \tag{5.35}$$

$$= [\mathbf{A},\ \mathbf{B}] - [\mathbf{A}, \mathbf{B}] \begin{bmatrix} \mathbf{v}_{pq} \\ v_{qq} \end{bmatrix} \begin{bmatrix} \boldsymbol{v}_{pq} \\ v_{qq} \end{bmatrix}^\top \tag{5.36}$$

Using the orthonormal property of matrix $\mathbf{V}$, i.e. $\mathbf{V}^T = \mathbf{V}^{-1}$, (5.36) can further delivered as:

$$[\mathbf{A} + \mathbf{E}_A, \mathbf{B} + \mathbf{E}_B] \begin{bmatrix} \mathbf{v}_{pq} \\ v_{qq} \end{bmatrix} = [\mathbf{A}, \mathbf{B}] \begin{bmatrix} \mathbf{v}_{pq} \\ v_{qq} \end{bmatrix} - [\mathbf{A}, \mathbf{B}] \begin{bmatrix} \mathbf{v}_{pq} \\ v_{qq} \end{bmatrix} \begin{bmatrix} \mathbf{v}_{pq} \\ v_{qq} \end{bmatrix}^\top \begin{bmatrix} \mathbf{v}_{pq} \\ v_{qq} \end{bmatrix} \tag{5.37}$$

$$[\mathbf{A} + \mathbf{E}_A, \mathbf{B} + \mathbf{E}_B] \begin{bmatrix} \mathbf{v}_{pq} \\ v_{qq} \end{bmatrix} = [\mathbf{A}, \mathbf{B}] \begin{bmatrix} \mathbf{v}_{pq} \\ v_{qq} \end{bmatrix} - [\mathbf{A}, \mathbf{B}] \begin{bmatrix} \mathbf{v}_{pq} \\ v_{qq} \end{bmatrix} \tag{5.38}$$

$$[\mathbf{A} + \mathbf{E}_A, \mathbf{B} + \mathbf{E}_B] \begin{bmatrix} \mathbf{v}_{pq} \\ v_{qq} \end{bmatrix} = \mathbf{0}_{m\times 1} \tag{5.39}$$

$$\tag{5.40}$$

It is clear that the parameter vector **n** or the solution of the TLS problem corresponds to

$$\mathbf{n}^*_{\text{TLS}} = -\mathbf{v}_{pq} v_{qq}^{-1} \tag{5.41}$$

And, because the TLS problem is tackled differently from the traditional LS problem, its performance typically cannot compete with the LS method.

6

Simulation

This chapter will present the outcomes of several AoA estimate and positioning algorithms, along with their performance, through simulations conducted on Matlab. Both the BLE signal and multipath profile are generated using the Matlab. The findings will be subjected to comparative analysis and subsequent discussion.

6.1. BLE Signal Generation

The Matlab simulation is built upon the official direction finding for tracking node position example in the Bluetooth Toolbox. The process of generating IQ samples is depicted in Fig.6.1 [53].

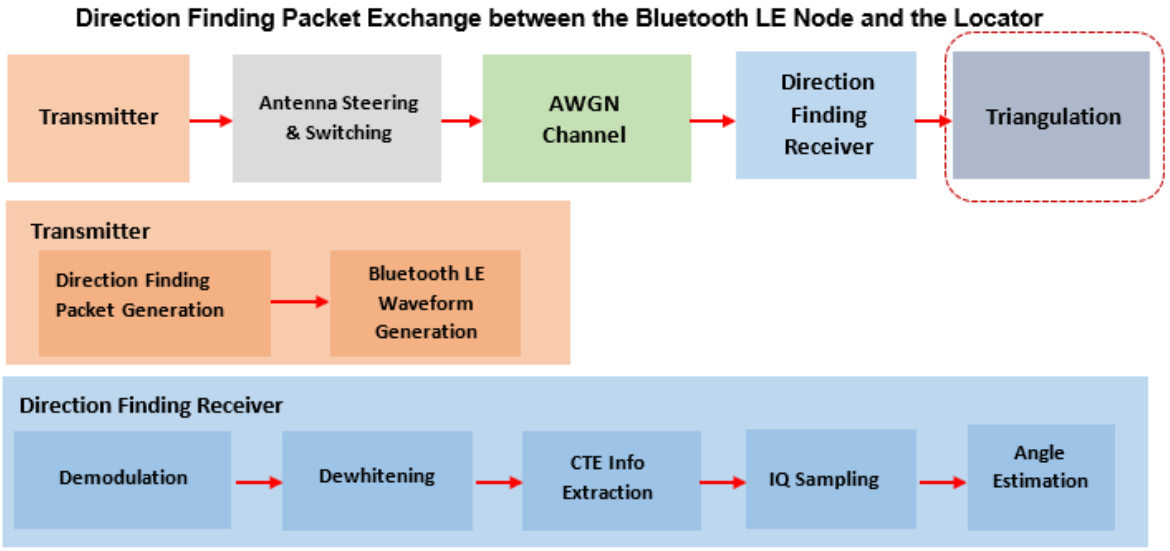

Figure 6.1: Illustration of MATLAB BLE Simulation Process.

The initial stage involves the generation of the BLE data bundle. The function *helperBLEGenerateDFPDU* is called with specified parameters, which include the packet type (either connection or connectionless CTE), the length of the CTE packet, the type of CTE packet, the length of the payload, and the starting CRC data. The packet comprises a Protocol Data Unit (PDU) that encompasses the information within the Cyclic Redundancy Check (CRC) section. The CRC is subsequently attached to the PDU.

Subsequently, the *bleWaveformGenerator* function will produce the BLE waveform by utilizing the preceding packet data. CTE bits consisting of all 1s are produced and appended following the preamble and the access address. The GMSK modulation technique is employed to modulate the entire frame of the physical layer.

Table 6.1: Parameters Used in Matlab Simulation

Parameter	Value	Meaning
M	4	Number of antennas along Z axis
N	4	Number of antennas along Y axis
λ	0.4	Antenna spacing
dfPacketType	'Connectless CTE'	Type of CTE Packets
switchingPattern	$[1, 2, \cdots, 16]$	The Robinhood switch pattern
slotDuration	1	Slot duration in microseconds
cteLength	160	Length of CTE in microseconds
crcInit	'555551'	CRC initialization
accessAddress	'01234567'	Access address
payloadLength	1	Payload length in bits

Subsequently, the BLE waveform is directed using specified azimuth and elevation angles and toggled based on the array geometry within the function *helperBLESteerSwitchAntenna*. The construction of the steering vector $\mathbf{a}(\phi, \theta)$, which corresponds to the angle pair (ϕ, θ) and is associated with a URA located on the x-z panel with an antenna spacing of λ, is as follows:

$$a(\phi, \theta) = \exp(-j2\pi \odot \mathbf{P} \odot \begin{bmatrix} \cos\theta\cos\phi \\ \cos\theta\sin\phi \\ \sin\theta \end{bmatrix}) \tag{6.1}$$

where $\odot$ stands for Hadamard product, and $\mathbf{P} \in \mathbb{R}^{3\times MN}$ is the antenna position matrix with M antennas on the z-direction and N antennas on the y-direction:

$$\mathbf{P} = \begin{bmatrix} 0 & 0 & & 0 & 0 & 0 & & 0 & & 0 \\ 0 & 0 & \cdots & 0 & \lambda & \lambda & \cdots & (N-1)\lambda & \cdots & (N-1)\lambda \\ 0 & \lambda & 2\lambda & (M-1)\lambda & 0 & \lambda & & 0 & & (M-1)\lambda \end{bmatrix} \tag{6.2}$$

As demonstrated in (6.2), the position matrix **P** can be modified with different antenna geometries. For multipath signals, the angles are computed with the ray-tracing technique. In the case of completely coherent signals, all signals originate from the same CTE packet, just with different attenuations and AoA. Thus, the multipath signals are generated by rotating the LOS angle.

Once the signal is rotated, the data is expanded from a single column originating from a reference antenna to $M \times N$ columns. The next step is to select data from various antennas resulting in the compression of the matrix into a singular column once more. As previously discussed in Chapter 2, the CTE samples are composed of reference samples obtained from the reference antenna, as well as other samples from antennas following the programmed switch pattern. It is noteworthy that switch slots do not include any useful data. So the samples ncluded within the switch slots are filled with zeros for further IQ sampling.

Then the steered and switched data is transmitted via an AWGN channel with given SNR values.

The final step is operating the IQ sampling at an ideal receiver with the function *bleIdealReceiver*. Since the waveform is corrupted by Gaussian noise, first the receiver needs to retrieve the CTE information from the noisy bits. The receiver would do IQ sampling based on the demodulated information. This can be achieved by retrieving the relevant data from the computed index. The IQ samples of different multipath signals are combined with the LOS signals by multiplying their amplitudes with their respective relative attenuations and adding them together.

All the parameters used in BLE signal generation are listed in Table.6.1.

6.1.1. Ray Tracing Technique

For multipath generation, it is crucial to accurately model the signal propagation from the transmitter and the receiver, particularly focusing on the path loss and the angle of arrival. In this project, we employed the ray-tracing technique. Matlab offers a selection of models, including atmospheric, empirical, terrain, and ray-tracing. After comparing them, the ray-tracing method is applied due to its ability to compute several propagation paths, including free space, reflection, and diffraction paths. Additionally, the maximum number of reflections can be adjusted in order to simplify the case.

In our simulation, the indoor environment is modeled as an empty room. The dimensions of the room are 10 meters in length, 6 meters in width, and 4 meters in height. Fig.6.2 shows the 3-D stl file of such a room, where the locator is positioned at (-1.2,-0.3,1.2) and the transmitter is located at (0,0,0.7). Matlab also provides more complex room models such as a conference room with a table, chairs, and laptops. Nevertheless, the presence of shelters in these models may result in the absence of LOS signal, hence causing the failure of the algorithm.

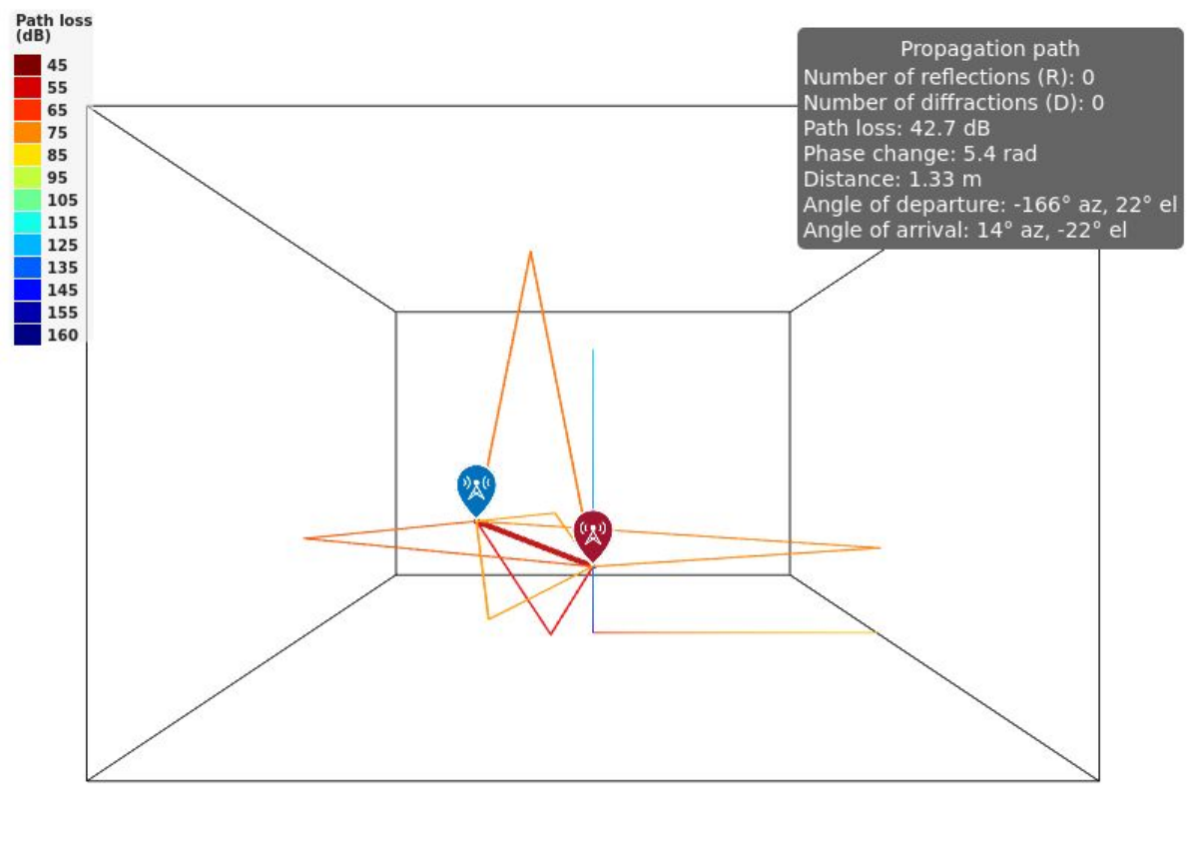

Figure 6.2: Illustration of Ray Tracing Model.

6.2. Frequency Offset Estimation Simulation

However, given the target of this project, the estimation of angles and positions holds greater importance. Therefore, the impact of frequency offset on angle estimation is the primary focus of our concern. Fig.6.3 demonstrates the impact of CFO techniques on the accuracy of AoA estimation. The simulation incorporates the same MUSIC estimate technique, without taking into account the effects of multipath propagation or packet aggregation.

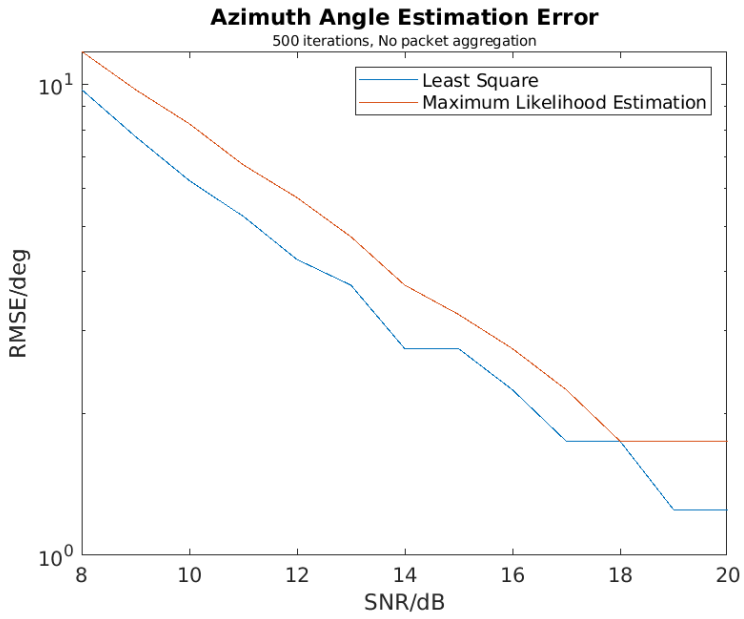

(a) RMSE of Azimuth Angle

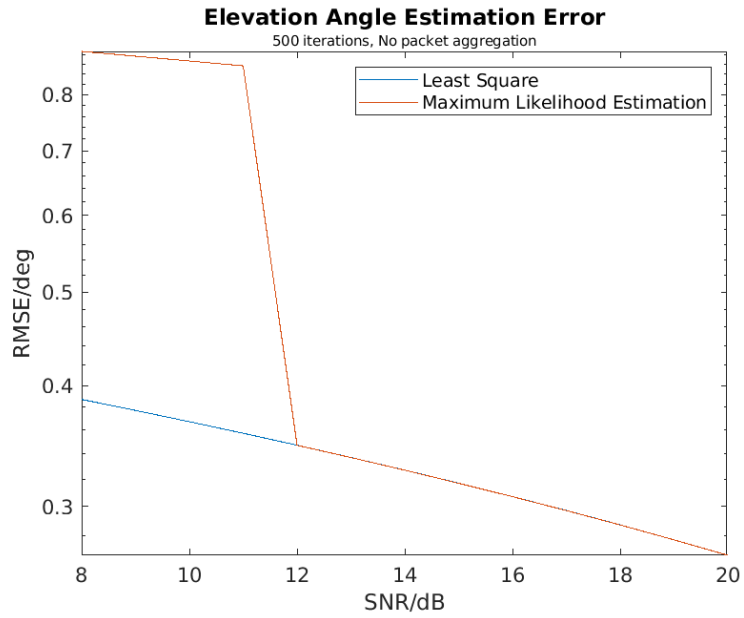

(b) RMSE of Elevation Angle

Figure 6.3: RMSE of Angles with Different CFO Estimation Methods Applied

The performance is evaluated with root-mean-square errors (RMSE) of angles. It is computed as

$$\text{RMSE} = \sqrt{\frac{\sum_{i=1}^{N}(x_i - \hat{x_i})^2}{N}} \tag{6.3}$$

where n is the total number of iterations for each SNR, $\hat{x_i}$ is the estimated angle, and x_i is the angle ground truth that is known in the simulations. Later when computing the RMSE for positions, $\hat{x_i}$ and x_i would represent the estimated and true positions respectively.

It is evident that the LS method exhibits a lower RMSE in comparison to the MLE method. As a result, the LS approach is selected as the ultimate algorithm for CFO estimate in further simulations. Nevertheless, the error level for both angles is rather low. The RMSE for the azimuth angle is found to be less than 5° when the SNR exceeds 12dB. The RMSE for the elevation angle consistently remains

Table 6.2: Parameters of Angle Estimation Simulation

Parameter	Value	Unit
Position of Locator	(-1.2,-0.3,1.2)	Meter
Position of Transmitter	(0,0,0.7)	Meter
Number of Multipath	7	
Channel Frequency	2.44	GHz
Number of Iterations	200	for each SNR

below 1°, and even below 0.5° specifically for the LS technique. The two fundamental CFO approaches provide satisfactory performance when the SNR exceeds 10dB. Consequently, in order to maintain the efficacy of the whole positioning algorithm, we did not explore more into complex CFO estimate techniques.

6.3. Angle Estimation Simulation

Two types of simulations are performed for the angle estimation. Given that the accuracy of AoA estimation is dependant upon the location of the transmitter as demonstrated in prior one-dimensional research, the first type of simulation fix the position for both the transmitter and the locator. In the other type of simulation, the transmitter will be positioned at various locations inside a two-dimensional plane, while keeping the single locator fixed. This will allow us to examine the influence of varied positions on angle accuracy.

To start with, only one locator is involved, and the position of the transmitter is fixed. The position configuration is shown in Tab.6.2. The graphic representation of the locator and the transmitter, as well as the LOS signal parameters obtained by the ray-tracing technique, is shown in Fig.6.2. The rays of both LOS and multipath are depicted, and their path loss is visualized with a color bar.

For each SNR value, the estimation process is repeated for N = 200 times. Even though more loops may result in a more smooth curve and help prevent extreme cases, we consider how fast the result should be computed in a real application, and thus 200 is chosen.

The RMSE simulation result is shown in Fig.6.4. It is evident that larger SNRs tend to yield more precise outcomes. When the SNR exceeds 20dB, the Toeplitz method exhibits the smallest error in azimuth angle, with an accuracy of less than 2°. The remaining three methods exhibit a somewhat higher error rate of less than 3°. For the elevation angle, Toeplitz method performed slightly worse than others, but still has error of less than 3°. The FBSS method and Unitary ESPRIT methods work better than Conventional MUSIC. In general, it can be shown from the box plots in Fig.6.5 and Fig.6.6 that as the SNR increases, the estimation results become more tightly clustered, indicating a decrease in variance. However, in the case of conventional music that lacks source decorrelation, there is not a significant variation in the variance of outcomes. The error range of elevation angle is smaller than the range of azimuth errors. With lower SNR, the azimuth error grows dramatically. In a higher SNR scenario (higher than 20dB), the VA+FBSS+MUSIC method has near zero variance.

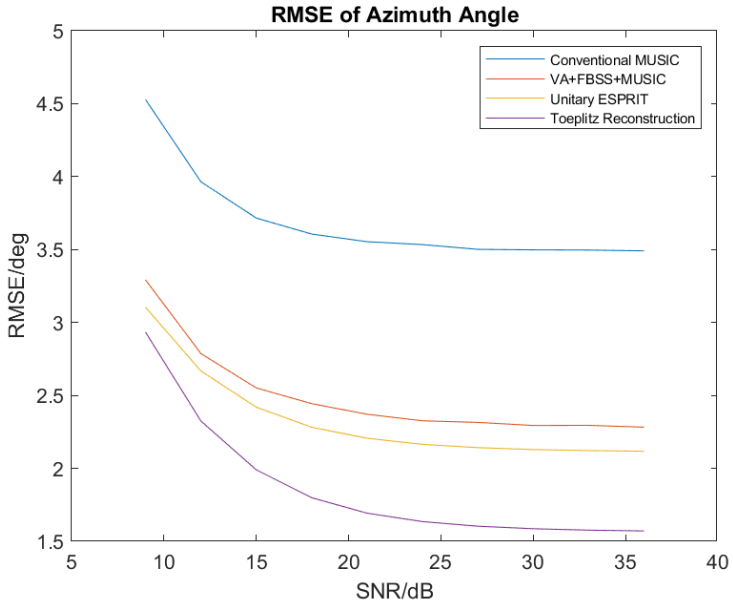

(a) RMSE of Azimuth Angle

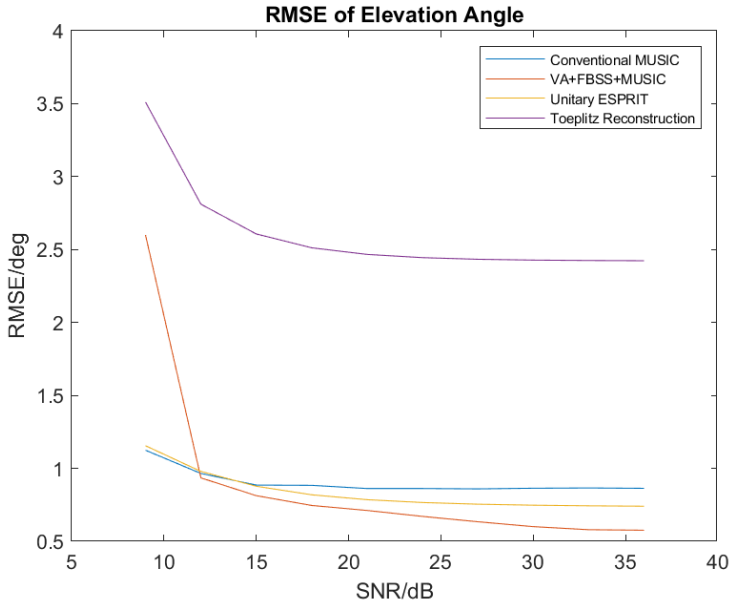

(b) RMSE of Elevation Angle

Figure 6.4: RMSE of All Methods with 4×4 URA

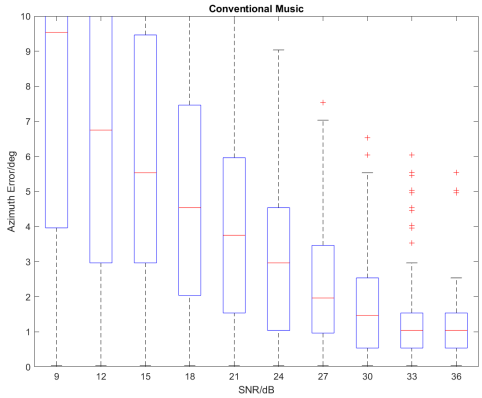

(a) CMUSIC Azimuth

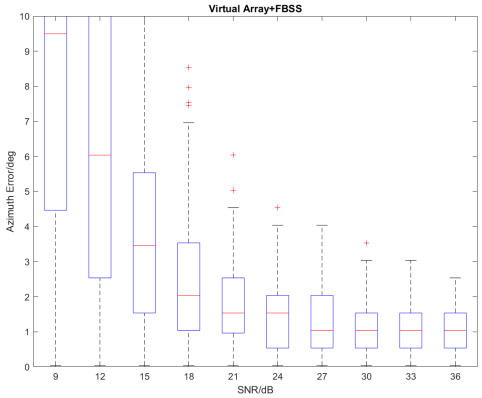

(b) VA+FBSS Azimuth

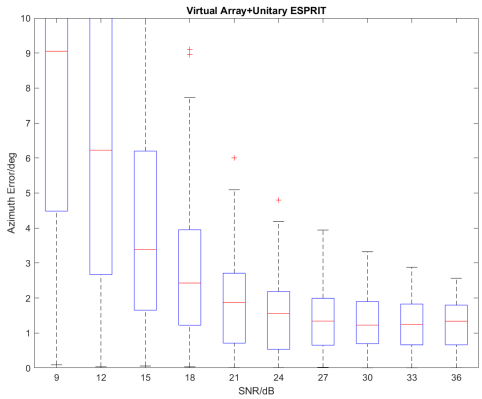

(c) Unitary ESPRIT Azimuth

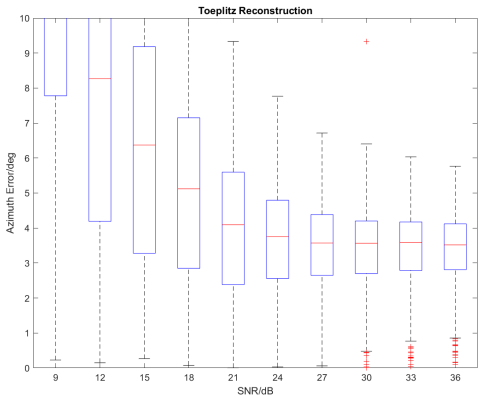

(d) Toeplitz Reconstruction Azimuth

Figure 6.5: Box Plot for Azimuth Estimation

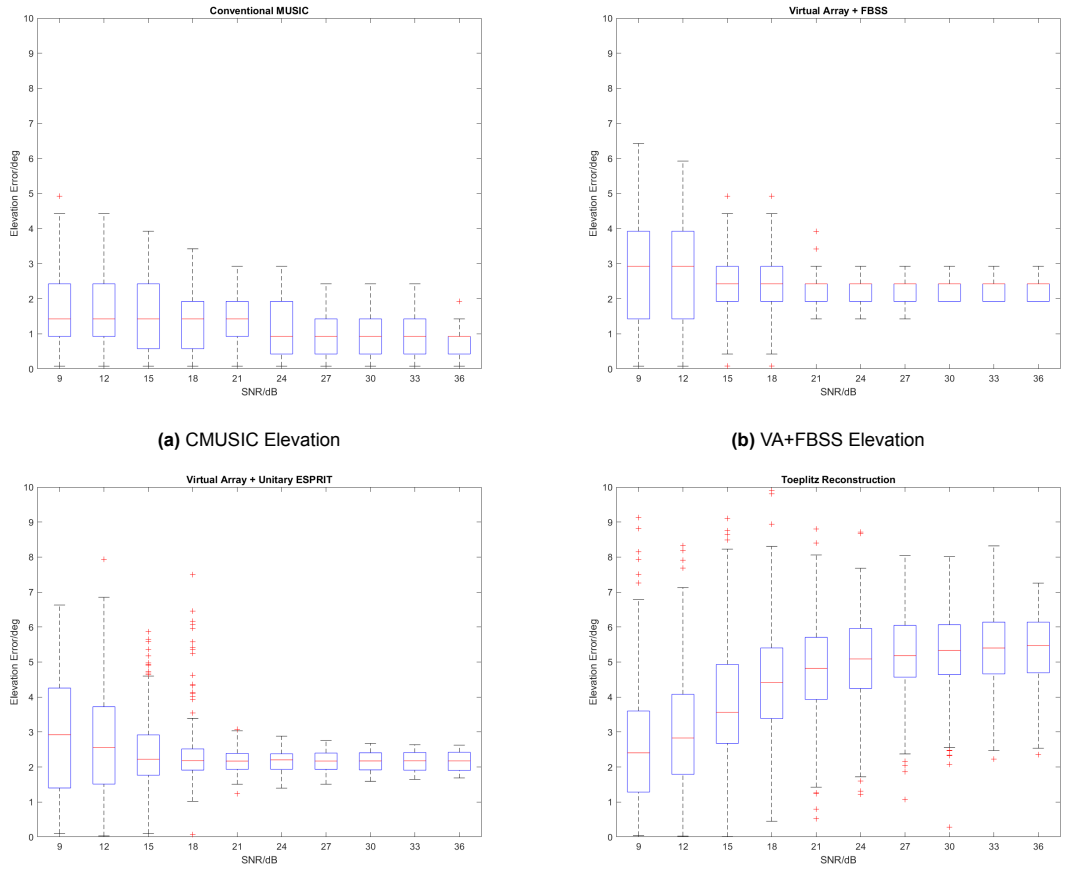

(a) CMUSIC Elevation

(b) VA+FBSS Elevation

(c) Unitary ESPRIT Elevation

(d) Toeplitz Reconstruction Elevationh

Figure 6.6: Box Plot for Elevation Estimation

6.3.1. The Effect of Package Aggregation

The concept of Package Aggregation involves using additional data from other packets to enhance the accuracy of estimation. In practical implementation, it is common to transmit a packet at a regular interval of 20 ms. This time duration is rather brief, allowing us to make the assumption that the position of the target remains constant during this period. According to Yao, the method can incorporate many packets instead of relying just on a single packet [7].

In the simulation, a comparison is made between the errors of both angles with and without packet aggregation using the Toeplitz Reconstruction method. The outcome is depicted in Figure 6.7. As demonstrated, the aggregation of additional data leads to a reduction in the variance of the estimation error. The plot shows the cumulative distribution functions (CDFs) of both angles.

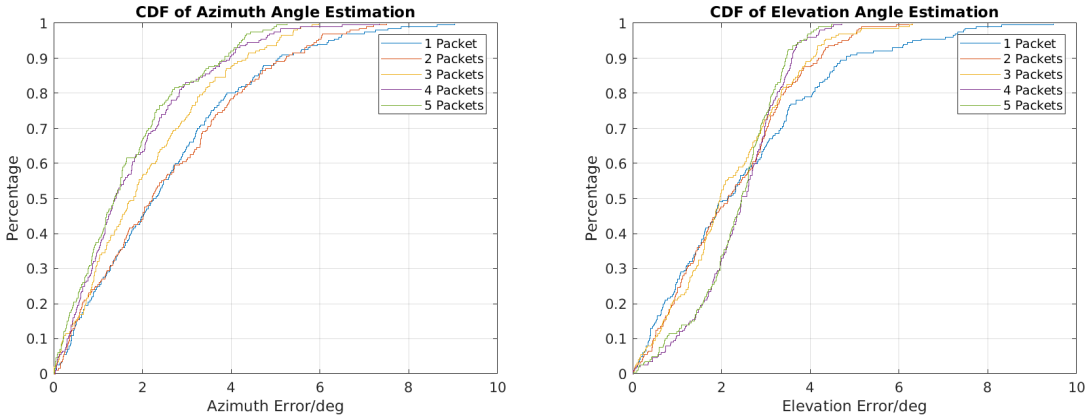

(a) CDF of Azimuth Angle Estimation

(b) CDF of Elevation Angle Estimation

Figure 6.7: CDF with Different Number of Packets Combined with 4×4 URA

Conduct the simulation with a larger URA of size 8×8, the CDF of both angle estimation errors are shown in Fig.6.8. With more data combined, the more accurate the result would be. Comparing to the results obtained with smaller URA, it becomes evident that the data processing method shows a more obvious improvement. This is obvious from the distinct separation observed in the CDF curves when using only one packet as opposed to mixing two packets.

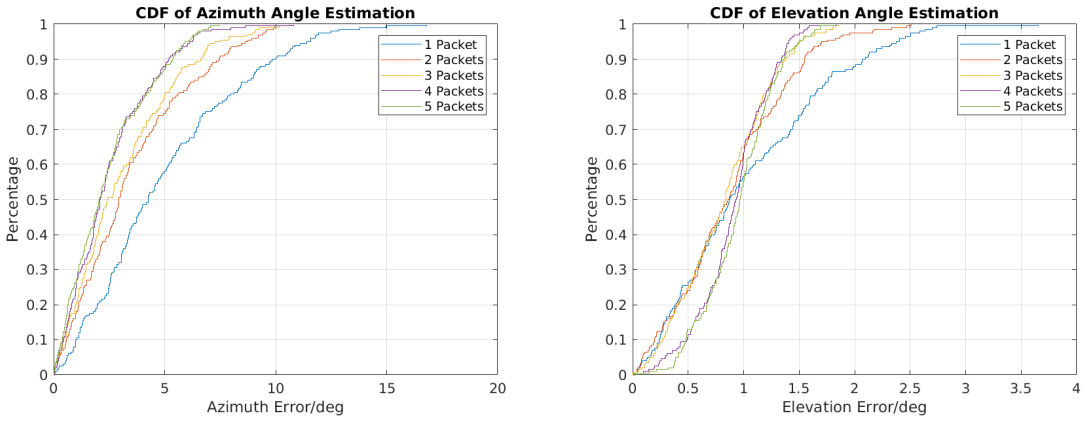

(a) CDF of Azimuth Angle Estimation

(b) CDF of Elevation Angle Estimation

Figure 6.8: CDF with Different Number of Packets Combined with 8×8 URA

As the RMSE improvement from 4 packets to 5 packets is already small(seen in Fig.6.10), and we perfer not assuming the location unchanged for too long, in later simulation, we will combine 5 packets for one iteration of angle estimation.

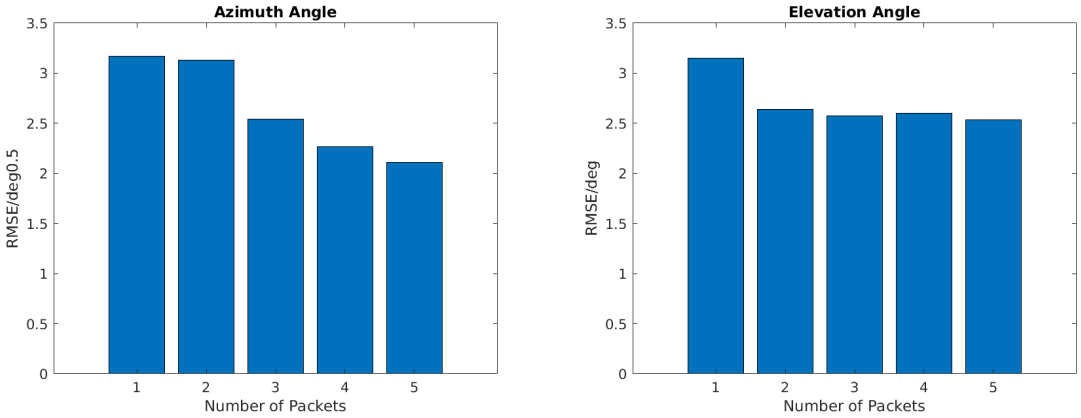

(a) RMSE of Azimuth Angle Estimation

(b) Error of Elevation Angle Estimation

Figure 6.9: RMSE with Different Number of Packets Combined with 4×4 URA

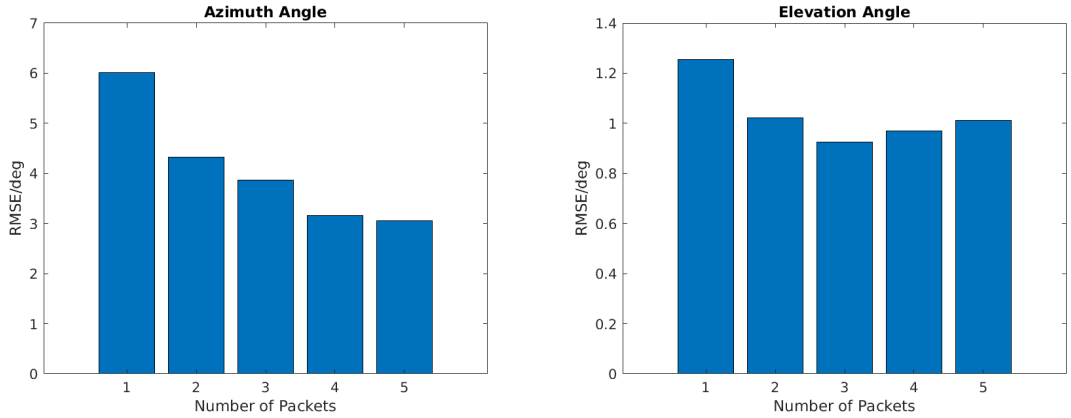

(a) RMSE of Azimuth Angle Estimation

(b) Error of Elevation Angle Estimation

Figure 6.10: RMSE with Different Number of Packets Combined with 8×8 URA

6.3.2. The Effect of Source Number Estimation

In [8], the effect of source number estimation is proven to be trivial for 1-D BLE AoA estimation. However, the impact of this phenomenon on 2-D baseline estimation of AoA using the ESPRIT algorithm has not been addressed.Given that both MUSIC and unitary ESPRIT are subspace-based methods, the way in which the noise subspace or source subspace is generated is directly influenced by the number of sources. This section, the effect of source number estimation will be discussed.

The parameters in the simulation are mostly unchanged after the angle estimation simulation. The signal be transmitted will loop over different number of multipath, the total number of signals changes from 1 (only LOS signal) to 7 (counting all the reflection from 4 walls, floor, and the ceiling). For each signal combination, different numbers of source (from 1 to 10) will be applied in the real estimation process. The accuracy is still presented in the form of RMSE.

In the subsequent simulation, we only examine the impacts of the proposed VA+FBSS+MUSIC algorithm in comparison to the Toeplitz Reconstruction method. The azimuth angle results are presented in Figure 6.11.

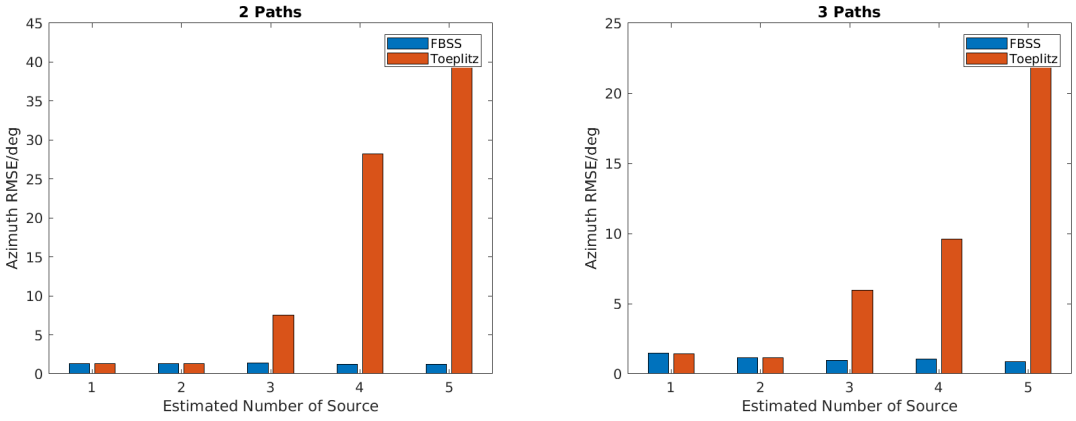

(a) 2 Sources Azimuth

(b) 3 Sources Azimuth

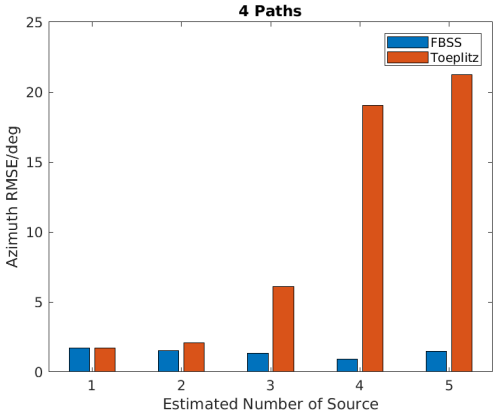

(c) 4 Sources Azimuth

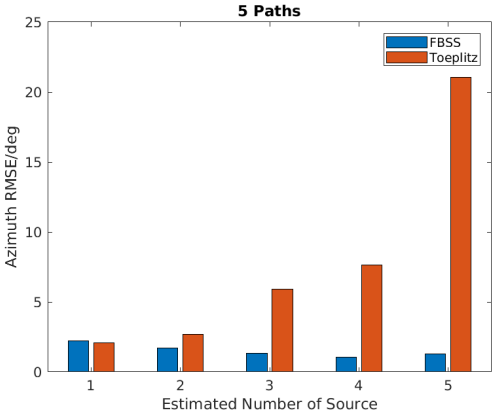

(d) 5 Sources Azimuth

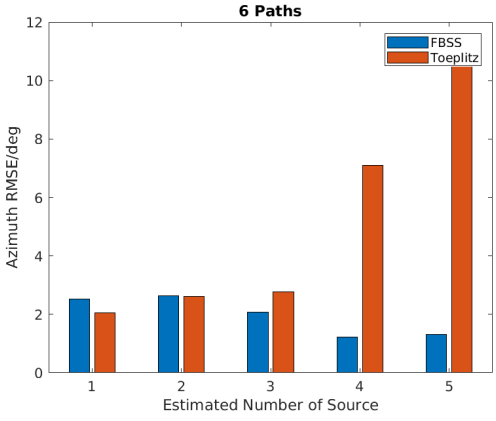

(e) 6 Sources Azimuth

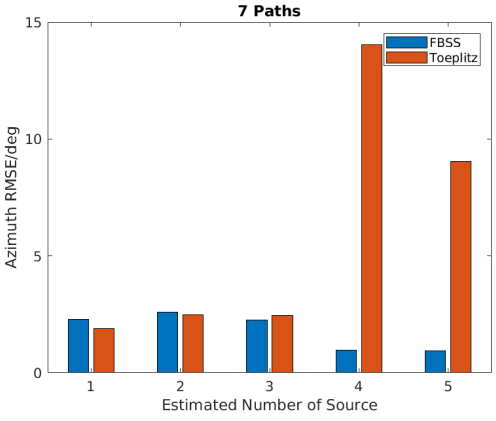

(f) 7 Sources Azimuth

Figure 6.11: Results of Azimuth Angle Estimation of Proposed Methods for Different Source Number Estimation

And for the elevation angle is shown in Fig.6.12:

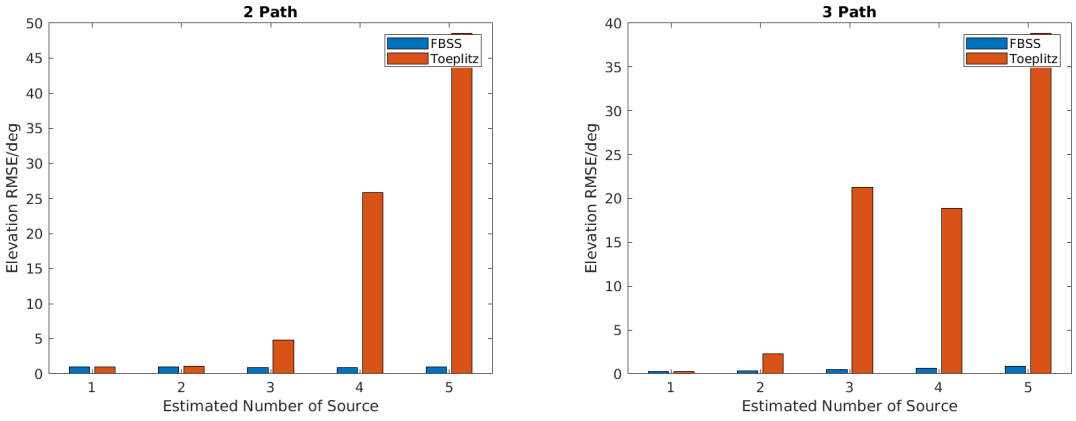

(a) 2 Sources Elevation

(b) 3 Sources Elevation

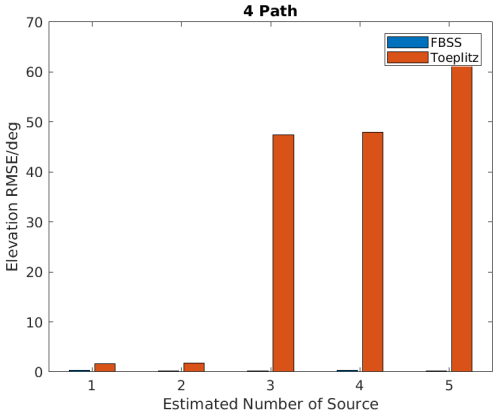

(c) 4 Sources Elevation

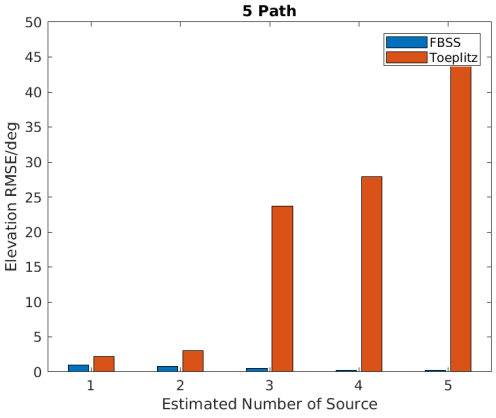

(d) 5 Sources Elevation

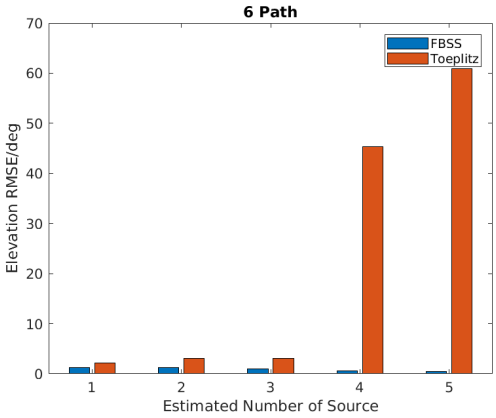

(e) 6 Sources Elevation

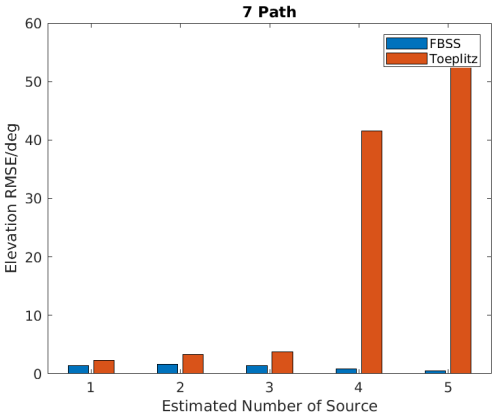

(f) 7 Sources Elevation

Figure 6.12: Results of Elevation Angle Estimation of Proposed Methods for Different Source Number Estimation

The errors of the two proposed methods are provided in Fig.6.11 and Fig.6.12, respectively. In comparison to the Toeplitz approach, the VA+FBSS+MUSIC algorithm demonstrates a reduced sensitivity to variations in the predicted number of sources.

Ensuring the precision of the source number does not necessarily ensure an improved estimation of the angle. This aligns with the findings presented in the simulations conducted by Cloudt et al. [8]. Such a phenomenon may result from the fact that there is only one real source and the other multipath are attenuated, delayed, and phase-shifted versions of it. So all the multipath sources are correlated with the LOS signal. Moreover, it is common for the power level of the reflected routes to be significantly different from that of the LOS signal. The power attenuation often remains below 0.5 of the LOS signal,

even in the case of the most intense reflection. Due to the lack of influence from the number of sources and the inherent inaccuracy of sophisticated source number estimation techniques, we have chosen to set the estimated number of sources as a fixed value of 1 in our further simulations. This decision has yielded improved results for both of the proposed methods.

6.3.3. The Effect of Subarray Size for FBSS

As previously introduced, FBSS decoherents the multipath signals by utilizing the Vandermonde structure with averaged subarray covariance matrix. The number of multipath signals that can be decorrelated by this method is constrained by the size of subarray. Hence, we want to investgate how the size of subarray can affect the angle estimation.

Both a 4×4 and a 8×8 URA were utilized in this study. The RMSE in relation to the subarray size is illustrated in Fig.6.13. In this plot, the x-axis represents the size of the subarray in one direction, denoted as $M_s = N_s = x_{\text{value}}$, rather than the total number of antennas within a subarray.

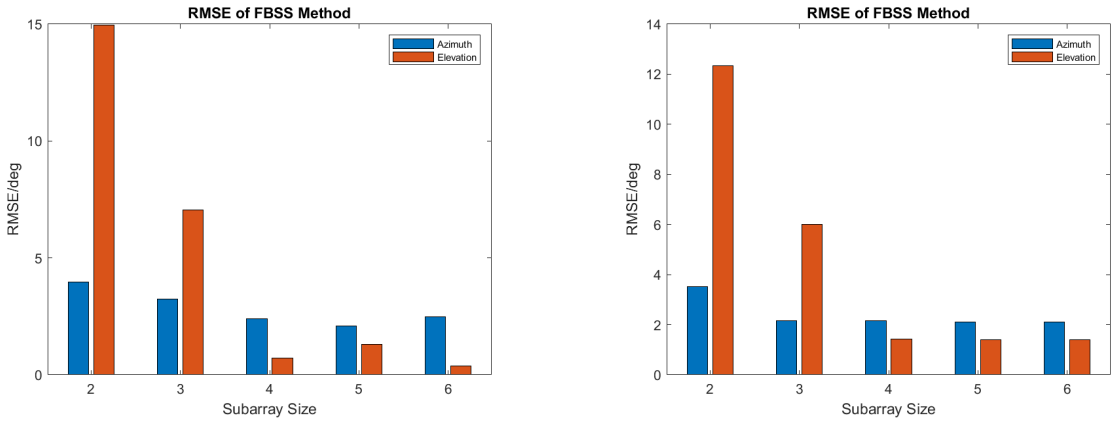

(a) RMSE of Differnt Subarray Size with 4×4 URA.

(b) RMSE of Differnt Subarray Size with 8×8 URA.

Figure 6.13: Illustration of Subarray Size Effect

In general, it can be observed that as the size of the subarray increases, there is a corresponding decrease in the RMSE. Nevertheless, the effectiveness of the FBSS method is not solely determined by the subarray size, which refers to the total number of antennas within a given subarray. It is also associated with the overall number of subarrays (the overall number of smoothing). In a given URA, it is observed that as the size of the subarray increases, the degree of smoothing that may be applied in both directions decreases. This is the reason why the size of subarrays, specifically those with dimensions of 4×4 and 6×6, shows little variation. In subsequent simulations, the subarray size was held constant at 4×4.

6.3.4. The Effect of PQ Values for Toeplitz Reconstruction

As previously said, in order to fully restore the rank of the covariance matrix, it is essential to carefully determine the values for P and Q. The impact of PQ values on both angles in various sizes of URA is seen in Fig.6.14. In the provided figure, the x-axis is labeled as 'PQ Value' and represents the value of a single parameter. It is assumed that the values of P and Q are equal.

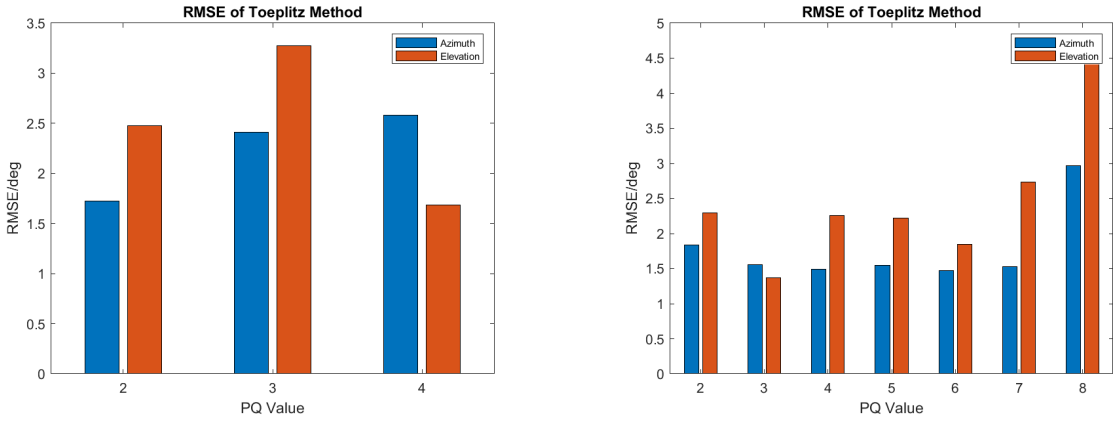

(a) RMSE of Differnt PQ Values with 4×4 URA.

(b) RMSE of Differnt PQ Values with 8×8 URA.

Figure 6.14: Illustration of PQ Value Effect

The limited range of P/Q values in Toeplitz reconstruction is due to the structure of a 4×4 URA. In general, the variance range associated with Toeplitz methods is rather small. The RMSE difference between the most negative case in a 4×4 URA is less than $1°$, whereas for a 8×8 URA, it is less than $3°$. The optimal performance is observed when both the bigger URA and smaller URA have equal values of P and Q, namely P = Q = 3. Therefore, in subsequent simulations, the values of P and Q are set to a constant value of 3.

6.3.5. The Cone of Interest

In prior studies concerning one-dimensional BLE localization using URA, it has been observed that not all angles exhibit equivalent accuracy, even when subjected to same conditions such as SNR, distance, and estimate method. The accuracy of the direction of arrival decreases when the angle of arrival approaches either end of the antenna array, specifically when the angle of arrival is closer to 0° or 180°. In the study conducted by Cominelli et al. , it was observed that the estimation results exhibit a high degree of variation within the range of $0° < \theta < 10°$. Consequently, this range was deemed unreliable and excluded from further analysis [54]. In a separate study by Ye et al., the focus was narrowed down to a narrower range of $20° < \theta < 160°$ for the cone of interest [6]. In the context of a more intricate interior setting, the cone of interest can be constrained to an angular range between 50° and 130°.

The concept of a cone of interest in 3-D space has challenges in defining it within the context of URA. To determine the optimal range of locations with optimum accuracy, a subsequent simulation is performed, whereby a plane is scanned instead of a single point. The illustration is depicted in Fig.6.15. The estimation process is iterated 200 times for each SNR value. The plane in which the transmitter is situated is the y-z plane, which is colored blue. All numerical values depicted in the diagram are expressed in the unit of meters. The locator remains fixed at position (-1.2, 0, 2) while the transmitter moves on the plane, each time moving its location by 0.5 meters in either the y or z directions. In this particular configuration, the azimuth range spans from -75.964° to +75.964°, while the elevation range extends from -59.036° to +59.036°.

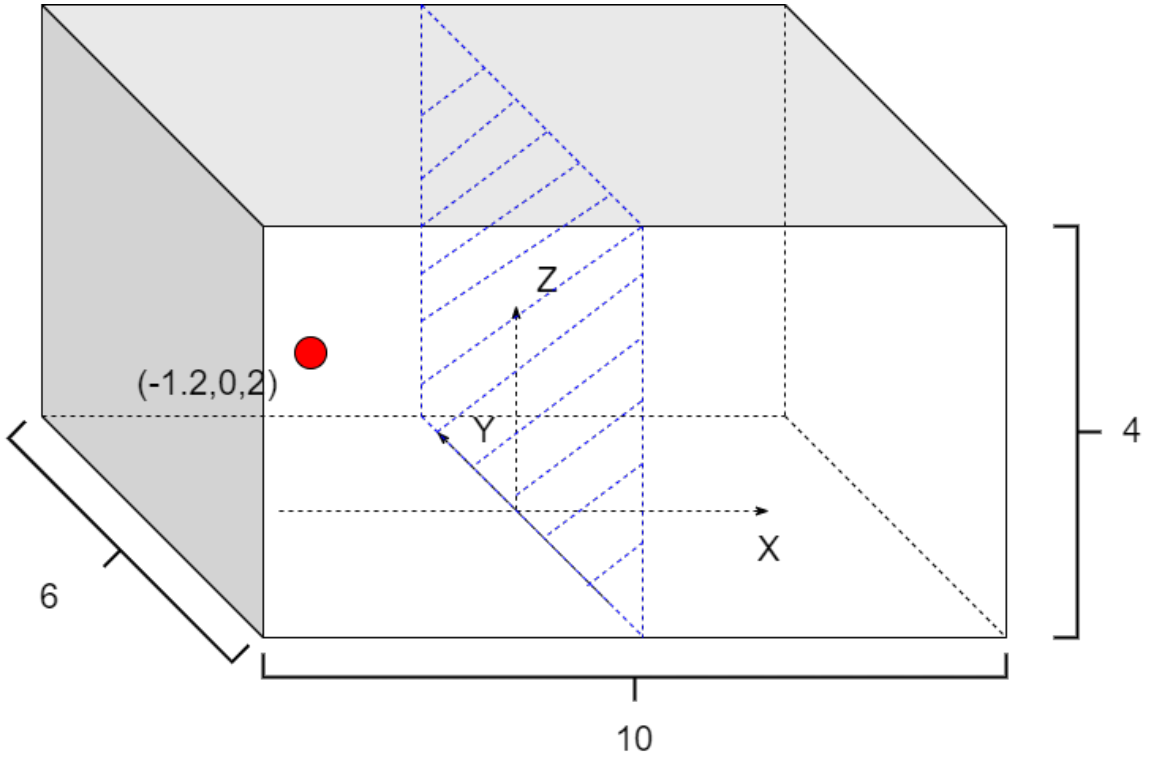

Figure 6.15: Illustration of Plane Scanning Simulation.

In general, the estimation of azimuth angles is most accurate when they are around 0°. As the angles deviate farther in either the negative or positive directions, the magnitude of the estimation error increases. The variations in elevation angles across all methods show less magnitudes as compared to their corresponding azimuth errors. Likewise, when the distance between the transmitter and the locator increases, the inaccuracies in the estimation of elevation angles become greater. The heat map shows certain symmetrical patterns wherein origin-symmetric positions experience comparable levels of estimating errors.

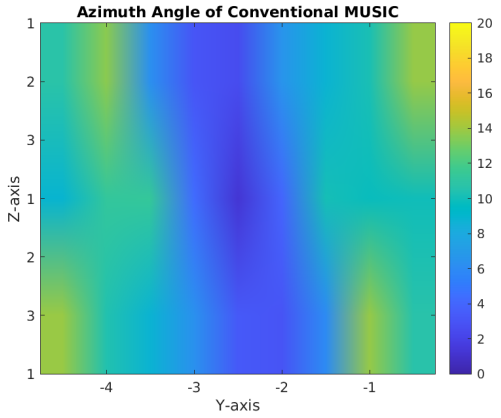

(a) Azimuth CMUSIC

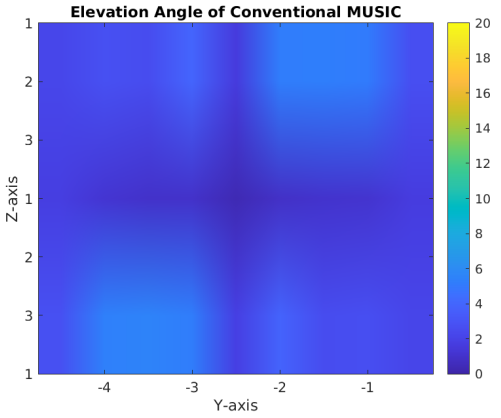

(b) Elevation CMUSIC

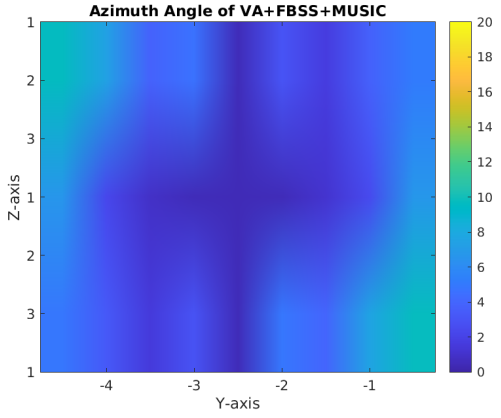

(c) Azimuth VA+FBSS+MUSIC

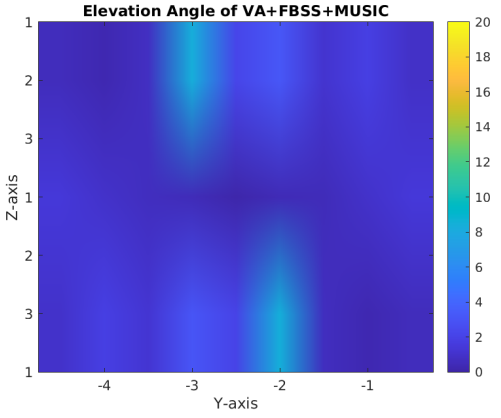

(d) Elevation VA+FBSS+MUSIC

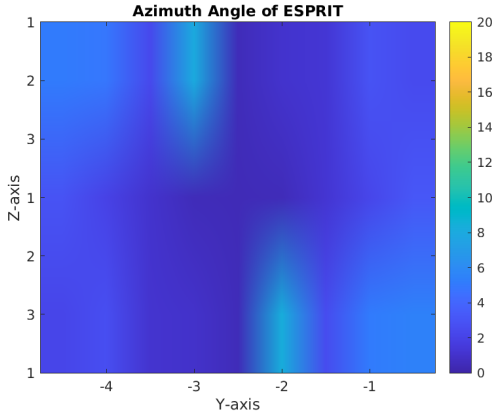

(e) Azimuth ESPRIT

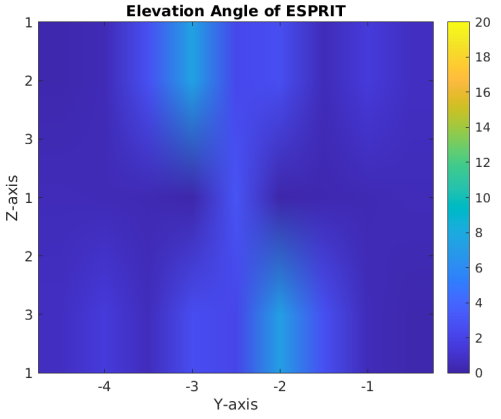

(f) Elevation ESPRIT

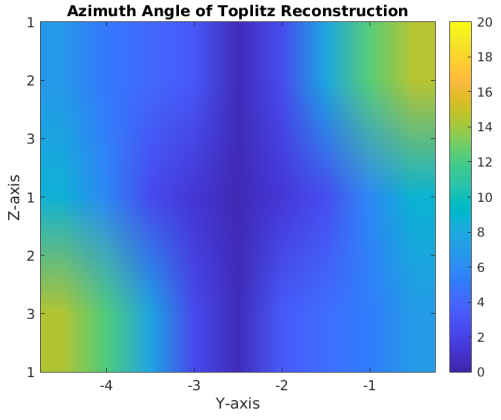

(g) Azimuth Toeplitz Reconstruction

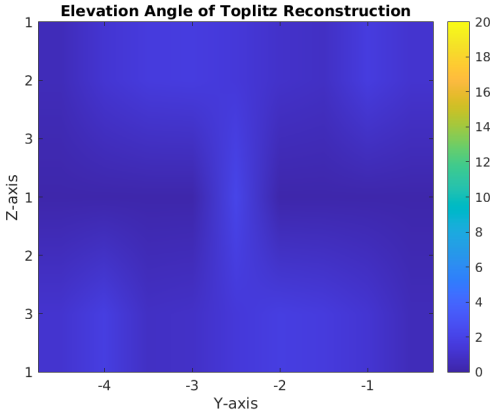

(h) Elevation Toeplitz Reconstruction

Figure 6.16: Results of Angle Estimations of Proposed Methods for Different Node Position

Fig.6.17a and 6.17b display the CDF of the estimation for azimuth and elevation angles, respectively. In regard to azimuth angles, it is seen that over 90% of the outcomes obtained from the three proposed methods display an error level below 10°, but the corresponding percentage for the CMUSIC method is approximately 50%. In terms of elevation angles, it has been found that over 90% of the Toeplitz Reconstruction results show an error level below 2°. In contrast, the unitary ESPRIT and FBSS methods yield an accuracy rate of 70% in achieving an error level below the aforementioned level. The percentage for CMUSIC is significantly lower than 40%. These two graphs provide further evidence of significant improvements in estimating both angles compared to the conventional MUSIC method.

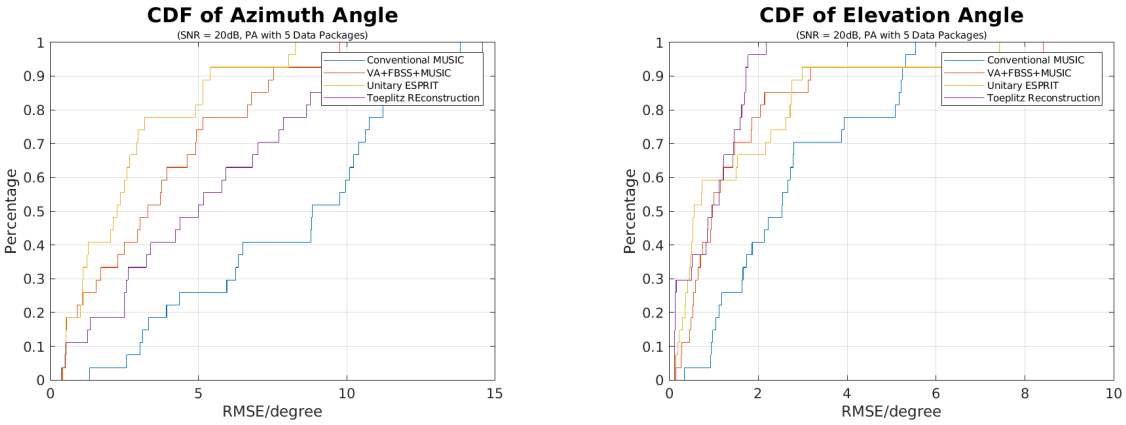

(a) CDF of Azimuth Angles Errors

(b) CDF of Elevation Angles Errors.

Figure 6.17: CDF of Proposed Methods with 4×4 URA

Despite the inherent limitation of the array size being restricted to 4×4, it is still feasible to conduct a simulation on a bigger URA. Yet, the upper limit of the array size is determined by the maximum length of the CTE packet. The maximum length of the URA is 160µs, with each sample slot and switch slot having a duration of 1µs. The URA size is limited to a maximum of 8×8. Therefore, the aforementioned simulation is repeated with the larger URA. Fig.6.18 illustrates the CDF of the angles for all methods.

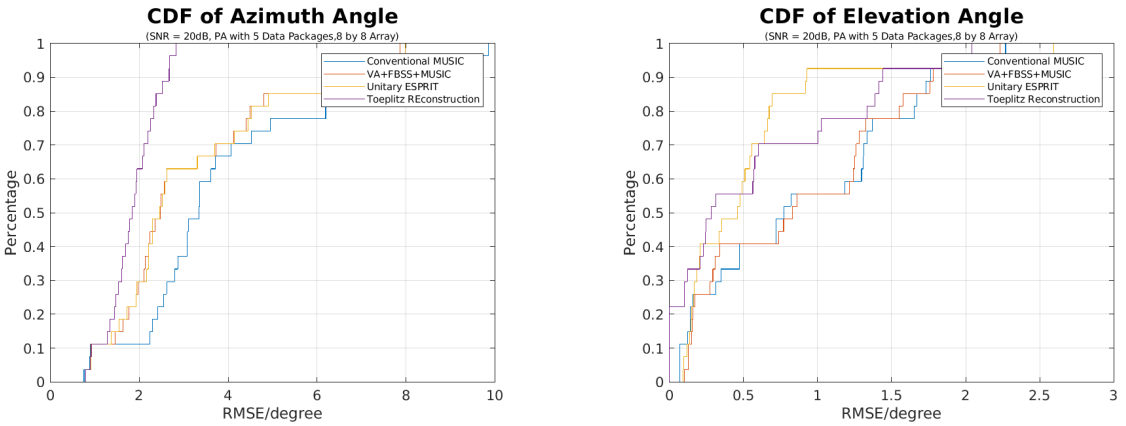

(a) CDF of Azimuth Angles Errors

(b) CDF of Elevation Angles Errors.

Figure 6.18: CDF of Proposed Methods with 8×8 URA

The accuracy in both angles improved with a bigger antenna array, which is consistent with the theoretical expectations, when compared to the findings obtained from a 4×4 URA. The majority of Toeplitz results, around 90%, have azimuth estimation errors below 2°. In contrast, other methods yield results with errors below 6° in approximately 80% of cases, indicating an improvement of approximately 4°. In terms of the elevation angle, it can be observed that over 80% of the obtained outcomes

show errors that are below 1.5°, while in a smaller array 80% of the errors are below 5°. This observation demonstrates that as the size of the array increases, there is a general decrease in the level of inaccuracy.

6.4. Position Estimation Simulation

This part will focus on the simulation of positioning. The simulation continues to be done using the same empty room model.

First, assume there are in total 4 locators on the center of each wall and their positions are known, seen in Fig.6.19. The objective is to create a maximal intersection space for the four cones of interest of all locators based on this assumption.

For locators numbered 1 and 3 in Fig.6.19, the range of azimuth angles and elevation angles are naturally more limited than the other two locators. To simplify the case, all four locators are limited to the minimum scanning range of the former two. In other words, the azimuth angles are limited to the range of $\phi \in$ (- 30.964°, +30.964°) and $\theta \in$ (- 21.801°,+ 21.801°). All these angle ranges are computed in their respective local coordinate systems, which are not always aligned with the global one. The intersection of these cones of interest and their projection onto the x-y and x-z planes are illustrated in Fig.6.20.

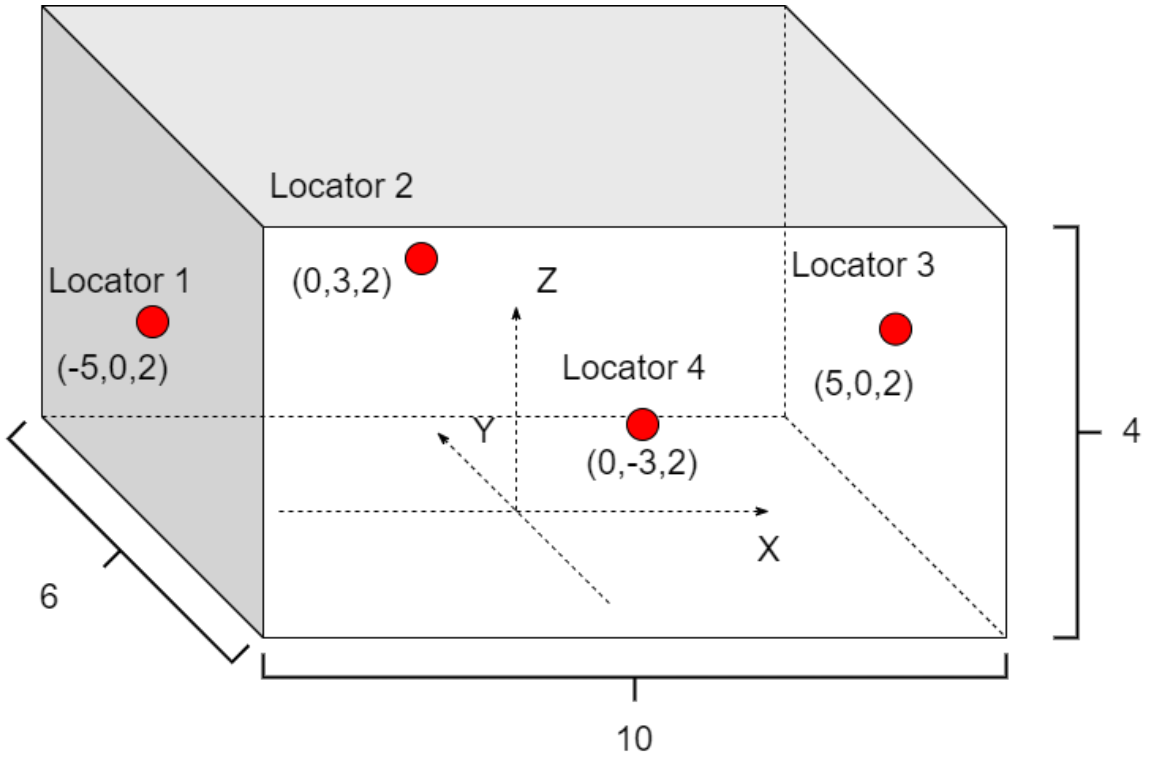

Figure 6.19: Illustration of 4 Locators in the Empty Room.

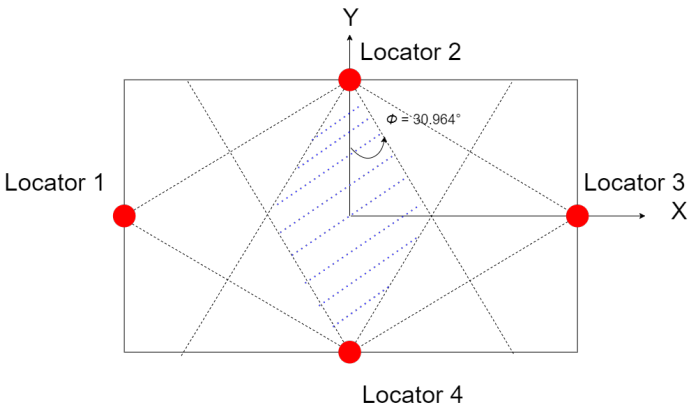

(a) Projection on X-Y Plane

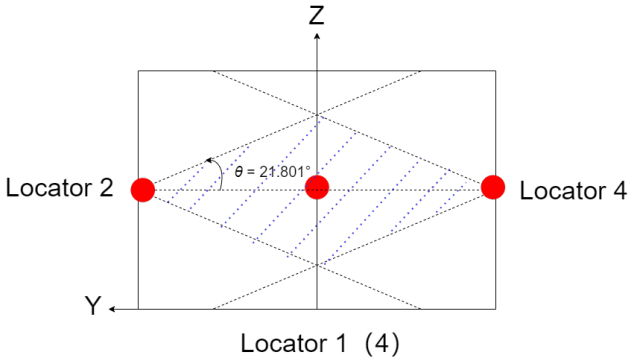

(b) Projection on Y-Z Plane

Figure 6.20: Projections of Cones of Interest on Different Planes

Results are shown in Fig.6.21 and Fig.6.22 in the forms of box plot and CDF respectively. The box figure illustrates that the Toeplitz reconstruction algorithm shows a comparatively smaller median error (represented by the red line) of 0.11 m, whilst the FBSS methods demonstrate higher errors, approximately 0.17 m. When executing the simulation on a larger 8×8 array, it is observed that the FBSS approaches show instability with increased variation. The errors observed in the results of this research exceed 0.5 m. The median results for both the TR method and the FBSS method exhibit a drop, specifically 0.09 m for the TR method and 0.12 m for the FBSS method. This implies that by employing a larger antenna array, as previously demonstrated to enhance angle estimation accuracy, there will also be a corresponding improvement in position estimation accuracy.

The analysis of two CDF graphs reveals that, in the case of a 4×4 array, the combination of angle estimate methods with both LS and TLS locationing algorithms results in errors that are below 0.2 m. Generally, the TR algorithm shows more accuracy in the estimation of final location. In the case of an 8×8 array, the performance of both methods is similar. The box plot demonstrates that the TR method exhibits lower variation compared to the FBSS approach.

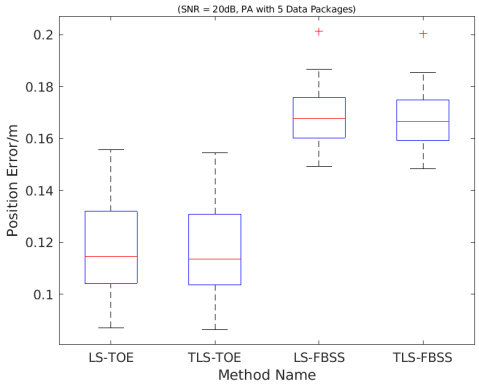

(a) Positioning Error with 4 by 4 Array

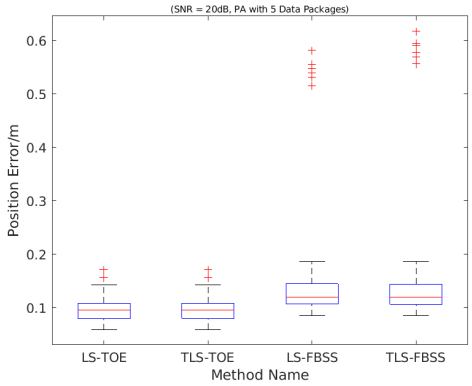

(b) Positioning Error with 8 by 8 Array

Figure 6.21: Box Plot of Position Errors.

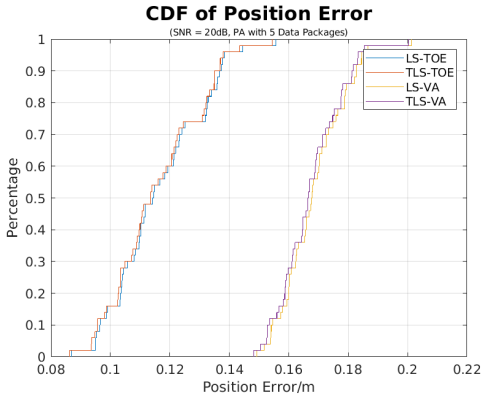

(a) CDF of Positioning Error with 4 by 4 Array

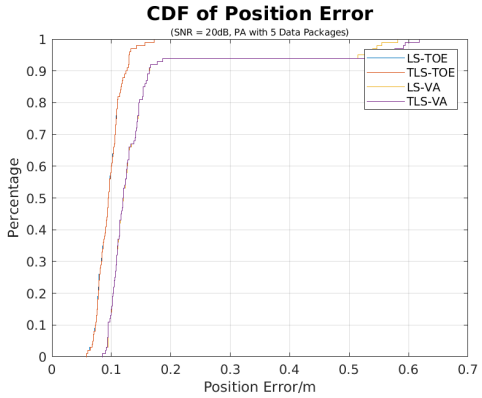

(b) CDF of Positioning Error with 8 by 8 Array

Figure 6.22: CDF of Positioning Error.

6.5. Conclusion

In this section, a series of simulations were performed to evaluate several aspects including the CFO, the number of packets aggregated, the estimated number of sources, the parameters in the algorithm, the accuracy of the angle estimation methods, and the accuracy of the positioning methods. The process of Matlab BLE signal generation and the ray-tracing technique were introduced. The results shows that, with approprate parameters, the TR algorithm demonstrates the best angle estimation with errors of near 1° for both azimuth and elevation angles. After combining the TR angle estimation with LS/TLS positioning estimation, it is shown that over 90% of the positoning errors are less than 0.14 m. Both the angle and position estimation would be enhanced by employing a larger URA.

7

Experiment

This chapter mainly presents an overview of the experimental setup, the obtained results, and the subsequent analysis.

7.1. Enviornment Setup

The hardware support for both the transmitter and the locators utilized in this project is provided by Nordic Semiconductor company. The transmitter/tag employs a nRF52833 development kit (DK), as depicted in Figure 7.2. The nRF52833DK is a single-board kit designed for various communication applications, including BLE), utilizing the nRF52833 multi-protocol System-on-Chip (SoC) [55]. In this project, the typical method of USB powering through an external power station is employed, although there are other alternative ways of powering. The chip itself is shown in Fig.7.1. The nRF52833 is a multi-purpose SoC that supports many protocols and features a radio with Bluetooth Direction Finding capability. It has been certified for operation within an extensive temperature range spanning from -40$^{\circ}C$ to +105$^{\circ}C$. The nRF52833 chip, which is the latest addition to the acclaimed nRF52 Series, features a 64 MHz Arm Cortex-M4 with FPU. It offers 512 KB flash and 128 KB RAM memory, making it suitable for applications that require enhanced performance and functionality [56].

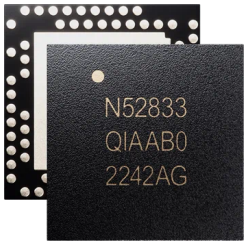

Figure 7.1: nRF52833 Multiprotocol SoC.

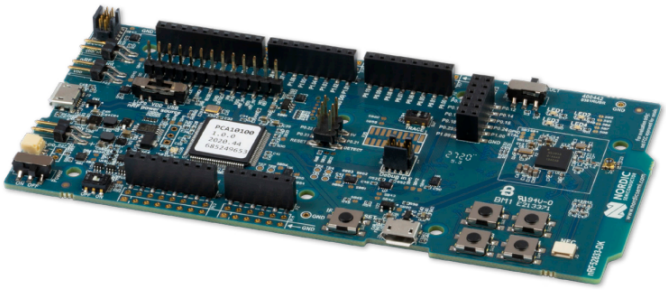

(a) Illustration of an nRF52833 DK, taken from[55]

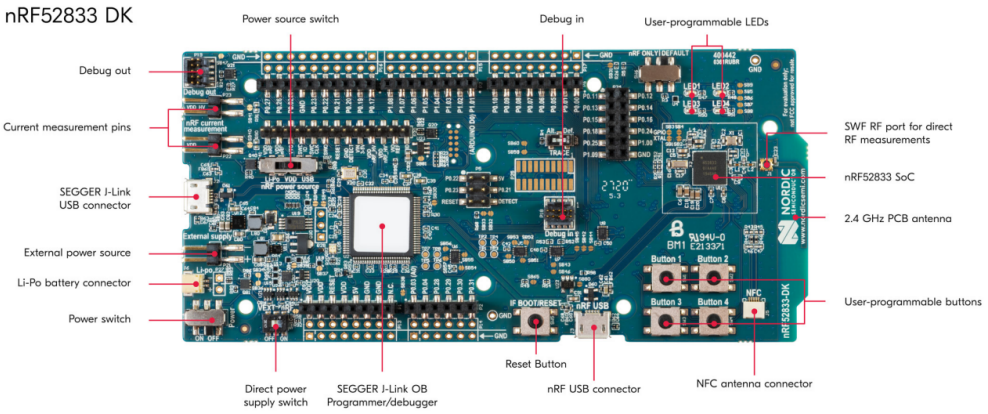

(b) Detailed Illustration of an nRF52833 DK

Figure 7.2: Illustration of the Tag

The 12 antenna rim URA provided by Nordic is utilized as the receivers/locators, as depicted in Fig.2.6. When the CTE signal impinges the antenna, the I/Q sampling is done by the array. The information from each locator is subsequently transmitted to the data center. Several data reports from various locators are then delivered from the data center to the computer via USB connection. The estimating algorithm is executed by the computer. The work flow is depicted in Fig.7.3 and an illustration of the enviornment setup is in Fig.7.4.

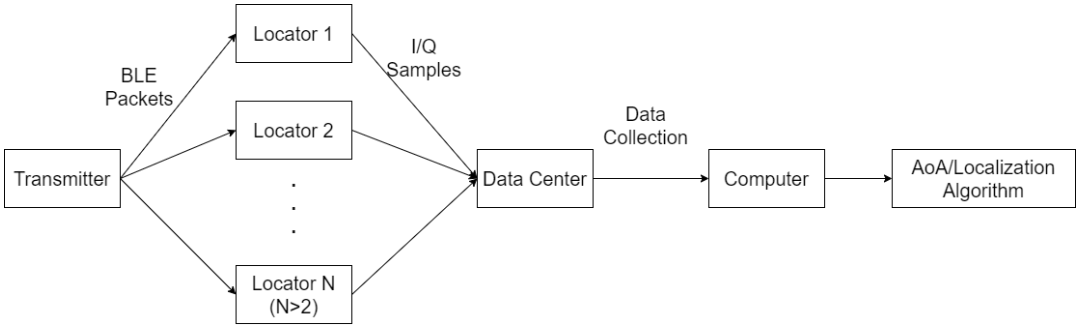

Figure 7.3: The Experiment Work Flow Chart.

Name	Coordinates/m
Locators	
Locator 1	(0,1.123,0.383)
Locator 2	(-1.522,0,0.497)
Locator 3	(1.340,0,0.500)
Transmitter	
Experiment 1	(0,0,0)
Experiment 2	(0.289,0.290,0)
Experiment 3	(0,0,0.795)

Table 7.1: Coordinates of Locators and Transmitter in the Experiment

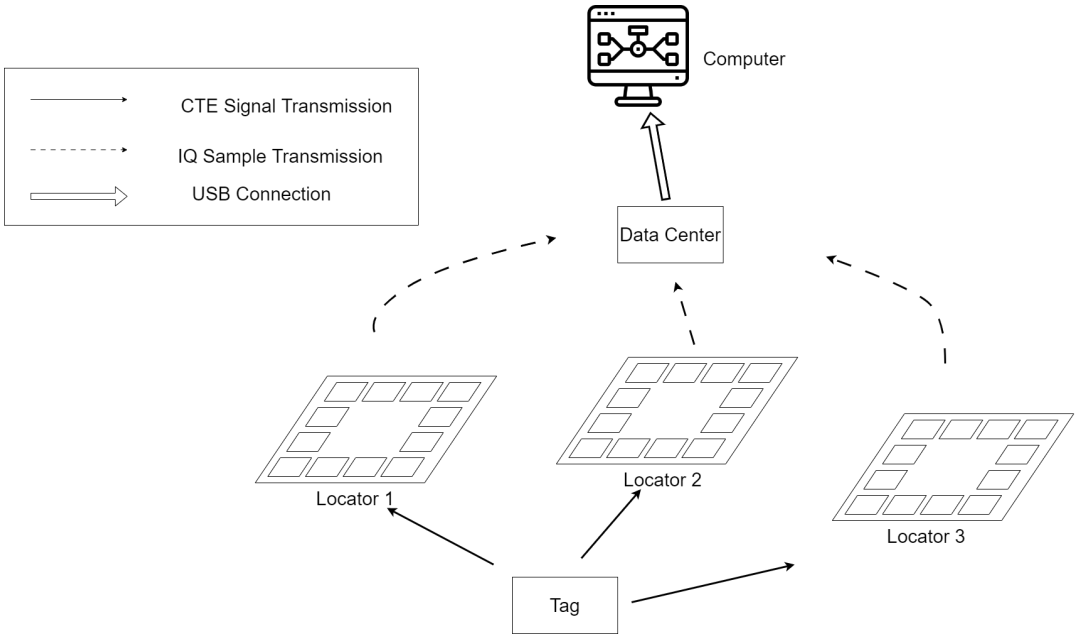

Figure 7.4: Experiment Setup.

During the experiment, since the position of the tag affects the estimation accuracy, three distinct positions for the tag were examined. The coordinates of the transmitter and locators are listed in Tab.7.1 below.

7.2. The Validity of the Data

The stability of the connections between the transmitter and each locator may vary during the duration of the experiment. Fig.7.5 shows the status of connection for packets in all three locators along the time (the events). The y-axis of Fig.7.5 is the number of valid reports sending to the data center, indicating the stability of the connection. Only packets with 3 reports were considered totally stable and sent to later process. The x-axis is the event counter, denoting discrete time instants of the transmissions. The figure illustrates that the efficacy of a connection is significantly influenced by its status.

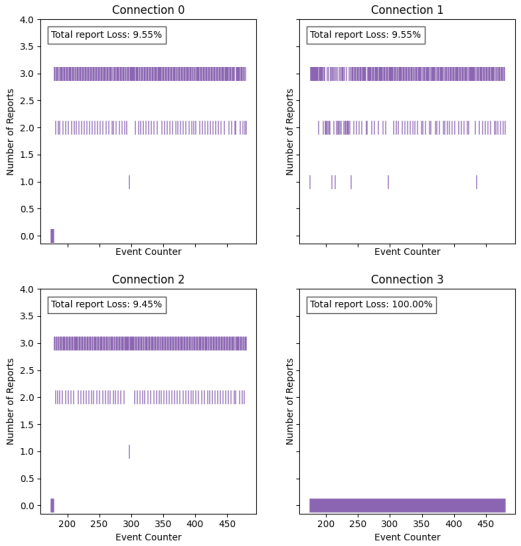

(a) Experiment 1

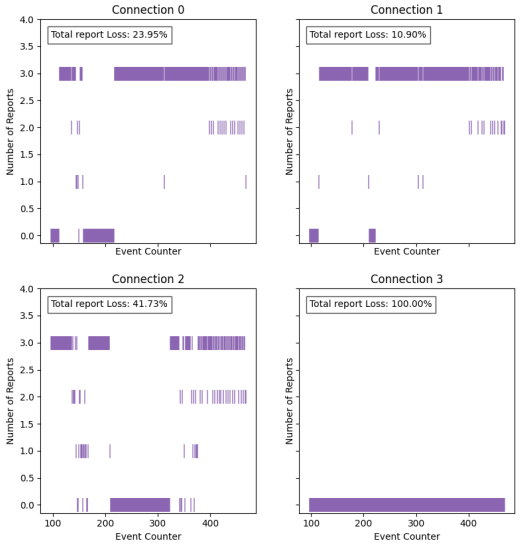

(b) Experiment 2

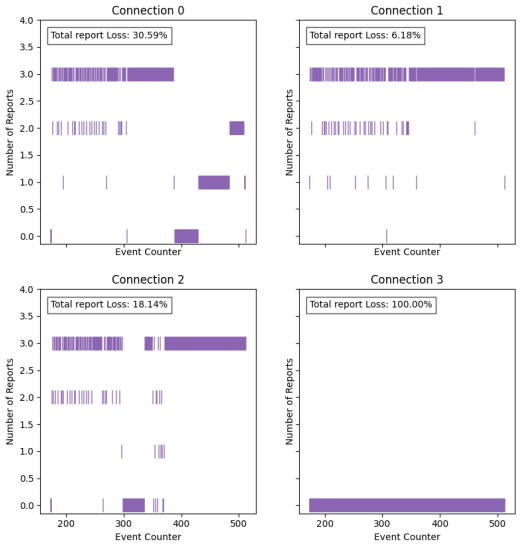

(c) Experiment 3

Figure 7.5: Packets Status in Three Experiments

The correspondence of Connection 0-2 and specific locators is not always fixed but related to the starting order when turning on each locator. The correspondence between the order of locators and the order of connections in each experiment are listed in Tab.7.2.

Experiment Number	Connection Number	Locator Number	Number of Valid Packets
Experiment 1	Connection 0	Locator 2	302
	Connection 1	Locator 1	302
	Connection 2	Locator 3	302
Experiment 2	Connection 0	Locator 1	175
	Connection 1	Locator 2	175
	Connection 2	Locator 3	175
Experiment 3	Connection 0	Locator 1	250
	Connection 1	Locator 2	250
	Connection 2	Locator 3	250

Table 7.2: Experiemnt Details

7.3. Angle of Arrival Experiment

Once the data was obtained from the data center, it was imported into the Matlab code and subsequently analyzed. The practical measurements in each experiment for each locator were partitioned into distinct Monte-Carlo experiments, with 10 packets in each experiment. In experiments 1, 2, and 3, there were 30, 17, and 25 estimations, respectively.

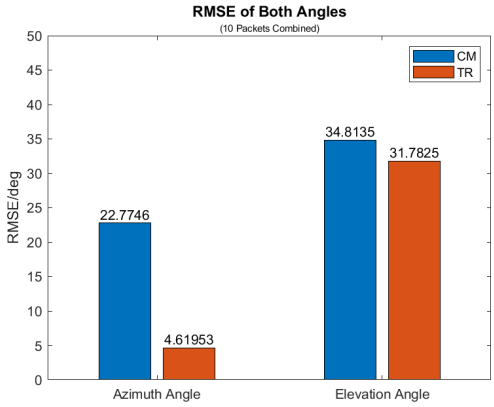

(a) Experiment 1

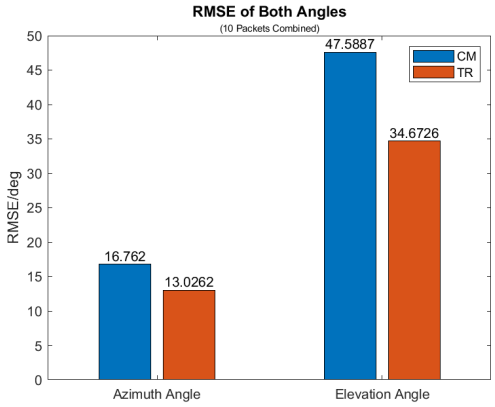

(b) Experiment 2

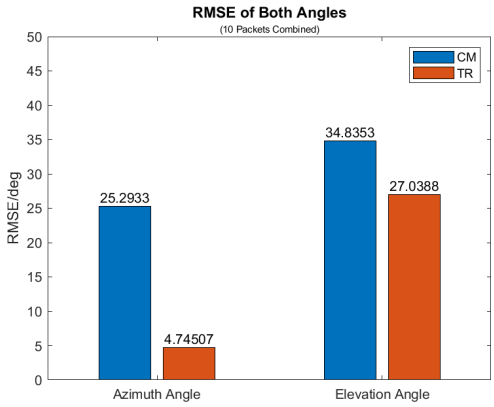

(c) Experiment 3

Figure 7.6: RMSE of Both Angles in Three Experiments

The results within a single experiment with different numbers of packets combined are shown in Fig.7.7. With more packets of data combined in one single estimation, the accuracy in both azimuth angle and elevation angle is improved. By increasing the number of packets combined from 3 to 20, the RMSE of azimuth angle decreased from 9.75828° to 3.43497°, improved 64.80%; the RMSE

of elevation angle decreased from 33.4033° to 31.559°, improved 5.52%. Increasing the number of packets combined does not improve the accuracy of the CM method as much as the TR method.

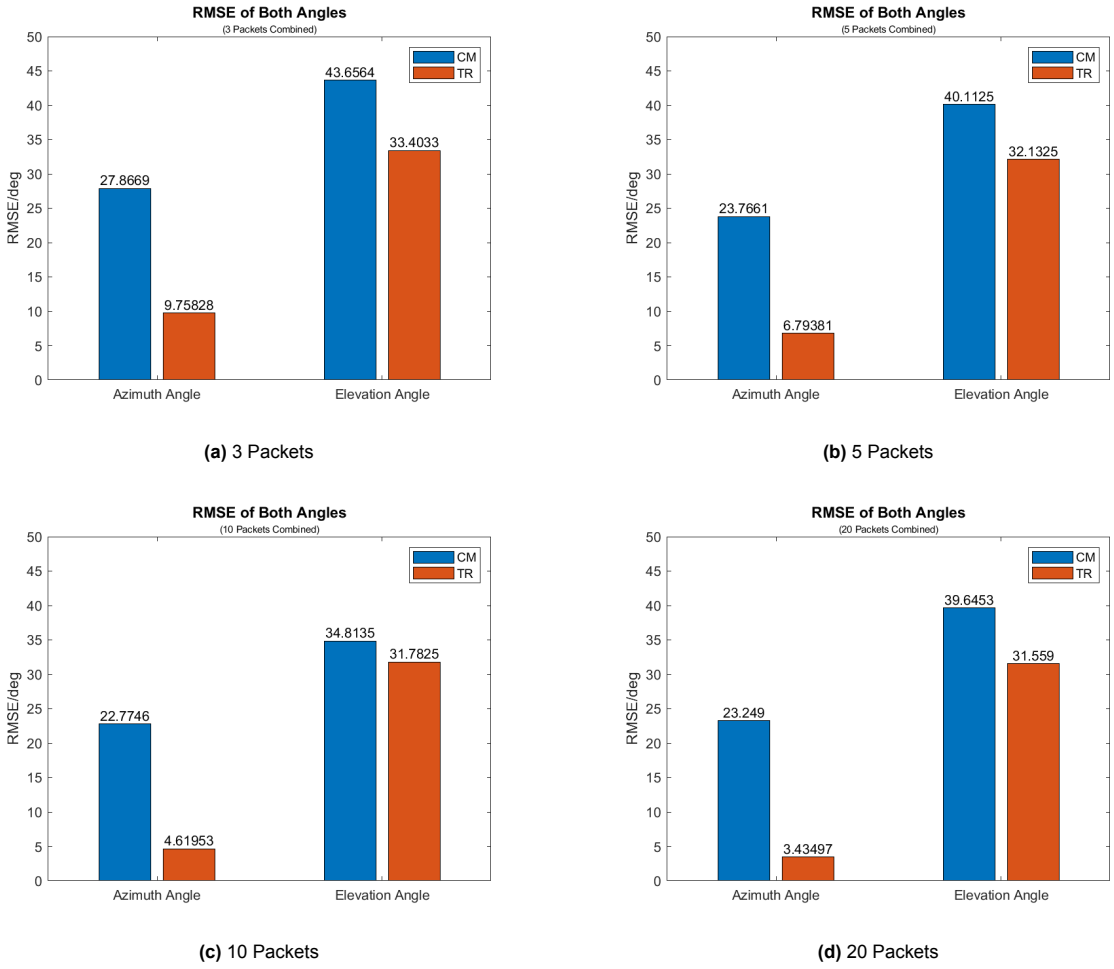

(a) 3 Packets

(b) 5 Packets

(c) 10 Packets

(d) 20 Packets

Figure 7.7: RMSE of Both Angles in Experiment 1 with Different Number of Packets Combined

The results of angle estimation error for all three experiment are shown in Fig.7.6. As we can see, the TR methods outperform the CM methods in both azimuth and elevation methods. For azimuth angle, TR method enhanced accuracy by 79.72%, 22.29%, and 81.24% than the conventional method. For the elevation angle, the accuracy improved by 19.19%, 27.14%, and 22.38%. Comparing to previous research, the azimuth angle performance is comparable of around 5° using the same hardware but only utilize the ULA subarray[9], and is improved with the azimuth estimation of indoor scenario using simple phase difference method other than subspace methods [54]. The fail in elevation angle may result from stronger multipath profile with the reflections from the ground and paper boxes on the elevation plane.

7.4. Localization Experiment

Prior to inputting the calculated angles into the positioning algorithm, it is necessary to perform a coordinate transformation procedure in the practical experiment. The calculated angles for each location are shown in the local coordinates, as depicted in Fig.2.7. In order to determine the position, it is necessary to convert each set of angles into a global coordinate system. The aforementioned transformation is just applied to the azimuth angle, while the definition of the elevation angle remains unaltered when the coordinate axis is rotated.

An illustration of azimuth transformation is shown in Fig.7.8 with an aerial view. In the figure, the azimuth angle from the transmitter to locator 2 is changed from ϕ_2 to ϕ_2' which satisfy $\phi_2' = \phi_2 - 90°$ or $\phi_2' = \phi_2 + 270°$ if we set the range of global angle values as $[0°, 360°)$.

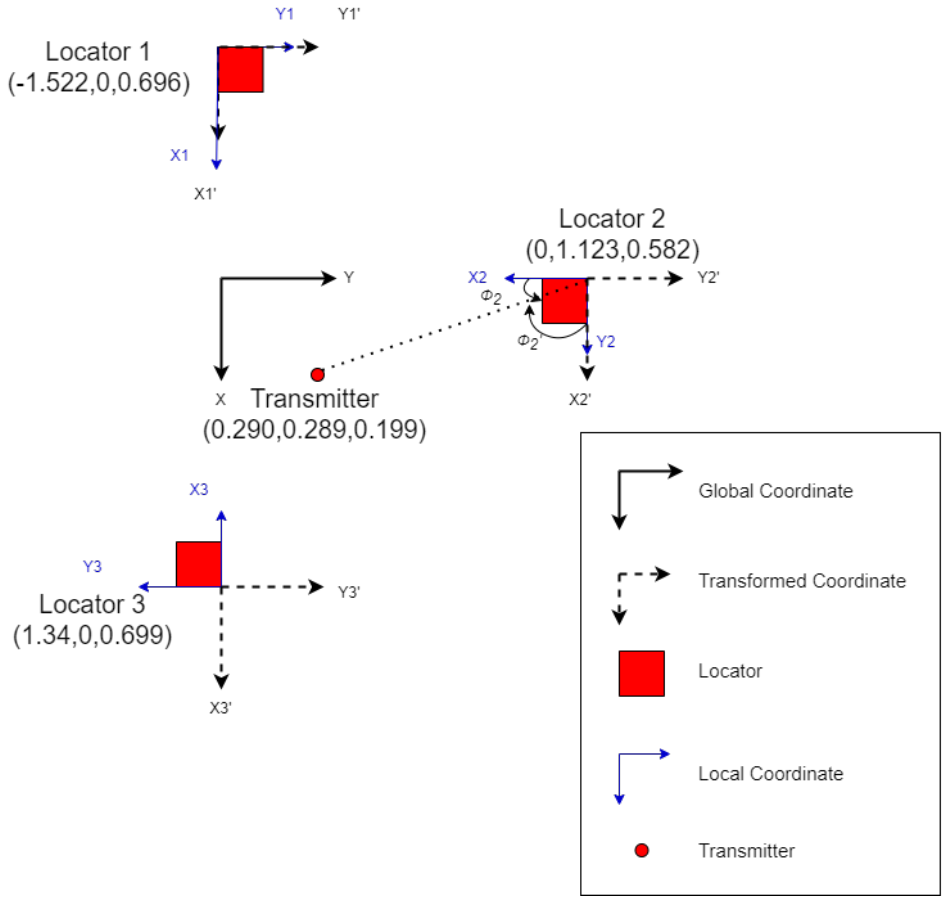

Figure 7.8: Illustration of Coordinates in Experiment 2.

The experiment results of three experiments are shown in Fig.7.9. TR method shows better performance with lower average positioning error and less variance of results. In experiment 1, more than 90% of the TR+LS results are 0.5 m away from the true position, while 90% of the CM results have errors more than 0.8 m. In experiment 2, nearly 90% of the TR+LS results are 0.60 m away from the true location, but for CM method 90% of the results are 1.00 m away. In experiment 3, nearly 95% of the results with TR+LS method is 0.50 m away from the true spot but 95% of the results with CM method are 1.00 m away.

The position estimation results are comparable with previous BLE position research. With the two-point locationing method and only utilizing ULA, the distance errors are guaranteed to not exceed 2 m [9]. By combining 30 packets per channel for ULA of 2 antennas, 95% of the positioning estimation results are below 0.85 m in [54]. The possibilities of a positioning error lower than 1 m were improved from 50% in [54] to 89%, 80%, and 80% respectively with 3 different channels [6]. While with the TR+LS method, the possibility of positioning error lower than 1 m is 100% in all experiments.

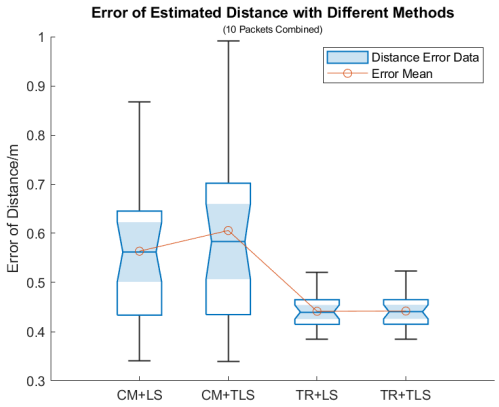

(a) Distance Errors in Experiment 1

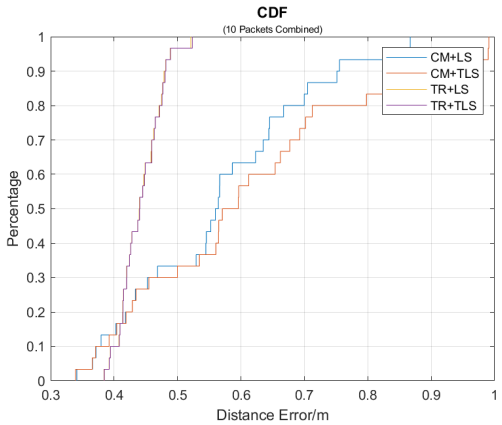

(b) CDF of Distance Errors in Experiment 1

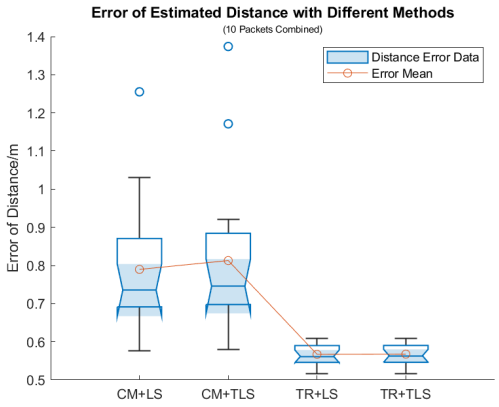

(c) Distance Errors in Experiment 2

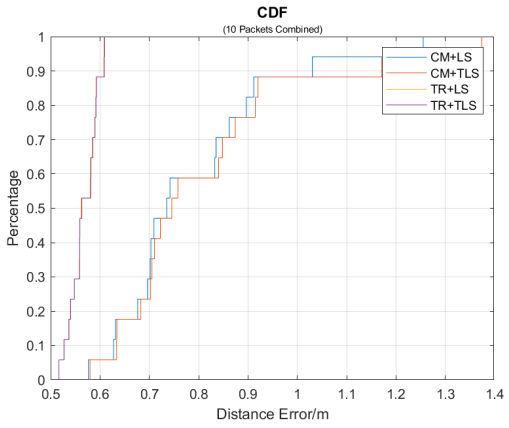

(d) CDF of Distance Errors in Experiment 2

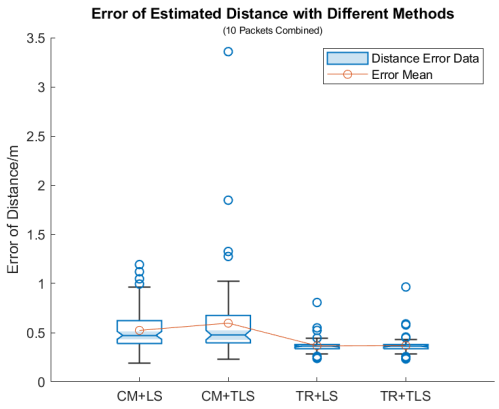

(e) Distance Errors in Experiment 3

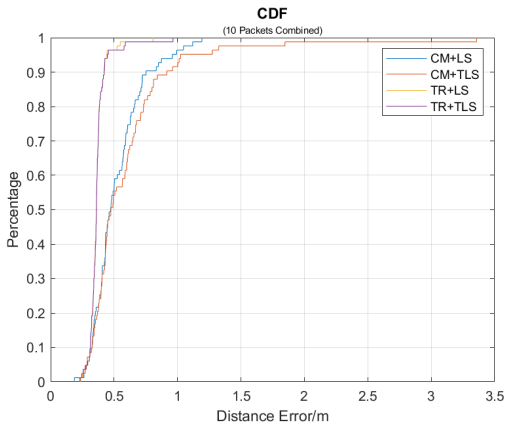

(f) CDF of Distance Errors in Experiment 3

Figure 7.9: Positioning Errors in Three Experiments with 10 Packets Combined.

7.5. Conclusion

In this section, the process and results of the experiment were introduced and explained. The distinguishing aspects of this project in comparison to prior research are:

- Combining BLE direction-finding feature with URA for 2-D AoA estimation instead of 1-D;
- Estimate the 3-D position with estimated angles, while previous researches either not involved

positioning or only estimate the 2-D positions;

- Consider the multipath mitigation in 2-D AoA estimation with a limited number of antennas.

The obtained results, while needing more improvement for practical implementation, show improvements compared to prior studies on BLE AoA and position estimation, particularly in regard to elevation angle estimation. Furthermore, the combination of data from various packets has been shown to increase the precision of angle estimation. Increasing the amount of data collected would enhance the precision of angle estimations, resulting in an enhanced final estimation of the location.

8

Conclusion

8.1. Conclusions

This thesis focuses on the Bluetooth direction-finding feature CTE, which was introduced in version 5.1. CTE allows for the estimation of both AoA and AoD. The objective of this project is to develop an algorithm that leverages the CTE feature with a multi-antenna array to accurately determine the precise location of the beacon.

To begin, a 2-D antenna array data model was created with a far-field assumption. The model incorporates the main challenges, namely frequency offset and multipath situation. The CFO is then introduced by exploring how it affects angle estimation. It is also integrated with the URA's non-simultaneous sampling scheme, which involves switching between multiple antennas. AoA estimation methods, mostly sub-space ones like MUSIC and ESPRIT, were also introduced. The investigation was carried out to look into the causes of the failure of sub-space techniques in the presence of multipath. The multipath mitigation approaches of SS, FBSS, and TR were then presented. Their capability of recovering the rank of the covariance matrix was investigated, as was their limitation of resolving more multipath in a 2-D scenario with a limited number of antennas. Following that, an attempt is made to introduce VA techniques. It fails, however, when dealing with multipath. We compared the LS and TLS positioning algorithms to the supplied Matlab algorithm after estimating the angles.

The performance of the algorithm was assessed using Matlab simulations. Matlab's built-in functions were employed to generate BLE signals, while its ray-tracing method was utilized to simulate near-ideal multipath propagation. The simulation consists of three distinct phases: the first phase involves estimating the angle using a fixed transmitter and a single locator; the second phase involves estimating the angle using a transmitter in various positions and a single locator; and the third phase involves estimating the position using a fixed transmitter and multiple fixed locators. In the first scenario, various factors were examined that could potentially impact the estimation of angles. These factors encompassed the SNR, the estimated number of sources, the combined number of packets, and the parameters utilized in mitigation algorithms, among others. The findings from the simulation demonstrate that the TR method, when appropriately configured, yields the most accurate estimation outcomes. The Monte-Carlo simulation results indicate that the placement error with four locators can reach a minimum value of 0.14 m with a confidence level of 90%.

Afterwards, an outdoor study was conducted to assess the efficacy of the algorithm in an actual outdoor environment. In order to mitigate the effects of unmanageable multipath interference, the experiment was carried out outdoors. Valid data was only taken into account if it was obtained through stable connections. The experiment involved the examination of three distinct transmitter locations using three fixed locators. The current experimental framework exhibits a higher level of complexity compared to previous studies, as it incorporates both environmental transmission channels and I/Q data obtained from real-world scenarios. The RMSE for the azimuth angle is found to be less than $5\circ$ when utilizing a 4×4 URA. Moreover, employing the TR+LS algorithm and incorporating data from 10 packets yields a positioning error that is below 0.45 m in 95% of the cases. This performance is notably superior to previous research conducted in one dimension, where 95% of the results exhibited a positioning error exceeding 0.85 m.

8.2. Future Work

For future works, studies could be done for these following aspects:

- Investigate automatically adjust optimal parameters for the TR methods as its performance is greatly influenced by the choice of P and Q.
- Incorporate additional elements that may impact the accuracy of angle estimation within the data model, such as mutual coupling, switch leakage, and path imbalance.
- Investigate the feasibility of different CTE configurations. In some previous research, the TI hardware could achieve a higher sampling rate for the reference period. The acquisition of more data within the limited CTE packet length could potentially benefit both the angle and the position estimation.
- Propose an experiment configuration that offers enhanced control over multipath conditions, facilitating a more comprehensive analysis of its effects.
- Integrate the previously employed RSSI data in BLE technology with the novel CTE features. Since RSSI can provide distance information rather than angles, it can aid in positioning.
- Further process the experiment data. In this project, all valid data with a solid connection was utilized. However, for more accurate estimation, only those packets acquired at the time of the instant or event counter when connections to all locators are stable should be considered.
- Conduct an examination of the spatial arrangement in relation to a mobile transmitter. In this project, it was assumed that the transmitter remains stationary in order to facilitate the application of packet aggregation technique, which allows for the combination of a larger amount of data to improve estimation accuracy. Nevertheless, in the event that the transmitter is in motion, it is only possible to utilize the data that is sampled within a brief time frame for the purpose of estimating a singular position. This would significantly increase the level of difficulty associated with the estimation process.

References

[1] Axel Küpper. *Location-based services: fundamentals and operation*. John Wiley & Sons, 2005.

[2] Faheem Zafari, Athanasios Gkelias, and Kin K Leung. “A survey of indoor localization systems and technologies”. In: *IEEE Communications Surveys & Tutorials* 21.3 (2019), pp. 2568–2599.

[3] Mikkel Baun Kjærgaard. “A taxonomy for radio location fingerprinting”. In: *Location-and Context-Awareness: Third International Symposium, LoCA 2007, Oberpfaffenhofen, Germany, September 20-21, 2007. Proceedings 3*. Springer. 2007, pp. 139–156.

[4] Song Chai, Renbo An, and Zhengzhong Du. “An indoor positioning algorithm using bluetooth low energy RSSI”. In: *2016 International Conference on Advanced Materials Science and Environmental Engineering*. Atlantis Press. 2016, pp. 274–276.

[5] SD Padiya and VS Gulhane. “Analysis of Bluetooth Versions (4.0, 4.2, 5, 5.1, and 5.2) for IoT Applications”. In: *Implementing Data Analytics and Architectures for Next Generation Wireless Communications*. IGI Global, 2022, pp. 153–178.

[6] Hongyun Ye et al. “A method of indoor positioning by signal fitting and PDDA algorithm using BLE AOA device”. In: *IEEE Sensors Journal* 22.8 (2022), pp. 7877–7887.

[7] Lichen Yao. “Bluetooth direction finding”. In: (2018).

[8] SD Cloudt. “Bluetooth low energy direction finding on embedded hardware by mitigating carrier frequency offset and multipath fading”. PhD thesis. Master thesis, Eindhoven University of Technology, 2021.

[9] Wenzhao Shu and Shuai Wang. “A Indoor Positioning System of Bluetooth AOA Using Uniform Linear Array Based on Two-point Position Principle”. In: *IEEE SENSORS JOURNAL* 30.8 (2022), p. 1.

[10] Shuai He, Hang Long, and Wei Zhang. “Multi-antenna array-based aoa estimation using bluetooth low energy for indoor positioning”. In: *2021 7th International Conference on Computer and Communications (ICCC)*. IEEE. 2021, pp. 2160–2164.

[11] Praveen Kumar, Lohith Reddy, and Shirshu Varma. “Distance measurement and error estimation scheme for RSSI based localization in wireless sensor networks”. In: *2009 Fifth international conference on wireless communication and sensor networks (WCSN)*. IEEE. 2009, pp. 1–4.

[12] Zheng Yang, Zimu Zhou, and Yunhao Liu. “From RSSI to CSI: Indoor localization via channel response”. In: *ACM Computing Surveys (CSUR)* 46.2 (2013), pp. 1–32.

[13] Marco Altini et al. “Bluetooth indoor localization with multiple neural networks”. In: *IEEE 5th International Symposium on Wireless Pervasive Computing 2010*. IEEE. 2010, pp. 295–300.

[14] Hakan Koyuncu and Shuang Hua Yang. “A survey of indoor positioning and object locating systems”. In: *IJCSNS International Journal of Computer Science and Network Security* 10.5 (2010), pp. 121–128.

[15] Waltenegus Dargie and Christian Poellabauer. *Fundamentals of wireless sensor networks: theory and practice*. John Wiley & Sons, 2010.

[16] Hui Liu et al. “Survey of wireless indoor positioning techniques and systems”. In: *IEEE Transactions on Systems, Man, and Cybernetics, Part C (Applications and Reviews)* 37.6 (2007), pp. 1067–1080.

[17] Jie Xiong and Kyle Jamieson. “{ArrayTrack}: A {Fine-Grained} indoor location system”. In: *10th USENIX Symposium on Networked Systems Design and Implementation (NSDI 13)*. 2013, pp. 71–84.

[18] Swarun Kumar et al. “Accurate indoor localization with zero start-up cost”. In: *Proceedings of the 20th annual international conference on Mobile computing and networking*. 2014, pp. 483–494.

[19] Jacopo Tosi et al. “Performance evaluation of bluetooth low energy: A systematic review”. In: *Sensors* 17.12 (2017), p. 2898.

[20] Jie Xiong. “Pushing the limits of indoor localization in today’s Wi-Fi networks”. PhD thesis. UCL (University College London), 2015.

[21] Jiang Xiao et al. “A survey on wireless indoor localization from the device perspective”. In: *ACM Computing Surveys (CSUR)* 49.2 (2016), pp. 1–31.

[22] Manikanta Kotaru et al. “Spotfi: Decimeter level localization using wifi”. In: *Proceedings of the 2015 ACM Conference on Special Interest Group on Data Communication*. 2015, pp. 269–282.

[23] Han Zou et al. “An online sequential extreme learning machine approach to WiFi based indoor positioning”. In: *2014 IEEE World Forum on Internet of Things (WF-IoT)*. IEEE. 2014, pp. 111–116.

[24] Bashima Islam et al. “Rethinking ranging of unmodified BLE peripherals in smart city infrastructure”. In: *Proceedings of the 9th ACM Multimedia Systems Conference*. 2018, pp. 339–350.

[25] Javier JM Diaz et al. “Bluepass: An indoor bluetooth-based localization system for mobile applications”. In: *The IEEE symposium on Computers and Communications*. IEEE. 2010, pp. 778–783.

[26] Roshan Ayyalasomayajula, Deepak Vasisht, and Dinesh Bharadia. “BLoc: CSI-based accurate localization for BLE tags”. In: *Proceedings of the 14th International Conference on emerging Networking EXperiments and Technologies*. 2018, pp. 126–138.

[27] SIG Bluetooth. *Bluetooth Core Specification 5.2. 2019*.

[28] Engin Tuncer and Benjamin Friedlander. *Classical and modern direction-of-arrival estimation*. Academic Press, 2009.

[29] Craig Robinson and Alan Purvis. “Demodulation of bluetooth GFSK signals under carrier frequency error conditions”. In: *IEE Colloquium on DSP enabled Radio*. IET. 2003, pp. 1–11.

[30] Rudi De Buda. “Coherent demodulation of frequency-shift keying with low deviation ratio”. In: *IEEE transactions on communications* 20.3 (1972), pp. 429–435.

[31] Paul H Moose. “A technique for orthogonal frequency division multiplexing frequency offset correction”. In: *IEEE Transactions on communications* 42.10 (1994), pp. 2908–2914.

[32] Sara A Van De Geer. “Least-Squares Estimation”. In: *Encyclopedia of Statistics in Quality and Reliability* 2 (2008).

[33] Steven M Kay. *Fundamentals of statistical signal processing: estimation theory*. Prentice-Hall, Inc., 1993.

[34] M Haardt et al. “ESPRIT and closed-form 2-D angle estimation with planar arrays”. In: *Digital Signal Processing Handbook* (1998).

[35] Martin Haardt et al. “2D unitary ESPRIT for efficient 2D parameter estimation”. In: *1995 International Conference on Acoustics, Speech, and Signal Processing*. Vol. 3. IEEE. 1995, pp. 2096–2099.

[36] Tie-Jun Shan, Mati Wax, and Thomas Kailath. “On spatial smoothing for direction-of-arrival estimation of coherent signals”. In: *IEEE Transactions on Acoustics, Speech, and Signal Processing* 33.4 (1985), pp. 806–811.

[37] Tie-Jun Shan and Thomas Kailath. “Adaptive beamforming for coherent signals and interference”. In: *IEEE Transactions on Acoustics, Speech, and Signal Processing* 33.3 (1985), pp. 527–536.

[38] S Unnikrishna Pillai and Byung Ho Kwon. “Forward/backward spatial smoothing techniques for coherent signal identification”. In: *IEEE Transactions on Acoustics, Speech, and Signal Processing* 37.1 (1989), pp. 8–15.

[39] Huiyue Yi and Xilang Zhou. “On 2D forward-backward spatial smoothing for azimuth and elevation estimation of coherent signals”. In: *2005 IEEE Antennas and Propagation Society International Symposium*. Vol. 2. IEEE. 2005, pp. 80–83.

[40] Benjamin Friedlander and Anthony J Weiss. “Direction finding using spatial smoothing with interpolated arrays”. In: *IEEE Transactions on Aerospace and Electronic Systems* 28.2 (1992), pp. 574–587.

[41] Yih-Min Chen. “On spatial smoothing for two-dimensional direction-of-arrival estimation of coherent signals”. In: *IEEE Transactions on Signal Processing* 45.7 (1997), pp. 1689–1696.

[42] Wikipedia. *Toeplitz matrix*. URL: https://en.wikipedia.org/wiki/Toeplitz_matrix#:~:text=In%20linear%20algebra%2C%20a%20Toeplitz,matrix%20is%20a%20Toeplitz%20matrix%3A&text=A%20Toeplitz%20matrix%20is%20not%20necessarily%20square. (visited on 07/19/2023).

[43] Fang-Ming Han and Xian-Da Zhang. “An ESPRIT-like algorithm for coherent DOA estimation”. In: *IEEE Antennas and Wireless Propagation Letters* 4 (2005), pp. 443–446.

[44] Fang-Jiong Chen, Sam Kwong, and Chi-Wah Kok. “ESPRIT-like two-dimensional DOA estimation for coherent signals”. In: *IEEE Transactions on Aerospace and Electronic Systems* 46.3 (2010), pp. 1477–1484.

[45] Yingbo Hua. “Estimating two-dimensional frequencies by matrix enhancement and matrix pencil”. In: (1992).

[46] Fang-Jiong Chen et al. “Estimation of two-dimensional frequencies using modified matrix pencil method”. In: *IEEE transactions on signal processing* 55.2 (2007), pp. 718–724.

[47] Yankui Zhang et al. “High-accuracy DOA estimation based on vectorized fourth-order cumulant with coprime array”. In: *2019 IEEE 19th International Conference on Communication Technology (ICCT)*. IEEE. 2019, pp. 210–215.

[48] Hirotugu Akaike. “A new look at the statistical model identification”. In: *IEEE transactions on automatic control* 19.6 (1974), pp. 716–723.

[49] Jorma Rissanen. “A universal prior for integers and estimation by minimum description length”. In: *The Annals of statistics* 11.2 (1983), pp. 416–431.

[50] Zhaoshui He et al. “Detecting the number of clusters in n-way probabilistic clustering”. In: *IEEE Transactions on Pattern Analysis and Machine Intelligence* 32.11 (2010), pp. 2006–2021.

[51] Gene H Golub and Charles F Van Loan. “An analysis of the total least squares problem”. In: *SIAM journal on numerical analysis* 17.6 (1980), pp. 883–893.

[52] Duke University. *Total Least Squares*. https://people.duke.edu/~hpgavin/SystemID/CourseNotes/TotalLeastSquares.pdf. Accessed: 2023-06-19.

[53] *Bluetooth LE Positioning by Using Direction Finding*. URL: https://nl.mathworks.com/help/bluetooth/ug/bluetooth-le-based-positioning-using-direction-finding.html.

[54] Marco Cominelli, Paul Patras, and Francesco Gringoli. “Dead on arrival: An empirical study of the Bluetooth 5.1 positioning system”. In: *Proceedings of the 13th international workshop on wireless network testbeds, experimental evaluation & characterization*. 2019, pp. 13–20.

[55] Nordic Semiconductor. *nRF52833 DK*. URL: https://www.nordicsemi.com/Products/Development-hardware/nrf52833-dk.

[56] Nordic Semiconductor. *nRF52833 Chip*. URL: https://www.nordicsemi.com/Products/nRF52833.

A

Appendix A: Cramer-Rao Lower Bound of Frequency Offset Estimation

A.1. Basic Model

In this section, we will examine the Cramér-Rao Lower Bound (CRLB) associated to the estimation of frequency offset. The data model being discussed in this context is

$$\mathbf{X}(t) = \mathbf{OA}s(t) + \mathbf{W}(t) \tag{A.1}$$

where

$$\begin{aligned}\mathbf{O} &= \text{diag}\begin{bmatrix} o_1 & o_2 & \cdots & o_{MN} \end{bmatrix} \\ &= \begin{bmatrix} 1 & & & \\ & e^{-2\pi(f_c+f_o)\triangle T} & & \\ & & \ddots & \\ & & & e^{-2\pi(f_c+f_o)(MN-1)\triangle T} \end{bmatrix} \\ &= \begin{bmatrix} 1 & & & \\ & e^{-2\pi f_o\triangle T} & & \\ & & \ddots & \\ & & & e^{-2\pi f_o(MN-1)\triangle T} \end{bmatrix} \in \mathbb{C}^{MN\times MN}\end{aligned}$$

is the frequency offset matrix, where the channel frequency f_c is ignored due to its large value, resulting in an integer of pi, which makes no difference if ignored, and $\triangle T$ is the time interval between two consecutive samples. And

$$\begin{aligned}\mathbf{A} &= \mathbf{a}(\theta_1, \phi_1) \\ &= \begin{bmatrix} e^{\tau_1} \\ e^{\tau_2} \\ \vdots \\ e^{\tau_{MN}} \end{bmatrix} \in \mathbb{C}^{MN\times 1}\end{aligned}$$

is the steering vector of the LOS signal at time t ,i.e.$s(t)$, τ_i indicates the antenna response at the (i-1)-th antenna, and $\mathbf{W}(t) = \begin{bmatrix} w_1 & w_2 & \cdots & w_{MN} \end{bmatrix}^T \in \mathbb{C}^{MN\times 1}$ is the white Gaussian noise vector, which has a zero-mean and the variance σ^2, i.e., for all the noise received at the i-th antenna, $w_i \sim \mathcal{N}(0, \sigma^2)$. No multipath scenario is considered here, and we assume $\tau_i \neq \tau_j$ when $i \neq j$.

Construct the unknown parameter $\xi = \begin{bmatrix} f_o & \tau_1 & \tau_2 & \cdots & \tau_{MN} \end{bmatrix}^T$ contaning MN the unknown in model shown in (A.1).

A.2. Distribution of Data Matrix $\mathbf{X}(t)$

For every element $x_i(t)$ in the data vector $\mathbf{X}(t)$, according to the previous model. Each $x_i(t)$ follows a complex normal distribution that is

$$x_i \sim \mathcal{N}(o_i a_i s(t), \sigma^2) \tag{A.2}$$

and its real part and imaginary part respectively follow:

$$\begin{aligned} \Re\{x_i\} &\sim \mathcal{N}(\Re\{o_i a_i s(t)\}, \tfrac{\sigma^2}{2}) \\ \Im\{x_i\} &\sim \mathcal{N}(\Im\{o_i a_i s(t)\}, \tfrac{\sigma^2}{2}) \end{aligned} \tag{A.3}$$

Thus, the probability density function (PDF) for (A.3) is

$$\begin{aligned} f(\Re\{x_i\}|\xi) &= \tfrac{2}{\sigma\sqrt{2\pi}} e^{-\frac{(\Re\{x_i\}-\Re\{o_i a_i s(t)\})^2}{\sigma^2}} \\ f(\Im\{x_i\}|\xi) &= \tfrac{2}{\sigma\sqrt{2\pi}} e^{-\frac{(\Im\{x_i\}-\Im\{o_i a_i s(t)\})^2}{\sigma^2}} \end{aligned} \tag{A.4}$$

Due to the independence and identical distribution of the real and imaginary components, the PDF for the entire vector $\mathbf{X}(t)$ with respect to the unknown vector ξ is obtained by multiplying all the PDFs in (A.4) together. To simplify the notation, the mean value of each x_i is denoted by $y_i = o_i a_i s(t) = e^{j2\pi f_o}$, and the total number of antennas is denoted by $M_T = MN$. Then

$$f(\mathbf{X}(t)|\boldsymbol{\xi}) = \prod_{i=1}^{M_T} \frac{2}{\sigma\sqrt{2\pi}} e^{-\frac{(\Re\{x_i\}-\Re\{y_i\})^2}{\sigma^2}} \overset{\#}{\prod_{i=1}} \frac{2}{\sigma\sqrt{2\pi}} e^{-\frac{(\Im\{x_i\}-\Im\{y_i\})^2}{\sigma^2}} \tag{A.5}$$

$$= (\frac{2}{\sigma\sqrt{2\pi}})^{2M_T} \prod_{i=1}^{M_T} e^{-\frac{(\Re\{x_i\}-\Re\{y_i\})^2+(\Im\{x_i\}-\Im\{y_i\})^2}{\sigma^2}} \tag{A.6}$$

A.3. Likelihood Function

The likelihood function is defined as the log-likelihood of the (A.6):

$$\begin{aligned} \ell(\boldsymbol{\xi}; \mathbf{X}(t)) &= \ln f(\mathbf{X}(t)|\boldsymbol{\xi}) \\ &= \ln(\frac{2}{\sigma\sqrt{2\pi}})^{2M_T} - \frac{1}{\sigma^2}\sum_{i=1}^{M_T}(\Re\{x_i\} - \Re\{y_i\})^2 + (\Im\{x_i\} - \Im\{y_i\})^2 \end{aligned} \tag{A.7}$$

It is important to highlight that the expression $(\frac{2}{\sigma\sqrt{2\pi}})^{2M_T}$ remains constant regardless of any unknown variable ξ when computing the derivatives. Furthermore, it should be noted that the real part and imaginary part of x_i solely serve as measurements and remain constant with respect to the unknown.

A.4. First Derivatives

With (A.7), we can compute the first derivatives for all parameters in ξ.

Let us express the real and imaginary components of y_i explicitly as functions of τ and f_o:

$$\begin{aligned} \Re\{y_i\} &= \cos(\angle y_i) = \cos(\angle e^{j2\pi f_o (i-1)\triangle T} e^{-j\tau_i} s(t)) \\ \Im\{y_i\} &= \sin(\angle y_i) = \sin(\angle e^{j2\pi f_o (i-1)\triangle T} e^{-j\tau_i} s(t)) \end{aligned} \tag{A.8}$$

Accordingly, their first derivatives are

$$\begin{aligned} \tfrac{\partial}{\partial f_o}\Re\{y_i\} &= -\sin(\angle y_i)\,|y_i|\,(j2\pi(i-1)\triangle T) \\ \tfrac{\partial}{\partial f_o}\Im\{y_i\} &= \cos(\angle y_i)\,|y_i|\,(j2\pi(i-1)\triangle T) \end{aligned} \tag{A.9}$$

In the subsequent section, the magnitude of y_i, denoted as $|y_i|$, is considered to be equal to 1, as previously established in the model.

For f_o, the first derivatives is

$$\begin{aligned} \frac{\partial}{\partial f_o}\ell(\xi; \mathbf{X}(t)) &= \frac{2}{\sigma^2}\sum_{i=1}^{M_T}(\Re\{x_i\}\frac{\partial \Re\{y_i\}}{\partial f_o} + \Im\{x_i\}\frac{\partial \Im\{y_i\}}{\partial f_o}) \\ &= \frac{j4\pi\triangle T}{\sigma^2}\sum_{i=1}^{M_T}(i-1)(-\Re\{x_i\}\sin(\angle y_i) + \Im\{x_i\}\cos(\angle y_i)) \end{aligned} \tag{A.10}$$

Then, the derivatives with respect to each τ_i are

$$\begin{aligned}\frac{\partial}{\partial\tau_i}\ell(\xi;\mathbf{X}(t)) &= \frac{2}{\sigma^2}\sum_{l=1}^{M_T}(\Re\{x_l\}\frac{\partial\Re\{y_l\}}{\partial\tau_i}+\Im\{x_l\}\frac{\partial\Im\{y_l\}}{\partial\tau_i})\\ &= \frac{-2j}{\sigma^2}(-\Re\{x_i\}\sin(\angle y_i)+\Im\{x_i\}\cos(\angle y_i))\end{aligned} \tag{A.11}$$

since those y_l with $l\neq i$ are all considered to be constant with respect to τ_i.

A.5. Fisher Information Matrix

For the unknown vector $\xi=\begin{bmatrix}\xi_1 & \xi_2 & \cdots & \xi_n\end{bmatrix}^T$, the (i,j) the element in the Firsher Information Matrix (FIM) is

$$\begin{aligned}\mathcal{I}(\xi)_{(i,j)} &= -\mathsf{E}\left[\frac{\partial^2}{\partial\xi_i\partial\xi_j}|\xi\right]\\ &= -\mathsf{E}\left[\frac{\partial}{\partial\xi_i}\ell(\xi;X(t))\frac{\partial}{\partial\xi_j}\ell(\xi;X(t))|\xi\right]\end{aligned} \tag{A.12}$$

where E indicates taking the expectation when certain regularity conditions hold. From (A.12), it is obvious that FIM is symmetric.

What's worth noting is that only x_i is considered a random variable, i.e., $\mathsf{E}[\Re\{x_i\}]=\Re\{y_i\}$, $\mathsf{E}[\Im\{x_i\}]=\Im\{y_i\}$, y_i is considered a constant and stays unchanged after taking the expectations.

A.5.1. FIM Elements only Related to f_o

First, compute the second derivatives with respect to f_o:

$$\begin{aligned}\frac{\partial^2}{\partial f_o^2}\ell(\xi|\mathbf{X}(t)) &= \frac{j4\pi\triangle T}{\sigma^2}\sum_{i=1}^{M_T}(i-1)|y_i|(j2\pi(i-1)\triangle T)\left(-\Re\{x_i\}\cos(\angle y_i)-\Im\{x_i\}\sin(\angle y_i)\right)\\ &= -\frac{8\pi^2\triangle T^2}{\sigma^2}\sum_{i=1}^{M_T}(i-1)^2\left(\Re\{x_i\}\cos(\angle y_i)+\Im\{x_i\}\sin(\angle y_i)\right)\end{aligned} \tag{A.13}$$

Then taking the expectation over the second dericative,

$$\begin{aligned}\mathcal{I}(\xi)_{(f_o,f_o)} &= -\mathsf{E}\left[\frac{\partial^2}{\partial f_o^2}\ell(\xi|\mathbf{X}(t))\right]\\ &= \frac{8\pi^2\triangle T^2}{\sigma^2}\sum_{i=1}^{M_T}(i-1)^2\end{aligned} \tag{A.14}$$

A.5.2. FIM Elements only Related to τ_i

The second derivatives of τ_i itself are:

$$\begin{aligned}\frac{\partial^2}{\partial\tau_i^2}\ell(\xi|\mathbf{X}(t)) &= \frac{-2j}{\sigma^2}|y_i|(-j)(-\Re\{x_i\}\cos(\angle y_i)-\Im\{x_i\}\sin(\angle y_i))\\ &= \frac{2}{\sigma^2}(\Re\{x_i\}\cos(\angle y_i)+\Im\{x_i\}\sin(\angle y_i))\end{aligned} \tag{A.15}$$

For $i\neq j$, the second derivatives of $\frac{\partial^2}{\partial\tau_i\partial\tau_j}\ell(\xi|\mathbf{X}(t))=0$ since the first derivatives of τ_i do not contain the variable τ_j and thus are considered constants with respect to τ_j.

Then the corresponding FIM elements are:

$$\begin{aligned}\mathcal{I}(\xi)_{(\phi_i,\phi_j)} &= \tfrac{\partial^2}{\partial\tau_i^2}\ell(\xi|\mathbf{X}(t))=-\tfrac{2}{\sigma^2} \quad i=j,1<i,j\leq M\\ \mathcal{I}(\xi)_{\phi_i,\phi_j)} &= \tfrac{\partial^2}{\partial\tau_i\partial\tau_j}\ell(\xi|\mathbf{X}(t))=0 \quad i\neq j,1<i,j\leq M\end{aligned} \tag{A.16}$$

A.5.3. FIM Elements Related to f_o and τ_i

Since FIM is symmetric, we only need to calculate the second derivatives of $\frac{\partial^2}{\partial f_o \partial \tau_i}\ell(\xi|\mathbf{X}(t)) = \frac{\partial^2}{\partial \tau_i \partial f_o}\ell(\xi|\mathbf{X}(t))$:

$$\begin{aligned}\mathsf{E}\left[\frac{\partial^2}{\partial f_o \partial \tau_i}\ell(\xi|\mathbf{X}(t))\right] &= \frac{-2j}{\sigma^2}(-\Re\{x_i\}\cos(\angle y_i)(j2\pi(i-1)\triangle T) - \Im\{x_i\}\sin(\angle y_i)(j2\pi(i-1)\triangle T)) \\ &= \frac{-4\pi(i-1)\triangle T}{\sigma^2}\end{aligned} \tag{A.17}$$

Then the corresponding elements in the first row/column of FIM are:

$$\begin{aligned}\mathcal{I}(\xi)_{f_o,\phi_i} &= \mathcal{I}(\xi)_{\phi_i,f_o} \\ &= \frac{4\pi(i-1)\triangle T}{\sigma^2}\end{aligned} \tag{A.18}$$

Then the complete FIM is

$$\begin{aligned}\mathbf{I}(\xi) &= \mathbf{I}(f_o,\phi_1,\cdots,\phi_M) \\ &= \begin{bmatrix} \mathcal{I}(\xi)_{f_o,f_o} & \mathcal{I}(\xi)_{\phi_1,f_o} & \cdots & \mathcal{I}(\xi)_{\phi_{M_T},f_o} \\ \mathcal{I}(\xi)_{f_o,\phi_1} & \mathcal{I}(\xi)_{\phi_1,\phi_1} & & \vdots \\ \vdots & & \ddots & \vdots \\ \mathcal{I}(\xi)_{f_o,\phi_{M_T}} & \cdots & \cdots & \mathcal{I}(\xi)_{\phi_{M_T},\phi_{M_T}} \end{bmatrix}\end{aligned} \tag{A.19}$$

And the CRLB matrix $V(\xi)$ is defined as the inverse of FIM, i.e., $V(\xi)I(\xi) = I$.

Denote the $V(\xi)$ matrix as:

$$\begin{aligned}\mathbf{V}(\xi) &= \mathbf{V}(f_o,\phi_1,\cdots,\phi_M) \\ &= \begin{bmatrix} \mathcal{V}(\xi)_{f_o,f_o} & \mathcal{V}(\xi)_{\phi_1,f_o} & \cdots & \mathcal{V}(\xi)_{\phi_{M_T},f_o} \\ \mathcal{V}(\xi)_{f_o,\phi_1} & \mathcal{V}(\xi)_{\phi_1,\phi_1} & & \vdots \\ \vdots & & \ddots & \vdots \\ \mathcal{V}(\xi)_{f_o,\phi_{M_T}} & \cdots & \cdots & \mathcal{V}(\xi)_{\phi_{M_T},\phi_{M_T}} \end{bmatrix}\end{aligned} \tag{A.20}$$

where only the $\mathcal{V}(\xi)_{f_o,f_o}$ element is the CRLB for the frequency offset we care about. Then, with known elements in FIM, the following equations are listed:

$$\begin{cases} \mathbf{V}(\boldsymbol{\xi})_{f_o,f_o}\mathbf{I}(\boldsymbol{\xi})_{f_o,f_o} + \sum_{i=1}^{M_T}\mathbf{V}(\boldsymbol{\xi})_{\phi_i,f_o}\mathbf{I}(\boldsymbol{\xi})_{f_o,\phi_i} & = 1 \\ \mathbf{V}(\boldsymbol{\xi})_{f_o,f_o}\mathbf{I}(\boldsymbol{\xi})_{\phi_i,f_o} + \mathbf{V}(\boldsymbol{\xi})_{f_o,\phi_i}\mathbf{I}(\boldsymbol{\xi})_{\phi_i,\phi_i} & = 0 \quad for \quad i \in [1,M_T] \end{cases} \tag{A.21}$$

After calculating each $\mathbf{V}(\xi)_{f_o,\phi_i}$ with FIM elements and $\mathbf{V}(\xi)_{f_o,\phi_i}$. Since V matrix is also diagonal symmetric, $\mathbf{V}(\boldsymbol{\xi})_{f_o,\phi_i} = \mathbf{V}(\boldsymbol{\xi})_{\phi_i,f_o}$. Finally, the CRLB of f_o is

$$\mathsf{CRLB} = \mathbf{V}(\boldsymbol{\xi})_{f_o,f_o} \tag{A.22}$$

$$= \frac{1}{\left(\mathbf{I}(\boldsymbol{\xi})_{f_o,f_o} - \sum_{i=1}^{M_T}\frac{\mathbf{I}(\boldsymbol{\xi})^2_{f_o,\phi_i}}{\mathbf{I}(\boldsymbol{\xi})_{\phi_i,\phi_i}}\right)} \tag{A.23}$$

A.6. Estimate Frequency Offset with Reference Samples Only

As explained in Chapter3, the estimation of CFO is only going to be conducted using samples derived from the reference period. Therefore, the data model has been modified to:

$$\begin{aligned}\mathbf{X}(t) &= \mathbf{o}a_1 s(t) \\ &= \begin{bmatrix} e^{2\pi f_o \triangle T} \\ e^{2\pi f_o 2\triangle T} \\ \vdots \\ e^{2\pi f_o N_T \triangle T} \end{bmatrix} e^{-j\phi_1} s(t)\end{aligned} \tag{A.24}$$

Here **o** is the CFO vector since the reference period only sample on the same antenna. And N_T is the number of samples within the reference period. This model can be interpreted as the process of sampling at a total of N_T antennas, all with the same steering response, but at different time instants. Only two unknown parameters appear, so $\boldsymbol{\xi} = [f_o, \phi_1]$.

Then, following the same steps in the previous sections, we have

$$\begin{aligned} \mathbf{I}(\xi)_{f_o,f_o} &= \tfrac{8\pi^2 \triangle T^2}{\sigma^2} \textstyle\sum_{i=1}^{N_T} i^2 \\ \mathbf{I}(\xi)_{f_o,\phi_1} = \mathbf{I}(\xi)_{\phi_1,f_o} &= \tfrac{4\pi \triangle T \sum_{i=1}^{N_T} i}{\sigma^2} \\ \mathbf{I}(\xi)_{\phi_1,\phi_1} &= -\tfrac{2}{\sigma^2} \end{aligned} \tag{A.25}$$

And the FIM is a 2×2 matrix:

$$\begin{aligned} \mathbf{I}(\xi) &= \begin{bmatrix} \mathbf{I}(\xi)_{f_o,f_o} & \mathbf{I}(\xi)_{\phi_1,f_o} \\ \mathbf{I}(\xi)_{f_o,\phi_1} & \mathbf{I}(\xi)_{\phi_1,\phi_1} \end{bmatrix} \\ &= \begin{bmatrix} \frac{8\pi^2 \triangle T^2}{\sigma^2} \sum_{i=1}^{N_T} i^2 & \frac{4\pi \triangle T \sum_{i=1}^{N_T} i}{\sigma^2} \\ \frac{4\pi \triangle T \sum_{i=1}^{N_T} i}{\sigma^2} & -\frac{2}{\sigma^2} \end{bmatrix} \end{aligned} \tag{A.26}$$

Consider the CRLB matrix $\mathbf{V}(\xi)$ is the inverse of the matrix in (A.26), and the CRLB of f_o is $\mathbf{V}(\xi)_{f_o,f_o}$:

$$\begin{aligned} \mathbf{V}(\xi)_{f_o,f_o} &= \frac{1}{I(\xi)_{f_o,f_o} + \frac{I(\xi)_{f_o,\phi_1} I(\xi)_{\phi_1,f_o}}{I(\xi)_{\phi_1,\phi_1}}} \\ &= \frac{3}{2\pi^2 \text{SNR} \triangle T^2 (N_T^3 - N_T)} \end{aligned} \tag{A.27}$$

In summary, the CRLB associated with the estimation of frequency offset using only reference samples exhibits a connection with the Signal-to-Noise Ratio (SNR) expressed in decibels, the sampling rate of the reference signal, and the number of samples contained within the reference period.